Highly Birefringent Photonic Crystal Fibers and sensors

Submitted by JU JIAN

A thesis submitted in partial fulfillment of the requirements for the Degree of Doctor of Philosophy

Department of Electrical Engineering
The Hong Kong Polytechnic University

March 2006

CERRIFICATE OF ORIGINALITY

I hereby declare that this thesis is my own work and that, to the best of my knowledge and belief, it reproduces no material previously published or written, nor material that has been accepted for the award of any other degree or diploma, except where due acknowledgement has been made in the text.

JU Jian

ACKNOWLEDGEMENTS

The completion of this thesis that is required to obtain an advanced degree is the product of hard work, perseverance, and the continuous support of my family and my supervisors. I would like to thank my chief supervisor, Professor Wei Jin, for his continuous encouragement and guidance of my work. Your scientific attitude and rigorous working style has been and remains an invaluable asset to me. I’m also very grateful to my co-supervisor, Professor M. Suleyman Demokan, for your welcomed comments and spending time on my papers and thesis.

A special thank goes to Professor Jinghui Su and Professor Libo Yuan at Harbin Engineering University. Without your selfless help and recommendation I could not start my PhD study in Hong Kong.

I am very fortunate to have the love and support of my family. My wife, Mu Tou, your confidence in my ability was a welcomed voice at the other end of the telephone. I would like to thank my parents for your continual encouraging and prayers.

I wish to take this opportunity to thank my colleagues at the Fiber Optics Laboratory for their technical help and enjoyable hours.

ABSTRACT

A novel class of material, known as photonic crystal, has opened up new ways to guide the flow of light. In the early 1990s, Photonic Crystal Fibers (PCFs), an optical fiber using photonic crystal cladding, were developed. The pioneering experimental works on these fibers showed that they have inherently unprecedented properties and overcome many limitations of conventional optical fiber, i.e. guiding light in a hollow core, being endlessly single mode, having anomalous dispersion in the visible region, and possessing high nonlinear coefficients, etc. Among the many unique properties of PCFs, this thesis is most concerned with the polarization and modal properties of highly birefringent (Hi-Bi) PCFs with asymmetric core and different hole-sizes along the two orthogonal axes.

The thesis starts with a short review of conventional optical fibers and then proceeds to a discussion on the guiding mechanisms of solid core and hollow core PCFs. The main properties of solid core PCFs, i.e. confinement loss, fundamental mode cutoff and dispersion, are reviewed. A special section is devoted to Hi-Bi PCFs and their corresponding properties.

The basic properties of an asymmetrical core PCF are theoretically investigated by using the full-vector finite element method (FEM). The calculated birefringence is in good agreement with the measured value. The influence of fiber structural parameters on modal birefringence, mode field diameter (MFD), and half divergence angle are investigated in detail. The group velocity dispersions for the two fundamental modes

are also calculated and found to be significantly different for the two orthogonal polarizations.

The full-vector FEM is also used to calculate the electrical fields and to evaluate the equivalent MFD of endlessly single mode PCFs. It was found that the MFD increases approximately linearly with pitch Λ and decreases with an increase in air-hole diameter to pitch ratio d/Λ. An empirical formula is proposed for estimating the MFD. The results calculated by using the formula deviates less than 1% from those obtained from FEM for $0.25 \leq d/\Lambda \leq 0.45$. With the help of the MFD, the connection loss between a single mode fiber and a PCF can be evaluated by using the classical method based on the MFD.

Through the analysis of a Hi-Bi PCF by FEM with anisotropic perfectly matched layers (PMLs), we proposed a general design methodology for an asymmetrical core PCF to achieve single polarization single mode (SPSM) operation at an arbitrary operating wavelength. Specifically we optimized the PCF structure for SPSM operation around 1.30μm and 1.55μm. The bandwidths of the SPSM PCFs are respectively 84.7nm and 103.5nm for 1.30μm and 1.55μm, within which one polarization state is attenuated by at least 30dB/m while the orthogonal state suffers a confinement loss of less than 1dB/m. The cutoff wavelengths of these fibres are further validated by calculating the effective mode area of each polarization, which deviates less than 4% from that found by the confinement loss calculation using FEM. The coupling losses between the proposed SPSM fibers and single mode fibers were also

calculated by using the overlap integral method and found to be ~78% and ~77% at 1.55μm and 1.30μm, respectively.

A similar Hi-Bi PCF but with different parameters is found to support only the LP_{01} and LP_{11}(even) modes from 543nm to 1310nm. The LP_{11}(odd) mode is unsupported within this broad range, and the supported LP_{11}(even) mode has a stable intensity lobe orientation. The very broad two-mode wavelength range will allow a number of novel two-mode devices to be developed. The examples of these devices include acousto-optic frequency shifters, tunable filters, modal filters, optical switches, etc. With the special modal properties of the Hi-Bi PCF, we experimentally demonstrated a two-mode PCF interferometer based on the modal interference between the LP_{01} and LP_{11}(even) modes propagating in the same length of PCF. The responses of the interferometer to axial strain and temperature were experimentally investigated over a wavelength range of from 600nm to 1310nm. For the strain sensor, the fiber elongations needed to produce 2π phase change decrease with the wavelength, indicating higher strain sensitivity at longer wavelengths. The strain sensitivity is also polarization dependent. The temperature sensitivity of the two-mode PCF sensor was measured and it showed a non-monotonic dependence on the operating wavelength. A mathematical model was developed to explain the non-monotonic temperature dependence, and found to agree in trends with the experimentally measured results. The unique wavelength dependence of the temperature/strain sensitivity would allow temperature insensitive strain measurement to be performed by operating the sensor at two selected wavelengths.

CONTENTS

CHAPTER 1

INTRODUCTION

1.1 Research motivation and contributions

A novel class of material, known as photonic crystal (PC), has opened up new ways to guide the flow of light. In such structures, propagation may be forbidden in any directions for a certain range of frequencies called photonic band gaps (PBGs). Based on the concepts of PBG, the microstructured photonic crystal cladding, running along the entire length of the fiber, can not allow light propagation in the cladding, hence light is trapped in the central hollow core. The hollow core photonic crystal fiber (PCF) using a triangular array of large air holes in the cladding was firstly demonstrated in 1999.

Another more common type of PCF is solid core PCF due to their relative ease of fabrication. For solid core PCF the guidance is attributed to modified total internal reflection (M-TIR), which is analogous to the TIR of conventional optical fibers. The effective index of the cladding is lower than that of the core, leading to a fiber structure similar to that of conventional step-index fiber. However, the refractive index of the microstructured cladding exhibits strong wavelength dependence, allowing PCF to possess unique properties unachievable by conventional fibers. The most striking among these properties is single mode operation over an infinite range of wavelength.

The pioneering experimental work on these PCFs showed that they have inherently unprecedented properties and overcome many limitations of conventional

optical fibers. With the versatile photonic crystal fiber, people can engineer the fiber properties from guiding light in vacuum to unthinkable dispersion properties, from enhanced nonlinearities by more confinement of light to minimizing the same non-linear effects by using very large mode area fibers. The discovery of these attractive properties makes PCFs ideal for high-power transmission without nonlinearities, all-optical signal processing, high power lasers and amplifiers, dispersion compensation, polarizing and polarization maintaining devices, and novel optical fiber sensors.

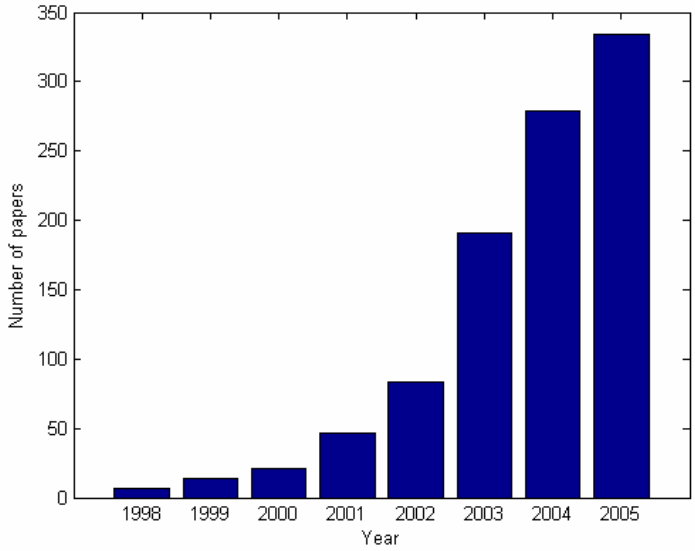

Figure 1.1 The number of papers retrieved from Science Citation Index Database.

PCFs have become one of the most popular research topics nowadays. Researchers with different background around the world start detailed investigating and drawing all kinds of PCFs. The number of papers retrieved from Science Citation Index Database by using “photonic crystal fiber”, “holey fiber”, and “microstructured fiber” as the key words shows an exponential increase from year 1996 to year 2005 (Fig. 1.1). Among the broad range of the unique properties of PCF, this thesis is mainly concerned with the polarization and modal properties of highly birefringent (Hi-Bi) PCFs with

asymmetric core and different hole-sizes along the two orthogonal axes. The main contributions made during the author's PhD studies are summarized as follows:

i. The basic properties of an asymmetrical core PCF are theoretically investigated by using the full-vector finite element method (FEM). The calculated birefringence is in good agreement with the measured value. The influence of fiber structural parameters on modal birefringence, mode field diameter (MFD), and half divergence angle are investigated in detail. The group velocity dispersions for the two fundamental modes are also calculated and found to be significantly different for the two orthogonal polarizations.

ii. The full-vector FEM is also used to calculate the electrical field and to evaluate the equivalent MFD of endlessly single mode (ESM) PCF. It was found that the MFD increases approximately linearly with pitch Λ and decreases with an increase in air-hole diameter to pitch ratio d/Λ. An empirical formula is proposed for estimating the MFD. With the help of the MFD, the connection loss between a single mode fiber and a PCF can be evaluated by using the classical method based on the MFD.

iii. Through the analysis of a Hi-Bi PCF by FEM with anisotropic perfectly matched layers (PMLs), we have presented the general design methodology of an asymmetrical core PCF for single polarization single mode (SPSM) operation at an arbitrary operating wavelength. Specifically we optimized the PCF structure for operating at 1.30μm and 1.55μm. The cutoff wavelength is further validated by calculating the effective area of each polarization. The coupling losses between the proposed SPSM fibers and single mode fibers

were also calculated by using the overlap integral method.

iv. A similar Hi-Bi PCF but with different structural parameters is found to support only the LP_{01} and LP_{11}(even) modes from 543nm to 1310nm. The LP_{11}(odd) mode is unsupported within this broad range, and the supported LP_{11}(even) mode has a stable intensity lobe orientation. With the special modal properties of the Hi-Bi PCF, we experimentally demonstrated a two-mode PCF interferometer based on the modal interference between the LP_{01} and LP_{11}(even) modes propagating in the same length of PCF. The responses of the interferometer to axial strain and temperature are experimentally investigated over a wavelength range of from 600nm to 1310nm. The strain sensor shows higher strain sensitivity at longer wavelengths, and the temperature sensitivity of the two-mode PCF sensor shows a non-monotonic dependence on the operating wavelength. We present a theoretical analysis of the non-monotonic response. The theoretical sensitivities agree in trends with the experimentally measured results.

The research contained herein has produced four publications in peer-reviewed journals and several conference papers (Appendix).

1.2 Thesis outline

This thesis is organized as follows:

Chapter 2 After a short review of the conventional optical fiber, we start introducing the guiding mechanism of PCF (section 2.1). The main properties of photonic crystal fibers and their corresponding applications are reviewed in section 2.2. This chapter finished with section 2.3, in this section special attention was paid to the

highly-birefringent PCF, with various fiber structures and their corresponding properties.

Chapter 3 This chapter starts with a general presentation of various numerical methods for analyzing PCFs and comparison of the advantage and disadvantage between them (section 3.1). Following the comparison we choose FEM as the main numerical method and a very general description of the FEM is described in section 3.2. As a commercial software, FEMLAB (Finite Element Modeling Laboratory) software package is employed throughout the thesis, we felt it's very important to validate its accuracy and the results are given in section 3.3. In the last section, we show an example to calculate the mode field of endlessly single mode fiber by using FEMLAB, which is further used to estimate the splice loss between photonic crystal fiber and single mode fiber SMF-28.

Chapter 4 This chapter presents a thorough analysis of the firstly reported Hi-Bi PCF. The mode properties and the single mode operation range are discussed in section 4.1. Section 4.2 and 4.3 investigate other properties of this Hi-Bi PCF, including modal birefringence, MFD, divergence angle, and polarization mode dispersion.

Chapter 5 In this chapter we explore the single polarization single mode operation of the HiBi photonic crystal fiber with special efforts devoted to design practical polarizing photonic crystal fiber at 1.3μm and 1.55μm. Section 5.1 reviews the principle of polarizing fiber and available realization methods. Section 5.2 presents the details for designing single polarization single mode photonic crystal fiber. In section 5.3 we validate the design methodology by calculating the polarization dependent confinement loss and effective mode area. Finally, we consider the practical butt

coupling efficiency to conventional single mode fiber and optimize the structural parameters of PCFs for operation at 1.3μm and 1.55μm.

Chapter 6 This chapter presents a general discussion of two-mode PCF and its basic modal properties in section 6.1. Section 6.2 discusses the possibilities of realizing two-mode operation by a Hi-Bi PCF. In section 6.3 we theoretically investigate a commercial available two-mode operation of Hi-Bi PCF in detail and describe the modal properties for future reference.

Chapter 7 This chapter starts with the principle of two-mode interferometer (section 7.1). Then the two-mode PCF interferometric sensor for strain and temperature sensing are experimentally demonstrated in section 7.2 and section 7.3, respectively. We also present a theoretical model for analyzing the temperature sensitivity in section 7.3. With the experimental results from the previous two sections, we theoretically discuss the possibilities of using two-mode photonic crystal fiber for discriminating strain and temperature in section 7.4. The errors related to the recovery of strain and temperature is also calculated in this section.

Chapter 8 In this last chapter, all the research works are summarized in section 8.1. And the promising research fields are recommended at section 8.2.

CHAPTER 2

BACKGROUND REVIEW

In this chapter, the guiding mechanisms of PCFs are described. The main properties of the index-guiding PCF, including loss, mode cutoff, and chromatic dispersion are reviewed. A special section is devoted to the Hi-Bi PCFs, in which various birefringent PCF structures, properties, and applications are reviewed.

2.1 Guiding mechanisms

2.1.1 Conventional optical fiber

The first low-loss optical fiber was made by scientists from Corning Incorporated, with a measured attenuation of less than 20dB/km [1]. Since its invention in the early 1970's, optical fiber has found numerous applications in telecommunications, sensors, automotive, military, and industry.

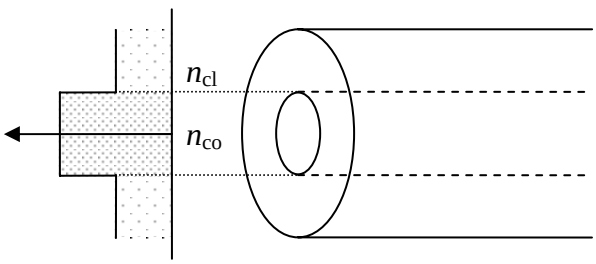

Figure 2.1 Schematic of a typical optical fiber.

The operation principle of conventional optical fiber relies on total internal reflection (TIR) [2]. A typical optical fiber consists of two components: core, and

cladding (Fig. 2.1). The core and cladding are made from two slightly different types of highly pure, solid glass, resulting a different refractive index n_{co} and n_{cl}. With the help of ray approach and Snell's law, and if $n_{co} > n_{cl}$, light propagating inside the core striking the core/cladding surface is totally reflected back into the core as long as the angle between launching light and core/cladding interface is small enough.

In order to obtain a complete description of modes of optical fiber, Maxwell's equation must be solved, and the exact solution requires six field components of great mathematical complexity. Fortunately the result can be considerably simplified by the realization that the refractive index of the core and cladding is only slightly different, so-called "weakly guiding fiber" [3]. The derivation of the simplified guided modes of the fiber comes down to solving eigenvalue β, which is called propagation constant associated with a specific mode of fiber. For all the guided modes the propagation constant should be contained in the interval of $n_{cl}k < \beta < n_{co}k$. The guided modes have finite and discrete values because of the resonance condition imposed by the eigenvalue equations. It should be mentioned that there exists radiation modes propagating in the cladding [2]. For these modes, the propagation constant lies in the range $0 < \beta < n_{cl}k$ and has infinite and continuous values.

2.1.2 Photonic crystal fibers

The general term holey fiber (HF) or microstructured optical fiber (MOF) refers to any type of fiber with an inclusion of other materials running along the longitudinal axis of fiber, whereas the term photonic crystal fiber (PCF) is intended to refer to MOF with a periodic array of cladding [4-6].

Like fabrication of conventional fibers, PCF fabrication starts from making PCF

preforms. Prefroms can be created either by stacking silica capillaries [5], or by drilling holes or extrusion [7, 8]. This process allows a high flexibility in design desirable PCF structure since solid, empty, or doped glass capillaries can be easily incorporated and the size or shape can be adjusted freely. After the desired preform has been created, it is drawn to a PCF in a conventional high temperature drawing tower. The success of this conventional technique is largely due to the capability to form of highly regular lattice of air holes and retain their arrangement during the drawing process, perhaps achieved by using pressure. Extrusion is an alternative technology to fabricate PCFs, and had already applied to other glasses [8], i.e. soft glasses and polymer, where the capillary tube form is not readily available. The flexible fabrication methods allow both solid core and hollow core PCF to be fabricated, as shown in Fig. 2.2. The two types of PCFs are based on completely different guiding mechanisms and will be discussed in further detail in the proceeding sections.

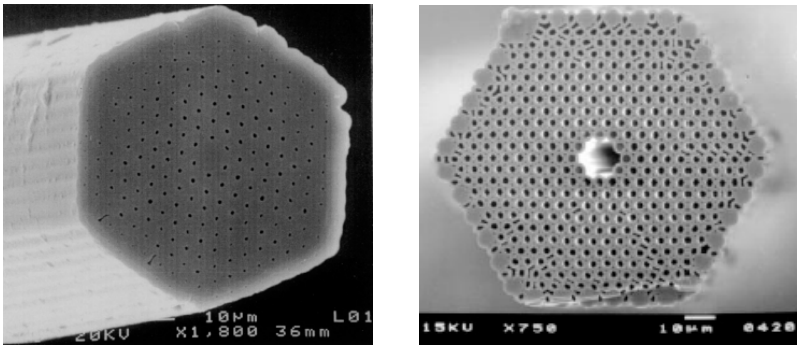

(a) (b)

Figure 2.2 Scanning electron micrograph (SEM) of the cleaved end-face of PCFs with a solid core (a) and a hollow core (b).

The large index contrast and complex index profile of PCF make it difficult to apply conventional optical fiber theory. The solution process is very complicated, and the Maxwell's equation should be solved numerically. The computation methods will

be presented in detail in Chapter 3. Prior to the mathematical solution to the problem, the basic guiding principles of PCF will be introduced in the following sections.

2.1.2.1 2-D photonic band gaps

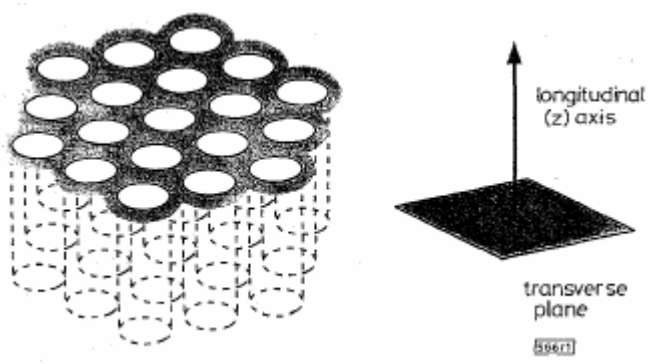

Figure 2.3 2-D photonic crystal with a non-zero propagation constant along the longitudinal axis [9].

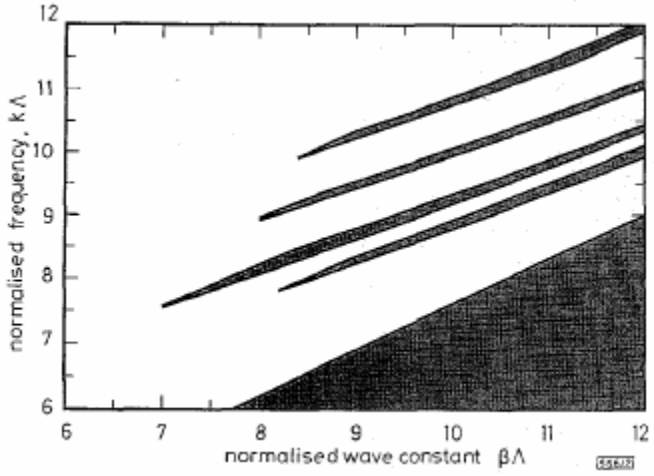

Figure 2.4 Illustration of out-of-plane PBGs for a triangular lattice cladding PCF [9].

As early as 1995 Birks et al. demonstrated that full 2-D photonic band gap exists when the longitudinal component of wave vector is non-zero, i.e. propagation out of the transverse plane [9]. The proposed structure consisted of a triangular array of air rods with an air filling fraction of 0.45 (Fig. 2.3). For a given normalized frequency $k\Lambda$ and normalized propagation constant $\beta\Lambda$, four PBGs are determined respectively, with the results given in Fig. 2.4, usually called propagation diagram. The spacing between adjacent air rods is denoted by Λ, and $k = \omega/c$ is wave number in vacuum. The bottom

black area, where the propagation constant is higher than that of the lowest order cladding mode, is the operation region by TIR. Above the black region a continuum of modes is allowed for propagation in the cladding. However, there exist the four forbidden regions, where the PBGs locate, prohibiting light propagation in the triangular lattice cladding, a feature due to the PBG effects.

2.1.2.2 Index guiding photonic crystal fiber

For index-guiding PCF, where the central capillary is replaced by a solid rod (Fig. 2.2a) [5], light is guided by modified total internal reflection (M-TIR). Intuitively, the "average refractive index" of the cladding is lower than that of the solid core, leading to a refractive index profile very similar to that of conventional optical fiber. In this case, PCF can be approximated by standard step index fiber with a high index core and a low index cladding. However, the low index cladding exhibits strong wavelength dependence, which is very different from that of the silica used for standard fiber. It is this special effect that allows index-guiding PCF to be designed with a whole new set of novel properties impossible to conventional fibers, e.g. endlessly single mode, where a single mode is guided over a very broad range of optical wavelength.

Strictly speaking, the "average refractive index" is not an average of any kind at all, but is associated with the maximal propagation constant supported by the microstructured cladding of PCF. The mode corresponding to the maximal propagation constant is the fundamental mode of the infinite photonic crystal cladding without the central defect or core, and it is called fundamental space-filling mode (FSM) [6]. Therefore, light with a propagation constant higher than the FSM can not propagate in the microstructured cladding, corresponding to the TIR operation region in Fig. 2.4.

This is analogous to the guiding principle of the conventional optical fiber (section 2.1.1), where light can not propagate in the cladding if $n_{cl}k < \beta$. The effective index of the microstructured cladding of PCF is then given by β_{FSM}/k. For all the guided modes of index-guiding PCF the propagation constant should be contained in the interval of $\beta_{FSM} < \beta < n_{co}k$.

2.1.2.3 Photonic band gap guiding PCF

In contrast to the index-guiding PCF, where a high refractive index core is surrounded by a cladding with a low refractive index, the PBG PCF permits leakage-free transmission in a low-index core (Fig. 2.2b) [4]. The PBG effect exhibited by the photonic crystal cladding makes PCF is operated physically different from that of the conventional fibers, and also from the index-guiding PCFs. Light with frequencies within a PBG is not allowed to propagate inside the photonic crystal. Therefore, if a defect is introduced into the photonic crystal, light can only propagate at the defect region. This opens up new possibilities never dreamed before: extreme low loss guidance in vacuum or compatible gas, high power delivery with low nonlinear effects, guidance of atoms, molecules through the hollow core [10], and novel fiber sensors [11].

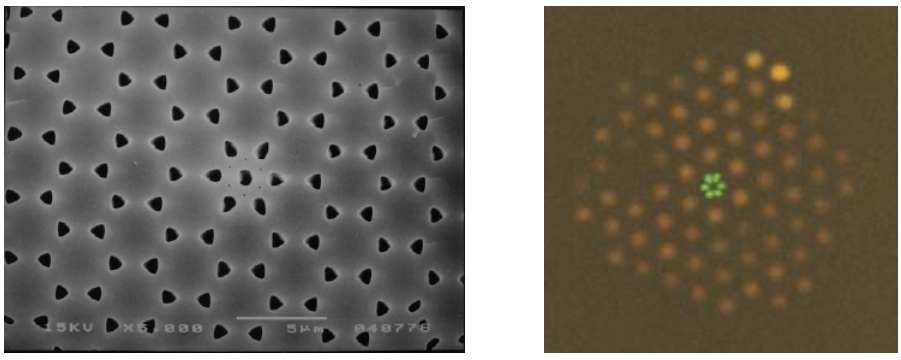

(a) (b)

Figure 2.5 (a) SEM of a cleaved end-face of a PBG fiber. (b) Near field patterns

observed with a laser source (wavelength = 458nm) [12].

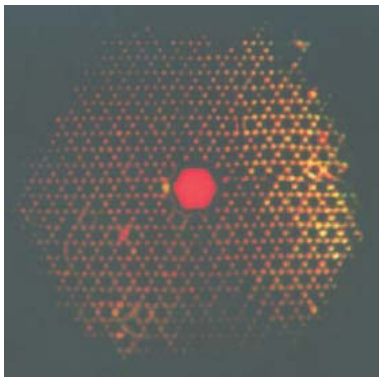

Figure 2.6 SEM of a cleaved end-face of a PBG fiber and its field intensity pattern [5].

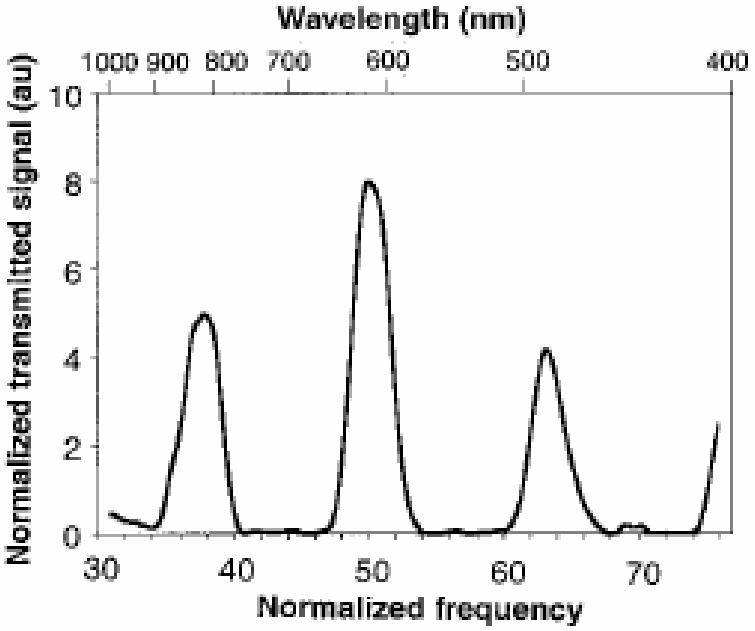

Figure 2.7 Intensity spectrum of the light transmitted through the hollow air core [5].

The first convincing demonstration of PBG PCF was based on honeycomb cladding structure (Fig. 2.5a) [12], which has the special properties of novel dispersion [13] and strong birefringence [14]. However, the guided mode is mainly distributed in silica (Fig. 2.5b), which is undesirable in certain circumstances. Cregan et al experimentally demonstrated single mode guidance in a hollow core PCF with a triangular-based PBG cladding (Fig. 2.6) [5]. When it was illuminated with a tungsten

halogen lamp, the central hollow air hole was found to be filled with a color light. Further examination of the transmission spectra by using a conventional multimode fiber showed more than one band of transmission existed, covering part of the visible spectrum and extending to the infrared (Fig. 2.7). The guidance loss for each of the transmission band is small, which can be definitely attributed to the PBG effect of the cladding.

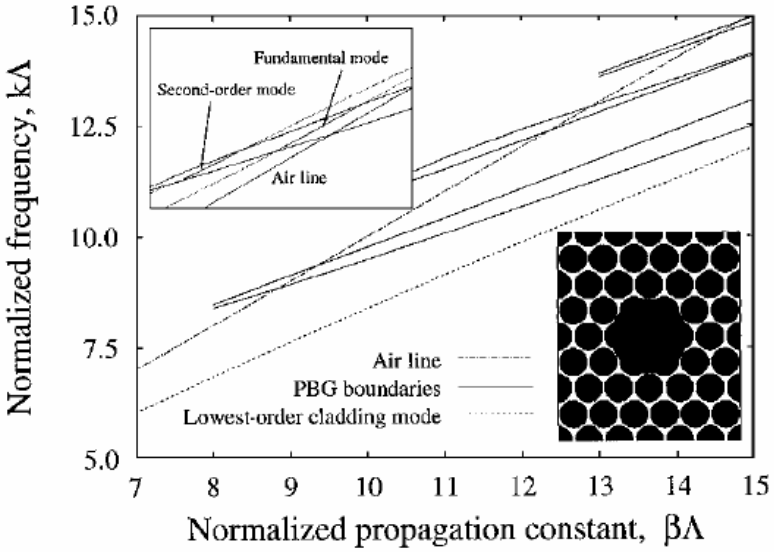

Figure 2.8 Variations of photonic bandgaps with the normalized propagation constant [15].

The use of microstructure cladding with a PBG effects makes it possible to guide light in a hollow air core. However, the PBG alone is not enough to obtain air-guiding PBG fibers. The PBG should overlap a special case of $\beta\Lambda = k\Lambda$, corresponding to light propagating in a homogeneous medium with a refractive index of 1.0, e.g. air or vacuum. Therefore, when a central defect of air or vacuum is introduced, light can propagate in the defect but can't escape this defect because of the PBG cladding. This was theoretically analyzed by Broeng et al [15] and the results are shown in Fig. 2.8. The full analysis reveals the presence of two core modes with their traces shown at the top left inset for a normalized propagation constant interval from $\beta\Lambda = 7.8$ to 9.3 and a

normalized frequency interval from kΛ = 8.1 to 9.9. The bottom right inset shows the cross-section of the air-guiding PCF. As can be seen from Fig. 2.8, there exist three PBGs for the interval from βΛ = 7.0 to 15, but only within a narrow interval do they overlap the air line. Within the PBG, both modes were found to be confined within the central air core, and the value of the normalized frequency range was determined to be 0.75 approximately. Further detailed numerical results confirmed this well-confined fundamental mode (kΛ = 9.0) and second mode (kΛ = 8.5).

2.2 Main properties of index-guiding PCFs

2.2.1 Basic loss properties

2.2.1.1 Optical attenuation

A PCF has the potential to achieve lower loss than the conventional fibers in that it is composed of only pure silica glass and doesn't suffer from the scattering loss introduced by doped ion in standard fiber. Moreover, the PBG PCF is capable to guide light in air, allowing ultra low loss and ultra low nonlinearity. Since its first fabrication, the attenuation loss of PCF has been dramatically reduced [16-20]. Early PCF had an attenuation loss of 0.24dB/m and the length is limited to tens of meters [16]. In the beginning of 2002, it was rapidly reduced to 1dB/km [17] and a record level of 0.28dB/km in the following year [18]. The fiber length has been extended to >10km which make PCF a promising candidate for future transmission media. A 100-meter length of air core PBG fiber with a minimum loss of 13dB/km at 1550nm has been reported in [20]. These improvements are attributed to the high purity glass prepared by the vapor-phase axial deposition technique and by eliminating the OH absorption

[21-22].

A proper designed structure, i.e. hole diameter d and hole pitch Λ, is the first step to realize a low loss PCF, and the confinement loss contribution should be minimized to a adequately low level because of the leaky nature of PCF. The ratio of hole diameter d to hole pitch Λ, or d/Λ, should be designed to large enough but ensuring a single mode operation at the same time because a large value of d/Λ potentially makes the PCF multi-mode. Optical confinement loss α (dB/km) of PCF with sufficiently reduced confinement loss can be expressed as [23]

$$\alpha = A/\lambda^4 + B + \alpha_{OH} + \alpha_{IR} \tag{2.1}$$

where *A*, *B*, α_{OH}, and α_{IR} are Rayleigh scattering coefficient, imperfection loss, and OH and infrared absorption loss, respectively. Among these loss components, scattering loss and OH absorption loss are dominant in today's PCFs. Both the intrinsic OH ions in fiber preforms and OH ions penetrating into the core region during the fabrication process contribute to the overall OH absorption loss. Fortunately an additional dehydration process can greatly reduce the OH absorption loss from 15dB/km to 0.4dB/km at 1.38μm, and its contribution to 1.55μm is decreased from 0.15db/km to less than 0.01dB/km. The surface roughness can increase the Rayleigh scattering when the roughness is small compared with the wavelength used, which can be improved by reducing the interior surface roughness of holes and maintaining the longitudinal uniformity along the fiber. The improved fabrication process leads to a reduction of scattering loss from 2dB/km to 1db/km at 1.55μm. It is with the reduction of both the OH absorption loss and Rayleigh scattering loss that the ultra low loss PCF was fabricated.

2.2.1.2 Confinement loss

In previous section, the confinement loss of PCF is assumed to be small enough so that its effect doesn't have to be taken into considerations. This is based on the assumption that the cladding is infinitely extended and the material is lossless, which is just as most numerical method using periodic boundary conditions treated [24-25]. However, this does not apply to the real PCF, where only a finite numbers of air hole rings is made in practice. The confinement loss is due to the finite numbers of air holes consisting of the PCF cladding even in the absence of material absorption loss or scattering loss. Various numerical methods have been used to investigate the leaky nature of the PCFs [26-31]. It should be mentioned here that other loss mechanisms discussed in the previous section are not considered when investigating the leakage property of PCFs.

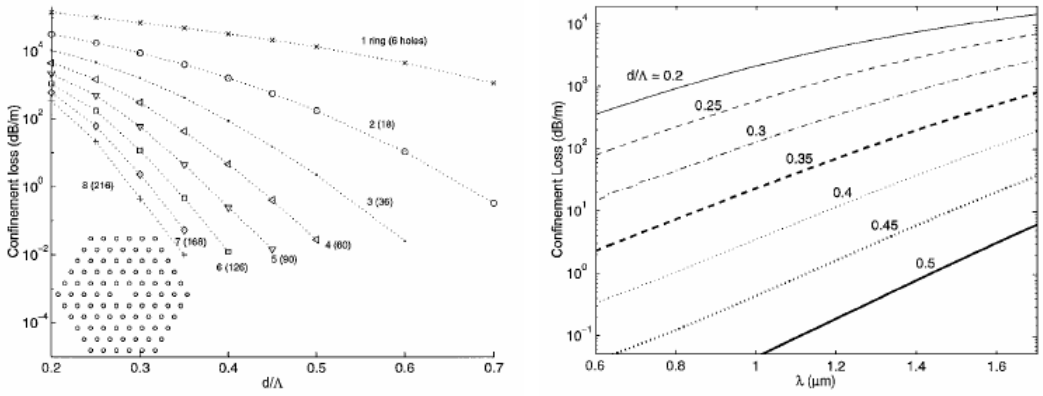

(a) (b)

Figure 2.9 (a) Confinement loss of a triangular lattice PCF as a function of the number of rings and hole diameter to pitch ratio (d/Λ). (b) Confinement loss as a function of wavelength for a triangular lattice PCF with a fixed hole pitch of 2.3μm [26].

White et al firstly reported their study on the finite cladding effect by using a full vector multipole method [26]. For an index-guiding PCF with a hole pitch Λ = 2.3μm,

the confinement loss of the fundamental mode at $\lambda = 1.55\mu m$ as a function of different numbers of air-ring and different d/Λ ratio is shown in Fig. 2.9a. As can be seen from the figure, PCFs with small hole size and less number of rings experience a higher loss, and the confinement loss decreases rapidly as hole diameters and number of rings are increased. This can be easily understood because it is the air holes that ultimately provide the confinement for the light field. The wavelength dependent confinement loss is shown in Fig. 2.9b, where it increases smoothly with the wavelength, implying the light is less confined in the core region at longer wavelengths.

2.2.1.3 Bending losses

In conventional optical fiber the single-mode bandwidth is limited by the higher order mode cutoff at short wavelengths and macro-bending loss at long wavelength. However, the PCF exhibits a very different bending characteristic [6, 32-37]. Both the short- and long-wavelength bend-edge are limited by the macro-bending and the short-wavelength bend-edge is of practical interests since the long-wavelength bend-edge occurs for $\lambda >> \Lambda/2$ [33] and it is within the non-transparent window of silica for typical large mode area (LMA) PCFs. Since the refractive index of core mode and cladding mode is strongly wavelength dependent, this index difference counteracts the $1/\lambda$ dependency of V-parameter of PCF, resulting in $V_{PCF} \rightarrow V_0$ for $\lambda \rightarrow 0$ where V_0 is a constant dependent on d/Λ [38]. This implies the refractive index difference decreases with the decreasing wavelength and correspondingly the field confinement will decrease. Therefore, macro-bending loss at short wavelength can be observed [33]. Generally, the bending losses increases with increasing mode areas, and PCFs and standard fibers will experience similar bend loss if they have similar mode areas [32].

Further investigation shows PCFs are found to have a significantly larger bandwidth than the conventional optical fiber with an identical mode field diameters [35], which can be utilized to realize LMA fiber with enhanced bending resistant properties.

2.2.2 Number of modes

2.2.2.1 Definition of V-parameter

In the case of conventional optical fiber, the *V*-parameter plays a central role in the description of the number of guided modes, the cutoff criterion, and the MFD. *V*-parameter of conventional step-index fiber (SIF) is given by [2]

$$V_{SIF} = k_{\perp} a = k \cdot \sin\theta \cdot a = \frac{2\pi}{\lambda} a \sqrt{n_{co}^2 - n_{cl}^2} \tag{2.2}$$

where λ is the wavelength, a is the core radius, n_{co} and n_{cl} are the core and cladding index, respectively. $k_{\perp}$ is the transverse projection of the free space wave number $k = 2\pi/\lambda$, and NA = $\sin\theta$ is the numerical aperture. An optical fiber is said to be multimode if $V_{SIF} >> 1$, when many bounded modes are supported to propagate within the core. However, when V_{SIF} is sufficiently small so that only the two degenerate modes, or the fundamental mode, can propagate, the fiber is said to be single-moded. For a conventional SIF, it is single-moded when $V_{SIF} < 2.405$. In the context of PCF, the first attempt to obtain an expression for the *V*-parameter is based on an equivalent SIF [6]. Up to date various definitions of *V*-parameter has been proposed [4, 39]. However, it seems that all of this attempts have faced the same problem of choosing a meaningful value of radius *a*. For example, although Ref [6] suggested some specific values, including the hole pitch Λ, they concluded that all of them are arbitrary choices, which may lead to the defined *V*-parameter arbitrary. Mortensen et al pointed out that the

problem is not a matter of defining a core radius but defining the natural length scale [40]. For an index-guiding PCF with a triangular lattice of air holes, the formulation of the *V*-parameter is given by [40]

$$V_{PCF} = \frac{2\pi}{\lambda}\Lambda\sqrt{n_{FM}^2 - n_{FSM}^2} \tag{2.3}$$

where n_{FM} and n_{FSM} are the refractive index of the fundamental mode and FSM, respectively. Similar to the counterpart of conventional fiber, the *V*-parameter of PCF provides plenty of information about the number of guided modes [40] and mode field radius [41].

2.2.2.2 Modal cutoff

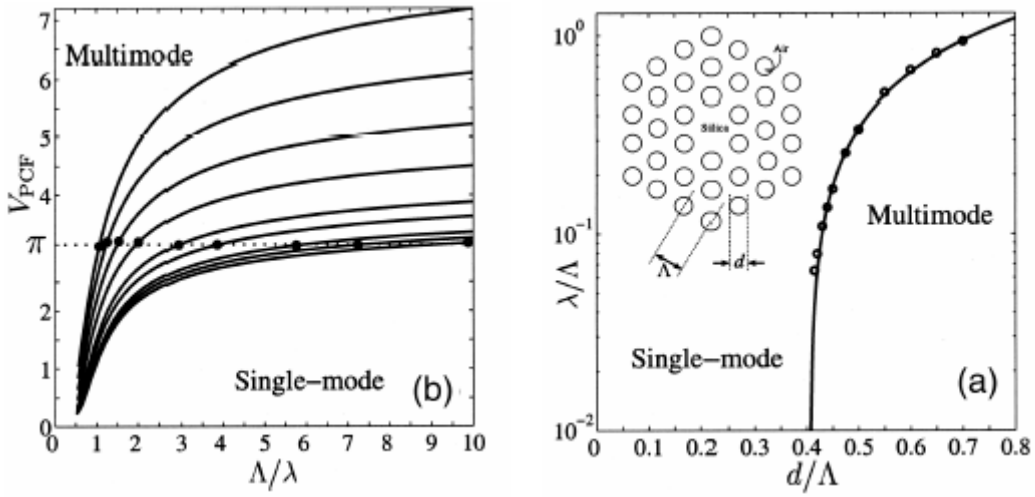

(a) (b)

Figure 2.10 (a) V_{PCF} as a function of Λ/λ for varying d/Λ from 0.43, 0.44, 0.45, 0.475, 0.50, 0.55, 0.60, 0.65, 0.70. (b) Single-mode – multimode phase diagram. Solid line shows solutions to equation 2.xx and circles correspond to solutions to $V_{PCF} = \pi$ [40].

It was argued in [40] that the second-order mode cutoff can be associated with $V_{PCF} = \pi$. And this conclusion is indeed identical to the single-mode-multimode boundary obtained by multipole method [42]. Fig. 2.10(a) shows the V_{PCF} as a function of wavelength for various values of d/Λ. With the decreasing of wavelength, the

V-parameter approaches a constant value, which depends on d/Λ. The horizontal dotted line shows $V_{PCF} = \pi$ and the black dots shows the cutoff wavelength from the empirical expression [42]

$$\lambda/\Lambda \approx \alpha\left(d/\Lambda - 0.406\right)^{\gamma} \tag{2.4}$$

where α = 2.80±0.12, and γ = 0.89±0.02. As can be seen from Fig. 2.10a good agreement can be found between these two criteria. The phase boundary shown in Fig. 2.11b provides more direct information about the mode cutoff and was confirmed experimentally in various index-guiding PCFs [43].

In general the PCF with d/Λ < 0.43 supports a single-mode and is so-called endlessly single mode, and for d/Λ > 0.43 the PCF support a second-order mode at wavelength smaller than the cutoff wavelength. For the experimental determination of the cutoff wavelength the transmission intensity as a function of wavelength is recorded and a significant difference is expected because of the very lossy nature of high-order mode when approaching the cutoff wavelength. However, it seems the alternative cutback technique fail to predicate the cutoff wavelength because of the less sensitivity to bending of the higher order modes in PCF, which can be attributed to the high NA of these high-order modes than that of the standard fiber [43].

2.2.3 Chromatic dispersion

The chromatic dispersion (CD) plays an important role in both linear and nonlinear phenomena in conventional fibers optics [44], and it leads researcher to explore this property for PCFs from all aspects. Both experimental and theoretical works have been devoted to this interesting subject, and PCFs have shown to possess unusual dispersion features unavailable to conventional optical fibers. PCFs can be engineered to have a

zero dispersion point from 500nm to 1.3μm [45] (Fig 2.11), making them useful for nonlinear applications such as soliton generation [46] and super continuum generation [47]. This novel property is a result of the strong waveguide dispersion exhibited by index-guiding PCF. For the small pitch of PCF used in Ref [45], the core diameter is in the scale of optical wavelength and thus waveguide dispersion dominates in the overall dispersion. In fact, the zero dispersion wavelengths can be precisely controlled to any wavelength by properly adjusting the waveguide dispersion and material dispersion, which is the basic idea behind the design of PCFs with ultra-flattened dispersion (Fig. 2.12) [48]. Two ultra-flattened dispersion PCFs with a dispersion of 0 ± 0.6ps/nm·km from 1.24μm – 1.44μm wavelength and 0 ± 1.2ps/nm·km from 1μm – 1.6μm have been demonstrated (Fig. 2.12).

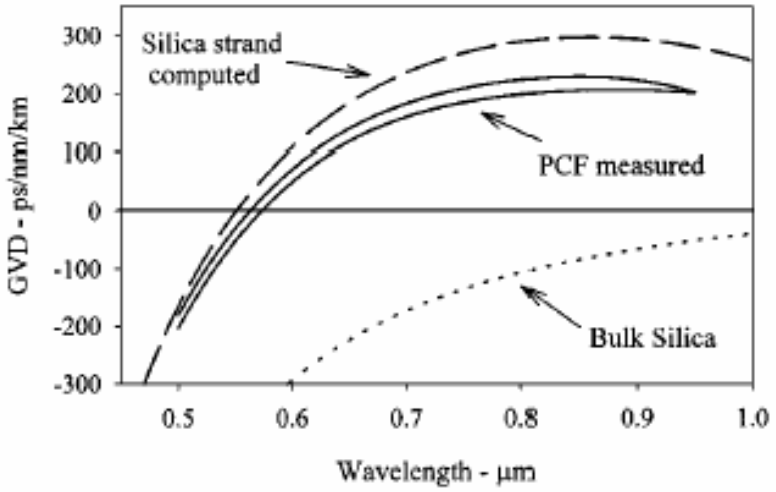

Figure 2.11 Chromatic dispersion curve (solid line) for PCF with d = 0.62μm and Λ = 1μm. Two polarization states of the fundamental mode can be clearly observed for this PCF. The broken line shows the computed results by modeling the PCF as a silica strand surrounded by air. The dotted line indicates the CD of pure bulk silica. [45]

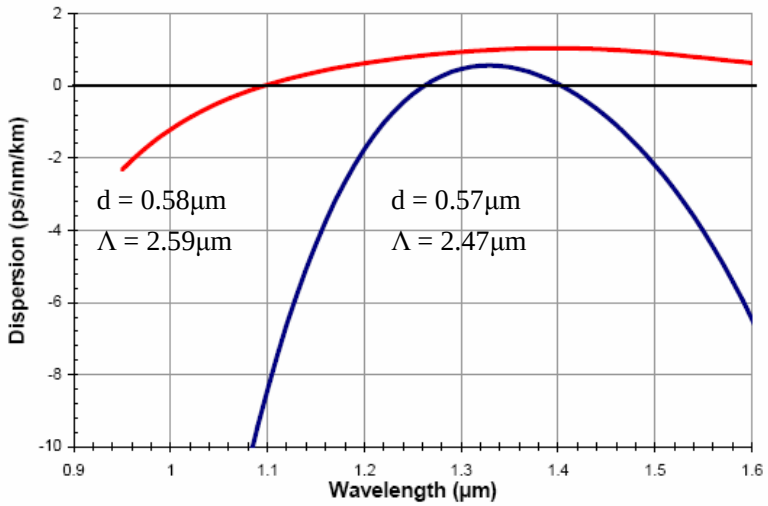

Figure 2.12 Measured dispersion for ultra flattened dispersion PCF with 11 rings of air holes [48].

In order to achieve ultra-flattened dispersion in PCFs, the influence of pitch Λ, hole diameter d, and number of hole rings N_r should be taken into consideration systematically [49-50]. Therefore, early theoretical predictions for dispersion of PCF by using silica strand approximation or full-vector method with a periodic boundary condition is inherently error-leading.

For a fixed hole diameter of 0.8μm the dispersion as a function of wavelength and different pitch is shown in Fig. 2.13 (a), where a small pitch value generates large oscillations in the dispersion curve and more than one zero dispersion wavelength can be found. With the increase of pitch Λ, equivalently increasing the core size of PCF, the dispersion becomes flattened and more close to the material dispersion, which is an indication of the reduced waveguide dispersion. This can also explain the oscillation dispersion behavior of PCF with a fixed pitch of 1.55μm but different air hole diameter.

For practical fabrication of PCF, three rings of holes will introduce huge confinement loss [26]. One can reduce the loss efficiently by increasing the number of

rings of holes N_r, but the dispersion curves will be modified correspondingly. The influence of N_r on the dispersion curve is shown in Fig. 2.14. As shown in Fig. 2.14a, the dispersion decreases as the increase of number of rings N_r. But the dispersion converges to a constant when the number of rings N_r increases (Fig. 2.14b). This convergence behavior differs for different wavelength: the larger the wavelength, the slower the convergence speed. It is related to the mode field of PCF, which is less influenced by increasing the number of rings. At longer wavelength the field is less confined and the convergence speed becomes slower.

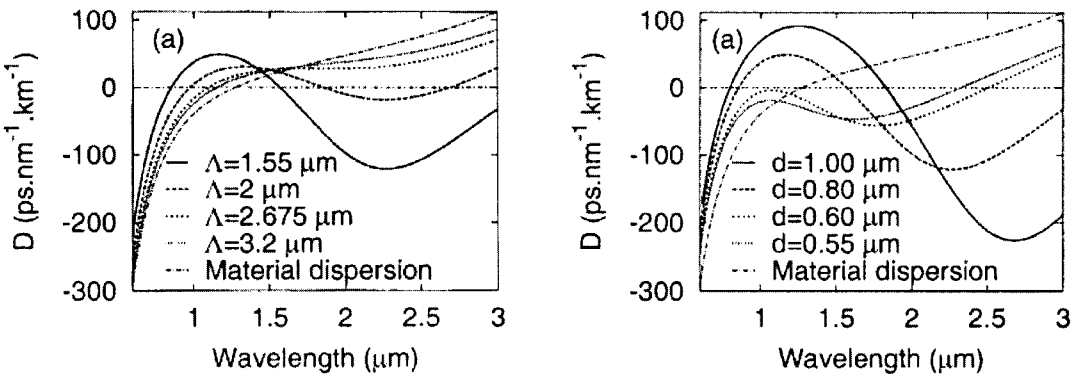

Figure 2.13 Dispersion for a three ring PCF as a function of wavelength and (a) pitch Λ, d = 0.8μm. (b) hole diameter d, Λ = 1.55μm [50].

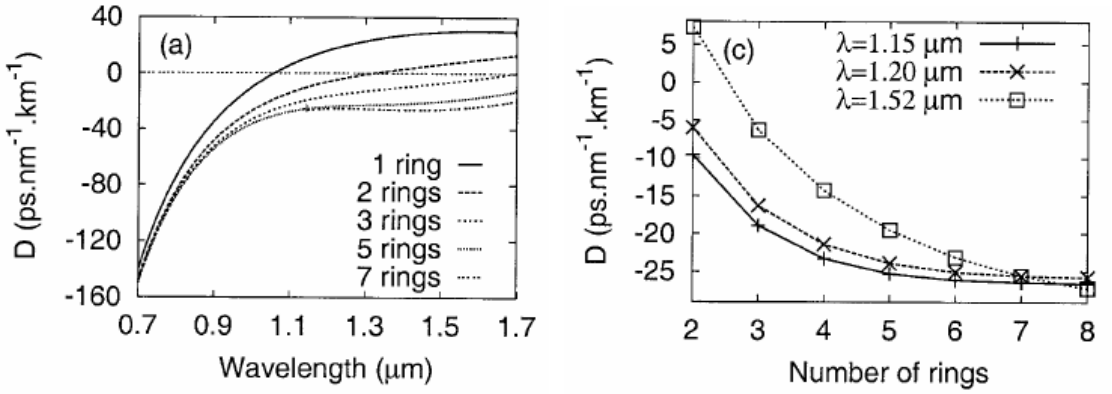

(a) (b)

Figure 2.14 (a) Dispersion as a function of wavelength and number of rings N_r. (b) Dispersion for three discrete wavelength as a function of the number of rings for PCF with d = 0.5μm and Λ = 2.0μm [50].

2.3 Hi-Bi PCF

Due to the highly flexibility during the fabrication process of PCFs, large birefringence can be introduced straightforwardly. With the general six- or four-fold symmetries the fundamental modes of PCFs are found to be doubly degenerate [51-53], as in conventional optical fibers. However, if the symmetry is broken into two-fold symmetry, e.g. by introducing different air-holes along the two principle axis [54-55] or by local elongation of core region [56-57], the degeneracy is lift and PCF becomes Hi-Bi. Further more, if the PCF is designed such that one of the polarization modes is suppressed, a single-polarization single-mode (SPSM) PCF can be realized [58-59].

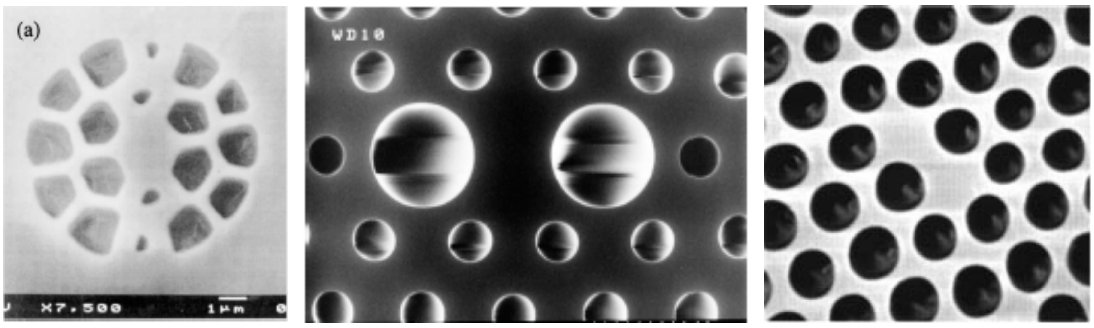

(a) (b) (c)

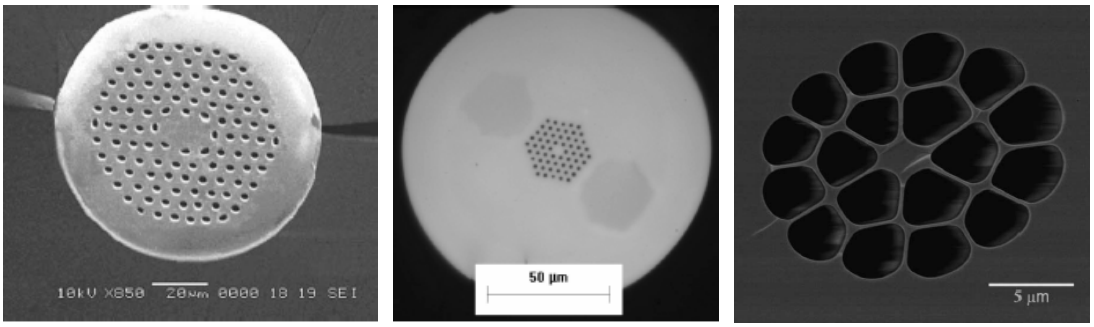

(d) (e) (f)

Figure 2.15 SEM of various Hi-Bi PCFs

2.3.1 Hi-Bi PCF with asymmetrical hole size in the cladding

The first Hi-Bi PCF was reported by Ortigosa-Blance et al in 2000 [54]. Anisotropy was intentionally introduced by careful positioning of capillaries with same outer diameter but different wall thickness, leading to a two-fold symmetry (Fig. 2.15a). The beat length at 1.55μm was measured to be 0.42mm, corresponding to a modal birefringence of 3.7×10^{-3}, which is an order of magnitude higher than that of typical conventional Hi-Bi fibers. We have conducted detailed investigation for Hi-Bi PCF with a similar structure, and the results will be discussed in Chapter 4.

Suzuki et al at NTT Corporation reported for the first time an ultra-low loss Hi-Bi PCF with 1.3dB/km transmission loss and crosstalk less than -22dB at 1.55μm [55]. Two opposite air holes near the core region are enlarged so that the effective index of the orthogonal axis becomes non-degenerate (Fig. 2.15b). The ratio (d_1/d_2) between the diameters of two big air-holes (d_1) and that of the cladding air-holes (d_2) determines the magnitude of birefringence. A birefringence of 1.4×10^{-3} at 1.55μm was measured when the ratio is set to 0.40 [55]. When the ratio is further increased to the extent that the effective index of one of the polarization states is lower than that of the cladding, or FSM, the mode becomes leaky and thus unguided [59]. Fig. 2.17 shows the spectral

loss profile for both of the polarization modes for the SPSM PCF. A polarization dependent loss (PDL) of 196dB/km and 19dB/km was obtained for 1.55μm and 1.30μm, respectively. We conducted detailed investigation on this type of PCF, including the design of SPSM PCF, two-mode PCF and applications. The results will be presented in Chapter 5 - 7.

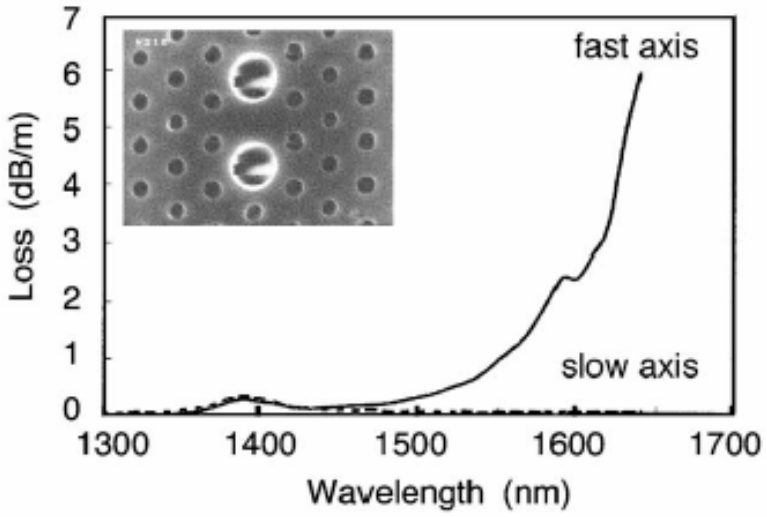

Figure 2.17 spectral loss profiles for the two orthogonal modes in 2-meter SPSM PCF [59].

2.3.2 Hi-Bi PCF with asymmetrical core

The anisotropy can also be introduced by using elliptical air-holes to form the cladding [56], but this makes the fabrication process hard to control. Through asymmetric core design, i.e. two neighboring air holes in the central are replaced by silica rods (Fig. 2.15c – Fig. 2.15d), Hi-Bi PCF can be conveniently realized [57, 60]. Both of these PCFs yield a birefringence of ~10^{-3} for the fundamental mode at 1.55μm. However, this type of PCF is prone to be multi-mode although a high birefringence can be obtained.

2.3.3 Hi-Bi large mode area PCF

Instead of changing the geometrical structure of PCF, Folkenberg et al demonstrated a Hi-Bi PCF by using stress-applying rods (Fig. 2.15e) [61-62]. The rods have a different

thermal expansion coefficient than that of the silica, resulting in a built-in stress in the fiber when it is cooled down below the softening temperature of silica. Because of the elasto-optic effect arising from the stress field, birefringence is introduced. The core and cladding region of this Hi-Bi PCF resembles those of the LMA PCF, where the air hole diameter d and pitch Λ are chosen to support single-mode operation in a wide optical wavelength. This PM PCF has a relatively lower birefringence in the order of 1.5×10^{-4} independent of wavelength, which is attributed to the screening of the strain field by the air holes. However, the Hi-Bi PCF inherits the endlessly-single-mode property and provides large mode field diameters. Further experimental study shows the relative temperature sensitivities of the phase and group delay for a small core Hi-Bi PCF is 100 times smaller than that of a standard PANDA fiber [62]. Therefore, this Hi-Bi PCF is a valuable candidate for polarization-maintaining applications demanding high temperature stability.

Through proper stress applying parts design, this Hi-Bi PCF can also be made to support only one of the orthogonal polarization states (Fig. 2.18). For wavelength above 850nm, the PCF act as a Hi-Bi PCF discussed previously with attenuation lower than 5dB/km. Within the 220nm (620nm to 840nm) single polarization bandwidth, which is defined as the wavelength range corresponding to 100dB/km attenuation, the PCF is SPSM and has a core size as large as 19.7μm, allowing Ti:Sapphire and IR light delivery without nonlinear effects or material damage.

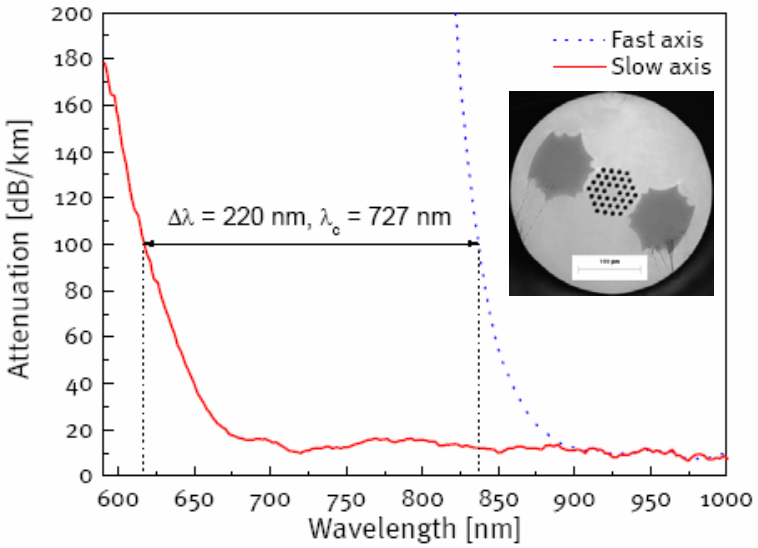

Figure 2.18 Spectral loss profile for the two orthogonal modes [63].

2.4 Summary

We have briefly reviewed the guiding mechanisms of conventional optical fibers, index-guiding and PBG-guiding PCFs. The main properties of index-guiding PCF, including loss mechanisms, mode cut-off, and dispersion, are outlined. The final section is devoted to a variety of Hi-Bi PCFs, which are the main topic of this PhD thesis and will be treated in detail in the following chapters.

References for Chapter 2

1. F.P. Kapron, D.B. Keck, R.D. Maurer, “Radiation losses in glass optical waveguides,” *Appl. Phys. Lett.*, vol. 17, pp. 423-425, 1970.
2. A.W. Snyder, and J.D. Love, *Optical waveguide theory*, Chapman and Hall, 1983.
3. D. Gloge, “Weakly guiding fibers,” *Appl. Opt.*, vol. 10, pp. 2252-2258, 1971.

4. J.C. Knight, T.A. Birks, P.St.J. Russell, D.M. Atkin, “All-silica single-mode optical fiber with photonic crystal cladding,” *Opt. Lett.*, vol. 21, pp. 1547-1549, Oct 1996.
5. R.F. Cregan, B.J. Mangan, J.C. Knight, et al., “Single-mode photonic band gap guidance of light in air,” *Science*, vol. 285, pp. 1537-1539, Sept 1999.
6. T.A. Birks, J.C. Knight, and P.St.J. Russell, “Endlessly single-mode photonic crystal fiber,” *Opt. Lett.*, vol. 22, pp. 961-963, July 1997.
7. M. van Eijkelenborg, M. Large, A. Argyros, J. Zagari, et al, “Microstructured polymer optical fibre,” *Opt. Express*, vol. 9, pp. 319-327, 2001.
8. P.St.J. Russell, “Photonic crystal fibers,” *Science*, vol. 299, pp. 358-362, 2003.
9. T.A. Birks, P.J. Roberts, P.St.J. Russell, D.M. Atkin, and T.J. Shepherd, “Full 2-D photonic bandgaps in silica/air structures,” *Electron. Lett.*, vol. 31, pp. 1941-1943, Oct 1995.
10. F. Benabid, J. Knight, and P. Russell, "Particle levitation and guidance in hollow-core photonic crystal fiber," *Opt. Express*, vol. 10, pp. 1195-1203, 2002.
11. Y.L. Hoo, W. Jin, C.Z. Shi, et al. “Design and modeling of a photonic crystal fiber gas sensor,” *Appl. Opt.*, vol. 42, pp. 3509-3515, Jun 2003.
12. J.C. Knight, J. Broeng, T.A. Birks, P.St.J. Russell, “Photonic band gap guidance in optical fibers,” *Science*, vol. 282, pp. 1476-1478, Nov 1998.
13. J. Broeng, D. Mogilevstev, S.E. Barkou, and A. Bjarklev, “Photonic Crystal Fibers: A New Class of Optical Waveguides,” *Opt. Fiber. Tech.*, vol. 5, pp. 305-330, July 1999.
14. A. Bjarklev, J. Broeng, S.E. Barkou, E. Knudsen, et al, “Polarization properties of honeycomb-structured photonic bandgap fibres,” *J. Opt. A*, vol. 2, pp. 584-588,

2000.

15. J. Broeng, S. Barkou, T. Sndergaard, and A. Bjarklev, “Analysis of air-guiding photonic bandgap fibers,” *Opt. Lett.*, vol. 25, pp. 96-98, 2000.
16. P. Bennett, T. Monro, and D. Richardson, “Toward practical holey fiber Technol.: fabrication, splicing, modeling, and characterization,” *Opt. Lett.*, vol. 24, pp. 1203-1205, 1999.
17. K. Tajima, K. Nakajima, K. Kurokawa, N. Yoshizawa, and M. Ohashi, “Low-loss photonic crystal fibers,” Optical fiber communications conference OFC 2002, pp. 523-524, 2002.
18. K. Tajima, J. Zhou, K. Nakajima, and K. Sato, “Ultra low loss and long length photonic crystal fiber,” Optical fiber communications conference OFC2003, PD1, 2003
19. K. Tajima, J. Zhou, K. Kurokawa, and K. Nakajima “Low water peak photonic crystal fibers,” 29th European conference on optical communication ECOC’03, pp. 42-42, 2003.
20. C.M. Smith, N. Venkataraman, M.T. Gallagher, et al., “Low-loss hollow-core silica/air photonic bandgap fibre,” *Nature*, vol. 424, pp. 657-659, Aug 2003.
21. M. Nielsen, C. Jacobsen, N. Mortensen, J. Folkenberg, and H. Simonsen, "Low-loss photonic crystal fibers for transmission systems and their dispersion properties," *Opt. Express*, vol. 12, pp. 1372-1376, 2004.
22. J. Zhou, K. Tajima, K. Nakajima, et al., “Progress on low loss photonic crystal fibers,” Optical Fiber Technol., vol. 11, pp. 101-110, Apr. 2005.
23. K. Tajima, J. Zhou, “Ultra low loss and long length photonic crystal fiber,” IEICE

Trans. on Eletron., vol. E88C, pp. 870-875, May 2005.

24. T.M. Monro, D.J. Richardson, N.G.R. Broderick, P.J. Bennett, “Holey optical fibers: an efficient modal model,” *J. of Lightwave Technol.*, vol. 17, pp. 1093-1102, 1999.
25. D. Mogilevtsev, T.A. Birks, P.St.J. Russell, “Localized function method for modeling defect modes in 2-D photonic crystals,” *J. of Lightwave Technol.*, vol. 17, pp. 2078-2081, 1999
26. T. White, R. McPhedran, C. de Sterke, L. Botten, and M. Steel, “Confinement losses in microstructured optical fibers,” *Opt. Lett.*, vol. 26, pp. 1660-1662, 2001.
27. D. Ferrarini, L. Vincetti, M. Zoboli, A. Cucinotta, and S. Selleri, “Leakage properties of photonic crystal fibers,” *Opt. Express*, vol. 10, pp. 1314-1319, 2002.
28. Y. Xu and A. Yariv, “Loss analysis of air-core photonic crystal fibers,” *Opt. Lett.*, vol. 28, pp. 1885-1887, 2003.
29. K. Saitoh and M. Koshiba, “Leakage loss and group velocity dispersion in air-core photonic bandgap fibers,” Opt. Express 11, 3100-3109 (2003)
30. M. Koshiba, K. Saitoh, “Polarization-dependent confinement losses in actual holey fibers,” *IEEE Photon. Technol. Lett.*, vol. 15, pp. 691- 693, 2003.
31. K. Saitoh, M. Koshiba, “Confinement losses in air-guiding photonic bandgap fibers,” *IEEE Photon. Technol. Lett.*, vol. 15, pp. 236- 238, 2003.
32. J. Baggett, T. Monro, and K. Furusawa, et al, “Comparative study of large-mode holey and conventional fibers,” *Opt. Lett.*, vol. 26, pp. 1045-1047, 2001.
33. T. Sorensen, J. Broeng, A. Bjarklev, et al, “Macro-bending loss properties of photonic crystal fibre,” *Electron. Lett.*, vol 37, pp. 287 – 289, Mar 2001.
34. J.C. Baggett, T.M. Monro, K. Furusawa, et al, “Understanding bending losses in

holey optical fibers," *Opt. Communications*, vol. 227, pp. 317-335, Nov 2003.

35. M. Nielsen, J. Folkenberg, N. Mortensen, and A. Bjarklev, "Bandwidth comparison of photonic crystal fibers and conventional single-mode fibers," *Opt. Express*, vol. 12, pp. 430-435, 2004.
36. M. Nielsen, N. Mortensen, M. Albertsen, et al, "Predicting macrobending loss for large-mode area photonic crystal fibers," *Opt. Express*, vol. 12, pp. 1775-1779 2004.
37. T.P. Hansen, J. Broeng, C.Jakobsen, et al, "Air-guiding photonic bandgap fibers: spectral properties, macrobending loss, and practical handling," *J of Lightwave Technol.*, vol. 22, pp. 11- 15, Jan 2004.
38. M. Nielsen and N. Mortensen, "Photonic crystal fiber design based on the V-parameter," *Opt. Express*, vol. 11, pp. 2762-2768, 2003.
39. J. Knight, T. Birks, P. Russell, and J. de Sandro, "Properties of photonic crystal fiber and the effective index model ," *J. Opt. Soc. Am. A*, vol. 15, pp. 748-752, 1998.
40. N. Mortensen, J. Folkenberg, M. Nielsen, and K. Hansen, "Modal cutoff and the V parameter in photonic crystal fibers," *Opt. Lett.*, vol. 28, pp. 1879-1881, 2003.
41. M. Nielsen, N. Mortensen, J. Folkenberg, and A. Bjarklev, "Mode-field radius of photonic crystal fibers expressed by the V parameter," *Opt. Lett.*, vol. 28, pp. 2309-2311, 2003.
42. B. Kuhlmey, R. McPhedran, and C. Martijn de Sterke, "Modal cutoff in microstructured optical fibers," *Opt. Lett.*, vol. 27, pp. 1684-1686, 2002.
43. J. Folkenberg, N. Mortensen, K. Hansen, T. Hansen, H. Simonsen, and C. Jakobsen,

"Experimental investigation of cutoff phenomena in nonlinear photonic crystal fibers ," *Opt. Lett.*, vol. 28, pp. 1882-1884, 2003.

44. G. Agrawal, *Nonlinear Fiber Optics*, Academic Press, 2001.
45. J.C. Knight, J. Arriaga, T.A. Birks, A Ortigosa-Blanch, et al. “Anomalous dispersion in photonic crystal fiber,” *IEEE Photon. Technol. Lett.*, vol. 12, pp. 807-809, July 2000.
46. W.J. Wadsworth, J.C. Knight, A. Ortigosa-Blanch, J. Arriaga, E. Silvestre, P.St.J. Russell, “Soliton effects in photonic crystal fibres at 850 nm,” *Electron. Lett.*, vol. 36, pp. 53-55, Jan 2000.
47. J. Ranka, R. Windeler, and A. Stentz, “Visible continuum generation in air silica microstructure optical fibers with anomalous dispersion at 800nm,” *Opt. Lett.*, vol. 25, pp. 25-27, 2000.
48. W. Reeves, J. Knight, P. Russell, and P. Roberts, “Demonstration of ultra-flattened dispersion in photonic crystal fibers,” *Opt. Express*, vol. 10, pp. 609-613, 2002.
49. G. Renversez, B. Kuhlmey, and R. McPhedran, “Dispersion management with microstructured optical fibers: ultraflattened chromatic dispersion with low losses,” *Opt. Lett.*, vol. 28, pp. 989-991, 2003.
50. B. Kuhlmey, G. Renversez, and D. Maystre, “Chromatic Dispersion and Losses of Microstructured Optical Fibers,” *Appl. Opt.*, vol. 42, pp. 634-639, 2003.
51. R. Guobin, W. Zhi, L. Shuqin, and J. Shuisheng, “Mode classification and degeneracy in photonic crystal fibers,” *Opt. Express*, vol. 11, pp. 1310-1321, 2003.
52. M. Steel, T. White, C. Martijn de Sterke, R. McPhedran, and L. Botten, “Symmetry and degeneracy in microstructured optical fibers,” *Opt. Lett.*, vol. 26, pp. 488-490,

2001.

53. M. Koshiba, and K. Saitoh, “Numerical verification of degeneracy in hexagonal photonic crystal fibers,” *IEEE Photon. Technol. Lett.*, vol. 13, pp. 1313-1315, Dec 2001.
54. A. Ortigosa-Blanch, J. Knight, W. Wadsworth, J. Arriaga, B. Mangan, T. Birks, and P. Russell, “Highly birefringent photonic crystal fibers,” *Opt. Lett.*, vol. 25, pp. 1325-1327, 2000.
55. K. Suzuki, H. Kubota, S. Kawanishi, M. Tanaka, and M. Fujita, “Optical properties of a low-loss polarization-maintaining photonic crystal fiber,” *Opt. Express*, vol. 9, pp. 676-680, 2001.
56. M. Steel, and R. Osgood, “Elliptical-hole photonic crystal fibers,” *Opt. Lett.*, vol. 26, pp. 229-231, 2001.
57. T.P. Hansen, J. Broeng, S.E.B. Libori, E. Knudsen, A. Bjarklev, J.R. Jensen, H. Simonsen, “Highly birefringent index-guiding photonic crystal fibers,” *IEEE Photon. Technol. Lett.*, vol. 13, pp. 588-590, Jun 2001.
58. K. Saitoh, and M. Koshiba, “Single-polarization single-mode photonic crystal fibers,” *IEEE Photon. Technol. Lett.*, vol. 15, pp. 1384-1386, Oct. 2003.
59. H. Kubota, S. Kawanishi, S. Koyanagi, M. Tanaka, and S. Yamaguchi, “Absolutely single polarization photonic crystal fiber,” *IEEE Photon. Technol. Lett.*, vol.16, pp. 182-184, Jan. 2004.
60. P.R. Chaudhuri, V. Paulose, C. Zhao, and C. Lu, “Near-elliptic core polarization-maintaining photonic crystal fiber: modeling birefringence characteristics and realization,” *IEEE Photon. Technol. Lett.*, vol. 16, pp. 1301-

1303, May 2004.

61. J. Folkenberg, M. Nielsen, N. Mortensen, C. Jakobsen, and H. Simonsen, "Polarization maintaining large mode area photonic crystal fiber," *Opt. Express*, vol. 12, pp. 956-960, 2004.

62. T. Ritari, H. Ludvigsen, M. Wegmuller, M. Legré, N. Gisin, J. Folkenberg, and M. Nielsen, "Experimental study of polarization properties of highly birefringent photonic crystal fibers," *Opt. Express*, vol. 12, pp. 5931-5939, 2004.

63. http://www.crystal-fibre.com/datasheets/LMA-PZ-20.pdf

CHAPTER 3

MODELING OF PHOTONIC CRYSTAL FIBER

In this chapter a general presentation of various numerical methods for modeling photonic crystal fibers is described. The basic theory of FEM, the main numerical method used for modeling PCF throughout this thesis, is then introduced. FEMLAB, which is a commercial FEM software package from COMSOL Inc., is used to simulate different types of waveguides. The modeling results are compared to the published data and good agreements are found. At the end of this chapter, I present the calculated mode field of endlessly single mode PCF and proposed a simple formula to evaluate the MFD. The formula is further used for estimating the splice loss between photonic

crystal fiber and single mode fiber.

3.1 Numerical methods for PCF modeling

3.1.1 Effective index method

Effective Index Method is one of the firstly developed methods for modeling PCF [1], but it is indeed an approximate approach to the problem. The basic idea behind this approximation is to regard the microstructured cladding as a uniform material with a properly chosen effective index (the index of fundamental space-filling mode) and PCF can be regarded as a conventional step index optical fiber. With such a simplified fiber structure, conventional well-established fiber theory can be applied to analyze the modal property of PCF. However, one difficulty arising from this effective index approach is the correct definition of the equivalent core radius.

3.1.2 Plane wave expansion method & super cell method

The plane wave expansion method was intensively used for accurate analysis of photonic crystals [2-3]. The basic principle is to express the electromagnetic (EM) field as a finite sum of plane wave basis. In order to find the solutions, it is advantageous to operate in the reciprocal space since the periodic functions can be expressed as Fourier-series expansion in terms of the reciprocal lattice vectors. This method seems straightforward but it demands intensive computation to accurately model the PCF since a large number of plane waves are required.

The super cell method [4-5] is closely related to plane wave method in that the EM field is also expanded as the sum of basis functions, i.e. Hermite-Gaussian basis functions. In a periodic structure the solutions maybe computed as Fourier series, just

like plane wave expansion method. But when a defect is introduced the structure is no longer periodic. Super cell method converts this non-periodic structure to an artificial periodic one by infinitely repeating the PCF structure with a central defect. The newly constructed periodic structure is then regarded as a combination of two separate periodic structures with different periods, which are easy to solve mathematically by taking advantage of the periodicity. However, one can't estimate the loss of modes by using super cell method because the finite confining structure is replaced with an infinite one.

3.1.3 Finite difference time domain method

Finite difference time domain method (FDTD) is one of the most powerful methods for modeling EM wave propagation. It utilizes the finite differences computed on a small space/time interval to replace the derivatives of functions in differential operators. The main drawback comes from the great difficulties when accurate representation of a complex geometry is required, where a fine grid or mesh not only takes more memory but also consumes long computation time. The other problem is that it is a time domain method, we need a frequency conversion to get the mode information. Therefore, FDTD is not a good numerical tool for modeling PCFs, and it was only reported in a few papers for analyzing PCFs [6].

3.1.4 Multipole method

Multipole method has been widely used to study PCFs and a detailed formulation and implementation of this powerful method was presented in Ref [7-8]. This method is a general extension of the multipole method previously developed for multicore conventional fibers [9-10]. Similar to plane wave expansion method, multipole method

is also finding solutions of the Helmholtz equations, but it chooses a different basis functions, i.e. Fourier Bessel series, a natural basis for harmonic functions in cylindrical coordinates. The basis functions of multipole method differentiate that of plane wave expansion method in that multipole series are localized and require a small number of terms to achieve a reasonable accuracy.

The multipole method is well suited for analyzing finite size PCF, with a solid core or an air core, which is attributed to the advantages it bears. Firstly, the method is of high accuracy and converging rapidly even when a larger number of inclusions are contained, which is an inherited advantage because this method was originally developed for analyzing the convectional fibers with inclusions. Secondly, the symmetry properties of optical waveguide, when taken into consideration, can greatly increase computation efficiency. The last but not the least advantage of this method is that it reveals both the real and the imaginary parts of the propagation constant, the latter one gives the confinement loss associated with the finite numbers of rings of air holes.

A key aspect of the multipole method is that it makes use of the circularity of the inclusions. It is therefore of high accuracy, converging sufficiently rapidly to be able to treat precisely systems that contain quite large numbers of inclusions. The finite element method, which we will discuss later in this chapter, is extremely flexible from both the geometric and material point of view, since it allows not only an easy treatment of inclusions of any shape but also anisotropic, inhomogeneous materials to be fully incorporated.

The above overview only provides a brief description of the various methods that

have been developed for PCF modeling and analysis. In the next sections I will present in relative detail of the FEM, which is used throughout this thesis for analyzing PCFs.

3.2 Finite Element Method

FEM has proved to be very successful in solving a large range of scientific problems although it was initially developed as a computer aid simulation software tool for analysis of aerospace structures. Its success quickly attracted attentions in 1970s and found its way continually in different fields, e.g. civil and mechanical engineering, and non-structural problems in fluids, thermomechanics, and electromagnetics. FEM is probably the most generally applicable and most versatile method for waveguide analysis at microwave, millimeter-wave, and optical frequencies [11-14]. In this section, the general outline of finite element method is given in the simplest form to illustrate the basic ideas behind this powerful method.

Considering an inhomogeneous waveguide filled with dielectric of the relative permeability μ_r and permittivity ε_r, we assume that the electromagnetic field has a z-dependence as $E(x,y,z) = E(x,y)e^{-jk_z z}$. From the Maxwell's equations the following vectorial wave equation is derived:

$$\nabla \times (\frac{1}{\mu_r} \nabla \times E) - k_0^2 \varepsilon_r E = 0 \tag{3.1}$$

where k_0 is the wave number in free space. Applying the variational formulation and the functional for Eq. (3.1) is given by

$$F(E) = \iint_{\Omega} \left[(\nabla \times E)^* \cdot \left(\frac{1}{\mu_r} \nabla \times E \right) - k_0^2 \varepsilon_r E^* \cdot E \right] dxdy \tag{3.2}$$

where Ω denotes the cross section of the structure to be analyzed. We discretize the

domain Ω by using the edge element, as shown in Fig. 3.1. The edges 1 to 3 are for the transverse components e_t and nodes 1 to 3 are for the longitudinal components e_z. Within each element we expand the electric field as

$$e = \begin{Bmatrix} e_t \\ e_z \end{Bmatrix} = \begin{Bmatrix} \{N\}^T \{e_t\}_e \\ \{L\}^T \{e_z\}_e \end{Bmatrix} \tag{3.3}$$

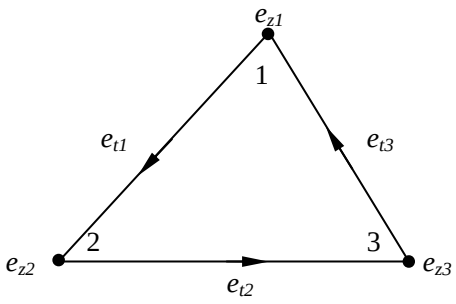

Figure 3.1 First order triangular edge element.

where $\{N\}$ and $\{L\}$ are the edge basis function and node basis function for the linear triangular element. $\{L\}$ is defined as

$$\{L\} = \begin{Bmatrix} L_1 \\ L_2 \\ L_3 \end{Bmatrix} = \frac{1}{2A_e} \begin{Bmatrix} a_1 + b_1 x + c_1 y \\ a_2 + b_2 x + c_2 y \\ a_3 + b_3 x + c_3 y \end{Bmatrix} \tag{3.4}$$

where A_e is the area of the element, and a_k, b_k, and c_k are given by

$$\begin{aligned} a_k &= x_l y_m - x_m y_l \\ b_k &= y_l - y_m \\ c_k &= x_m - x_l \end{aligned} \tag{3.5}$$

where x_k and y_k (k = 1, 2, 3) are coordinates of nodes 1 to 3 of the triangular element and subscripts k, l, m always progress modulo 3. $\{N\}$ can be defined as

$$\{N\} = \begin{Bmatrix} N_1 \\ N_2 \\ N_3 \end{Bmatrix} = \begin{Bmatrix} (L_1 \nabla L_2 - L_2 \nabla L_1) l_1 \\ (L_2 \nabla L_3 - L_3 \nabla L_2) l_2 \\ (L_3 \nabla L_1 - L_1 \nabla L_3) l_3 \end{Bmatrix} \tag{3.6}$$

where l_k is the length of each edge. The transverse electric field on each edge is further

decomposed into *x* and *y* components, and e_t can be written as

$$e_t = \begin{Bmatrix} \hat{x}e_x \\ \hat{y}e_y \end{Bmatrix} = \begin{Bmatrix} \hat{x}\{U\}^T \{e_t\}_e \\ \hat{y}\{V\}^T \{e_t\}_e \end{Bmatrix} \tag{3.7}$$

substituting Eq. (3.4) into Eq. (3.6), we obtained the edge basis function

$$\{U\} = \frac{1}{(2A_e)^2} \begin{Bmatrix} (\tilde{a}_1 + \tilde{c}_1 y) l_1 \\ (\tilde{a}_2 + \tilde{c}_2 y) l_2 \\ (\tilde{a}_3 + \tilde{c}_3 y) l_3 \end{Bmatrix}, \quad \{V\} = \frac{1}{(2A_e)^2} \begin{Bmatrix} (\tilde{b}_1 - \tilde{c}_1 x) l_1 \\ (\tilde{b}_2 - \tilde{c}_2 x) l_2 \\ (\tilde{b}_3 - \tilde{c}_3 x) l_3 \end{Bmatrix} \tag{3.8}$$

where $\tilde{a}_k$, $\tilde{b}_k$, and $\tilde{c}_k$ are given by

$$\begin{aligned} \tilde{a}_k &= a_k b_l - a_l b_k \\ \tilde{b}_k &= a_k c_l - a_l c_k \\ \tilde{c}_k &= b_l c_k - b_k c_l \end{aligned} \tag{3.9}$$

Discretizing the functional in Eq. (3.2) and applying the variational procedure, we obtain the following eigenvalue equation

$$\begin{bmatrix} [A_{tt}] & 0 \\ 0 & 0 \end{bmatrix} \begin{Bmatrix} \{e_t\} \\ \{e_z\} \end{Bmatrix} = -k_z^2 \begin{bmatrix} [B_{tt}] & [B_{tz}] \\ [B_{zt}] & [B_{zz}] \end{bmatrix} \begin{Bmatrix} \{e_t\} \\ \{e_z\} \end{Bmatrix} \tag{3.10}$$

where the matrices are assembled from their corresponding elemental matrices given by

$$\begin{aligned} [A_{tt}^e] &= \iint_\Omega \left[\frac{1}{\mu_r^e} \left(\frac{\partial\{V\}}{\partial x} - \frac{\partial\{U\}}{\partial x} \right) \left(\frac{\partial\{V\}^T}{\partial x} - \frac{\partial\{U\}^T}{\partial x} \right) - k_0^2 \varepsilon_r^e \left(\{U\}\{U\}^T + \{V\}\{V\}^T \right) \right] d\Omega \\ [B_{tt}^e] &= \iint_\Omega \frac{1}{\mu_r^e} \left[\{U\}\{U\}^T + \{V\}\{V\}^T \right] d\Omega \\ [B_{zz}^e] &= \iint_\Omega \left[\frac{1}{\mu_r^e} \left(\frac{\partial\{N\}}{\partial x}\frac{\partial\{N\}^T}{\partial x} + \frac{\partial\{U\}}{\partial y}\frac{\partial\{U\}^T}{\partial y} \right) - k_0^2 \varepsilon_r^e \{N\}\{N\}^T \right] d\Omega \\ [B_{tz}^e] &= [B_{zt}^e]^T = \iint_\Omega \frac{1}{\mu_r} \left[\{U\}\frac{\partial\{N\}^T}{\partial x} + \{V\}\frac{\partial\{N\}^T}{\partial y} \right] d\Omega \end{aligned} \tag{3.11}$$

Eliminating the longitudinal components $\{e_z\}$ from Eq. 3.10, the following eigenvalue equation for the transverse components is obtained

$$[A_{tt}]\{e_t\} = k_z^2 \left([B_{tz}][B_{zz}]^{-1}[B_{zt}] - [B_{tt}] \right) \{e_t\} \tag{3.12}$$

The propagation constant k_z and the corresponding field components e_t can be obtained

directly by solving Eq. (3.12).

3.3 FEMLAB software

3.3.1 Introduction

FEMLAB is a FEM modeling software package for the simulation of any physical process you can describe with partial differential equations (PDEs). FEMLAB is commercial software from COMSOL, Inc. It features state-of-the-art solvers that address complex problems quickly and accurately. FEMLAB consists of several different modules which enable researcher to concentrate on specific applications or a combination of multi-physics. The electromagnetics module specializes in virtually all electromagnetic field simulation from statics and quasistatics to microwaves and photonics. The static, transient and frequency domain analyses allow for material properties that are complex-valued, i.e., anisotropic, frequency or time-dependent. We're most interested in the capabilities of the electromagnetics module for mode analysis of optical waveguide with or without anisotropic media with loss. In the following sections, I'll rigorously evaluate the performance FEMLAB software by comparing the results to that of well-established theory or other numerical methods.

3.3.2 Assessment of FEMLAB for semiconductor rib waveguide analysis

In this section semiconductor rib waveguide will be analyzed by using FEMLAB, and it is demonstrated that FEMLAB can predict accurate simulation results. First, we consider a semiconductor rib waveguide (Fig. 3.2a) having a rib width W = 3μm and substrate depth $t + h$ = 1μm, where h is the etch depth. The outer slab depth t varies from 0μm to 0.9μm. Fig. 3.2b shows a typical element division profile, where only

one-half of the cross-section is taken into consideration by taking use of the symmetry nature of the rib waveguide.

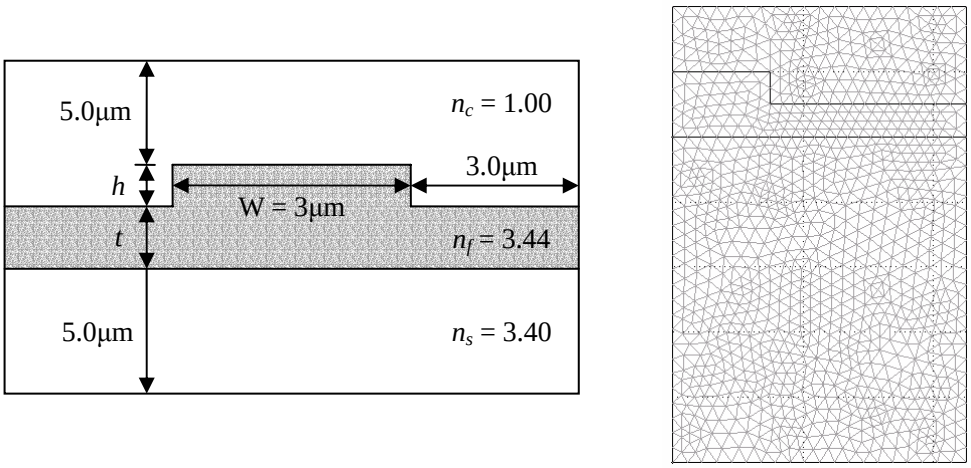

(a) (b)

Fig. 3.2 (a) Rib waveguide structure, (b) Element division profile.

Fig. 3.3 shows the normalized propagation constant *b* as a function of *t* for the two non-degenerated fundamental modes, where *b* is defined as

$$b = \frac{(\beta/k_0)^2 - n_s^2}{n_f^2 - n_s^2} \tag{3.13}$$

where β is the propagation constant and k_0 is the free space wave number. The results of vector finite element method (VFEM) with higher order mixed-interpolation type elements [15] and scalar finite difference method (SFDM) [16] are also given in Fig. 3.3. It is confirmed that the results obtained with FEMLAB are in good agreement with VFEM and SFDM.

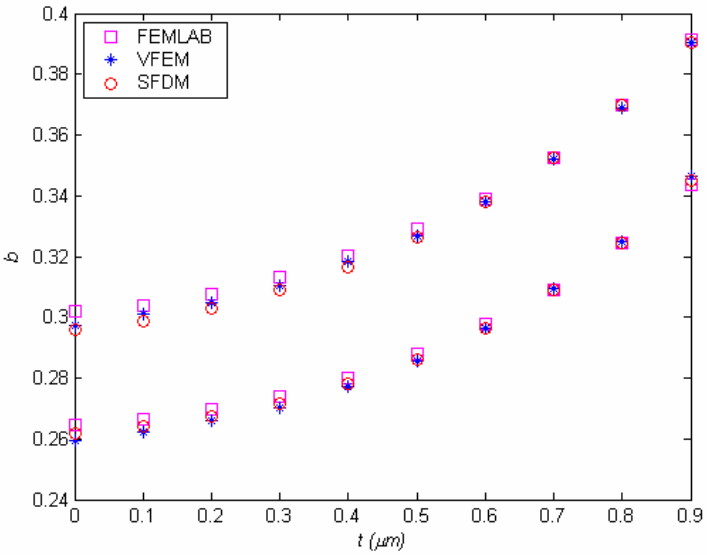

Figure 3.3 Normalized propagation constants of the rib waveguide.

3.3.3 Assessment of FEMLAB for PCF simulation

3.3.3.1 A multi-mode PCF example

In this section, I'll apply the full-vector FEM for analyzing the modal properties of PCFs. The cross section of a typical PCF is schematically shown in Fig. 3.4, where d is the hole diameter and Λ is the hole pitch. We consider a PCF with structural parameters Λ = 2.3μm, d/Λ = 0.8, and a background index of silica n = 1.457 [17]. At a wavelength of 633nm, it allows higher order modes to exist since the d/Λ is beyond the value (0.43) for endlessly single mode operation. Taking use of the symmetry nature of the cross section, only a quarter of the cross section was used during the simulation and a perfect electric or perfect magnetic conductor (PEC or PMC) is applied along the symmetric plane Γ_1 and Γ_2. PEC or PMC makes the electric field perpendicular or parallel to the boundaries, respectively. The polarization of a considered mode over a quarter of the cross-section is preserved subject to the proper choice of PEC and PMC combinations [18]. The boundary conditions for calculating the corresponding guided

modes are summarized in Table 3.1, referring to the boundaries Γ_1 and Γ_2 appearing in Fig. 3.4.

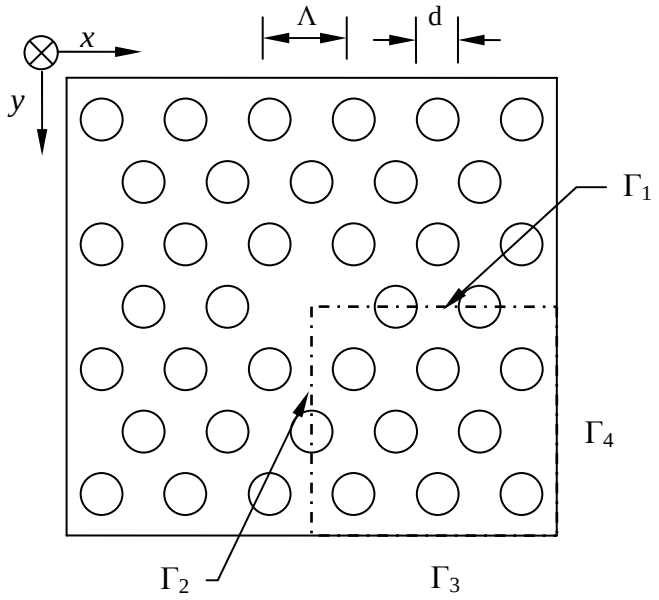

Figure 3.4 Schematic of the cross section of a PCF.

Table 3.1 Boundary conditions for calculating n_{eff}

Mode Label	Γ_1	Γ_2
HE_{11}^1, EH_{11}^2, EH_{312}, HE_{12}^2	PMC	PEC
HE_{11}^2, EH_{11}^1, EH_{311}, HE_{12}^1	PEC	PMC
TE_{01}, HE_{21}^2, EH_{21}^1	PEC	PEC
TM_{01}, HE_{21}^1, EH_{21}^2	PMC	PMC

Fig. 3.5 shows mode indices of the first 14 modes supported by this PCF. We also show the results calculated by using supercell lattice method (SLM) [17] in Fig. 3.5. For detailed comparison the results of both methods are summarized in Table 3.2, and excellent agreement was found between these two numerical methods. For an ideal PCF, the mode index of the two fundamental modes should be the same theoretically [19]. Therefore, the modal birefringence $|\Delta n|$, which corresponds to the difference

between the modal indexes of the fundamental modes, results from the error introduced by the numerical methods. It can be used to evaluate the accuracy of the algorithm: the less $|\Delta n|$ is, the more accurate the numerical method [4]. The modal birefringence $|\Delta n| = 7.5\times10^{-7}$ indicates that FEMLAB can yield very accurate results.

Table 3.2 Mode index of the first 14 modes.

Ordinal of mode	FEMLAB	SLM [17]	Label
1	1.44884671	1.44882484	HE_{11}
2	1.44884596	1.44882443	
3	1.43680859	1.43674688	TE_{01}
4	1.43645021	1.43637588	HE_{21}
5	1.43644586	1.43635241	
6	1.43624155	1.43622158	TM_{01}
7	1.42212080	1.42177752	HE_{311}
8	1.42113562	1.42112856	EH_{11}
9	1.42113364	1.42108459	
10	1.41945180	1.41946985	HE_{312}
11	1.41554257	1.41542537	HE_{12}
12	1.41554168	1.41542357	
13	1.40886545	1.40865377	EH_{21}
14	1.40884648	1.40863244	

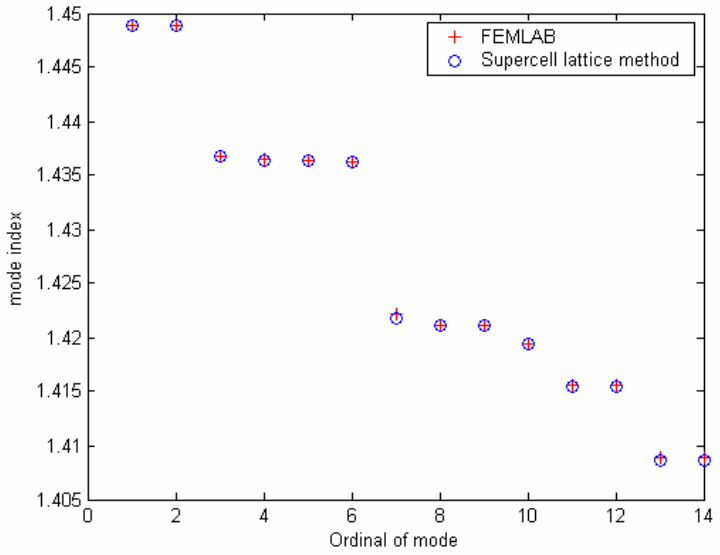

Figure 3.5 Mode index of the first 14 modes in PCF with structural parameters Λ = 2.3μm, d/Λ = 0.8, at 633nm.

3.3.3.2 Fundamental space-filling mode of PCF

In index-guiding PCF the effective index of core is higher than that of cladding, leading to the M-TIR. In other words, the effective index of the propagation mode should satisfy the following equation:

$$n_{FSM} < \frac{\beta}{k} < n_{co} \tag{3.14}$$

where n_{FSM} is the effective cladding index of the FSM of the infinite photonic crystal cladding without the central defect or core, β is the propagation constant of the propagating modes supported by the PCF, and n_{co} is the refractive index of the core. The equivalent refractive index of the cladding, n_{SFM}, can be determined by applying the full-vector FEM to the elementary piece of the cladding which act like an infinite propagation medium as shown in Fig. 3.6 [20]. The calculation of effective index of the cladding can also be categorized as *x*- and *y*-polarization with a proper setting of the boundary conditions (Table 3.3). The simulation results indicated that the two polarizations of the FSM are also degenerate.

As an example, we calculate the refractive index of the FSM of a PCF with Λ = 2.3μm, d/Λ = 0.8 at 633nm. The effective indexes of the x- and y-polarization of FSM are 1.40383994762110 and 1.40383980709472, respectively. The difference between this two polarization, $|n_{FSM}^{x} - n_{FSM}^{y}|$ = 1.4×10^{-7}, indicates that the two polarizations of FSM are degenerate.

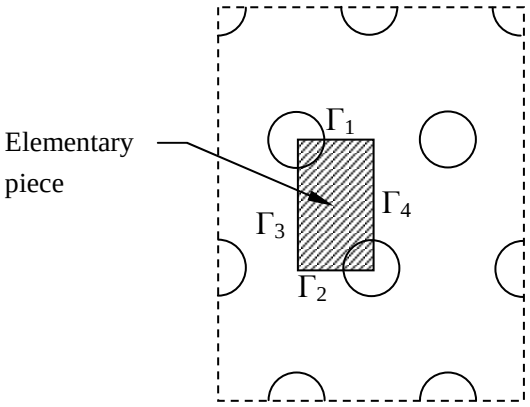

Figure 3.6 The elementary piece of the cladding used to calculate the fundamental space filling mode.

Table 3.3 Boundary conditions for calculating n_{SFM}

Polarization	Γ_1 and Γ_2	Γ_3 and Γ_4
x	PMC	PEC
y	PEC	PMC

3.3.3.3 Guided modes of PCF

To find the supported propagation modes of the PCF and validate the full-vector FEM of FEMLAB, the propagation constants of all propagating modes and that of the cladding should be determined first. Fig. 3.7 shows the effective index n_{eff} (= β/k) as a function of Λ/λ for a PCF with hole pitch Λ = 2.3μm and hole diameter d = 1.4μm.The effective index of cladding is also shown in the same figure. In the calculations the

background refractive index of silica is assumed to be a fixed value of 1.46 for the entire wavelength range. This PCF is multi-mode and has two multiplets. The first one is a polarization doublet (Fig. 3.8 a to b), while the second one consists of four nearly degenerate higher-order modes (Fig. 3.8 c to f). Therefore, the total number of guided mode is 6.

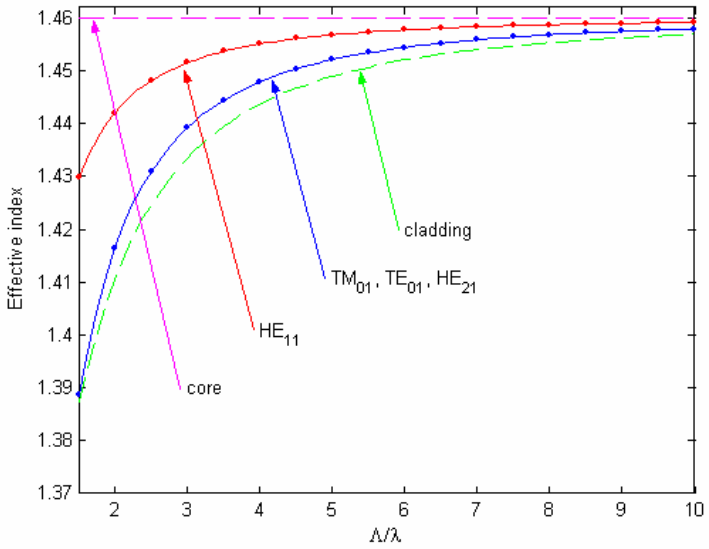

Figure 3.7 Modal dispersion properties of a multi-mode PCF with Λ = 2.3μm and d = 1.4μm.

All the results presented in this section are in good agreement with those obtained by a full-vector multipole method [21] and full-vector finite element method [22]. We thus convinced that FEMLAB is a reliable and accurate numerical tool for full-vector analysis of PCFs.

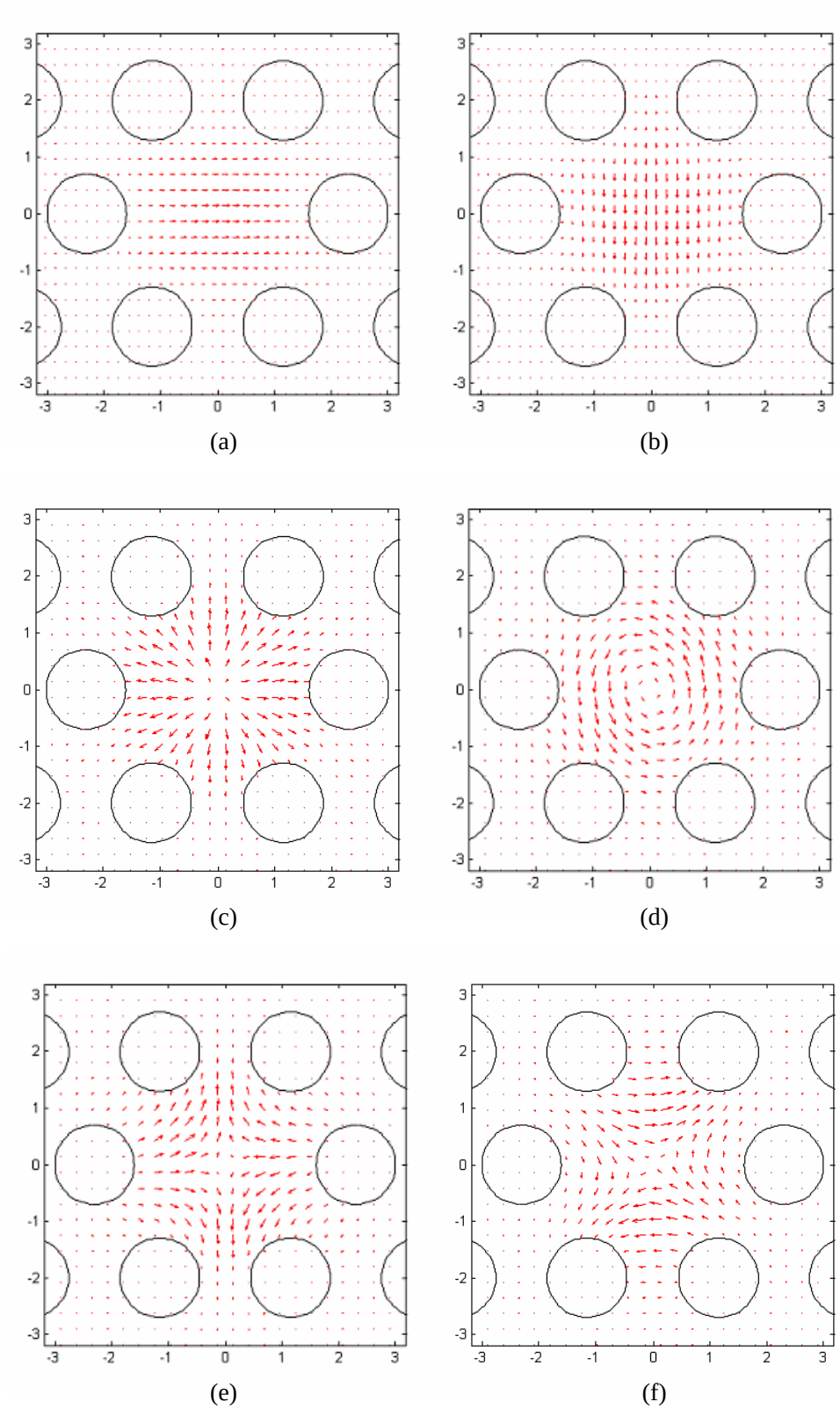

Figure 3.8 Vector transverse electric field distribution of (a) HE_{11}^{x} mode, (b) HE_{11}^{y} mode, (c) TE_{01} mode, (d) TM_{01} mode, (e) and (f) HE_{21} modes at λ = 632.8nm. Structural parameters: Λ = 2.3μm, d = 1.4μm.

3.4 Simple splice estimation between ESM PCF and SMF

The PCF/SMF splice loss has been studied by calculating the transmitted and reflected fields using a FDTD [23], and by evaluating the overlap integral of mode field distribution obtained from FEM [24]. However, for both techniques, numerical calculations are tedious and intense computation efforts are required. In this section, I present an empirical formula for estimating the MFD of ESM PCF. The formula is based on the extensive simulation results obtained by FEMLAB and is subsequently used to estimate the splice loss between PCF and SMF.

3.4.1 Mode field diameter

One of the most important properties of the PCF is the fact that it can be designed to be ESM, referring to the fact that no higher order modes are supported regardless of wavelength. As is well known, PCFs with a structural parameter of $d/\Lambda < 0.45$ are endlessly single mode.

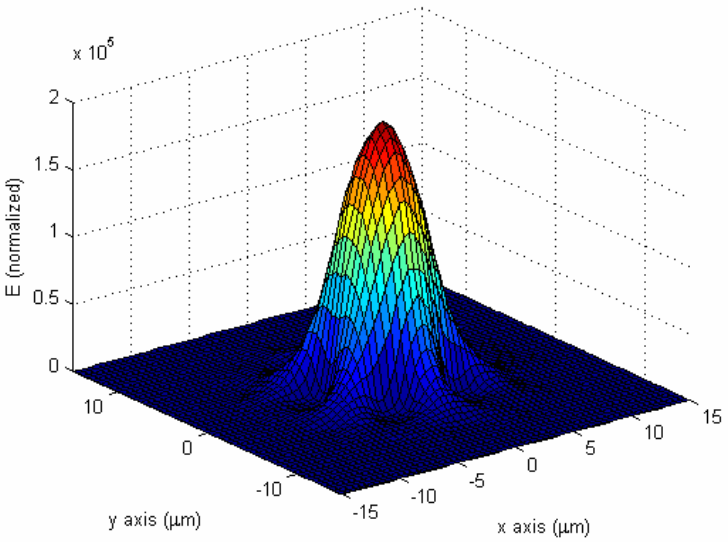

Figure 3.9 Electrical field distribution of a PCF with $d/\Lambda = 0.458$, $\Lambda = 6\mu m$ at $\lambda = 1550nm$.

To evaluate the MFD of PCF, the transverse electrical field components were

firstly calculated by using FEM (Fig. 3.9). The MFD was then obtained by numerical integration of electrical field components according to the definition of MFD as given in [25]

$$2\omega_{PCF} = 2\sqrt{\frac{2\int_0^\infty I(r)r^3 dr}{\int_0^\infty I(r)dr}} \tag{3.15}$$

where *I(r)* is the transverse modal intensity. Fig. 3.10 shows the calculated MFD ($2\omega_{PCF}$) as function of Λ for d/Λ from 0.25 – 0.45 at wavelength 1.55μm. The MFD increases approximately linearly with pitch Λ and decreases with an increase in d/Λ. The latter is expected because the light confinement is better for relative larger air-hole diameters. Based on the simulation results shown in Fig. 3.10, we apply a linear curve fitting for a specific value of d/Λ, which has the general form of

$$\omega_{PCF}\,|_{\frac{d}{\Lambda}=const} = a \cdot \Lambda + b \tag{3.16}$$

where *a* and *b* is the coefficient of linear curve fitting. The curve fitting results of the corresponding coefficients for different values of d/Λ are listed in Table 3.4.

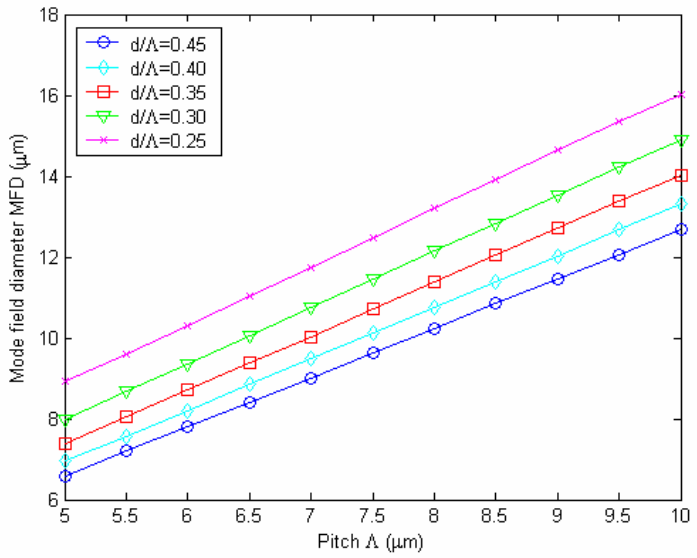

Figure 3.10 MFD ($2\omega_{PCF}$) as function of pitch for *d/Λ* from 0.25 to 0.45 in steps of 0.05.

Table 3.4 Curve fitting results of corresponding coefficients.

d/Λ	*a*	*b*
0.25	1.433	1.730
0.30	1.388	1.036
0.35	1.330	0.7292
0.40	1.272	0.5799
0.45	1.217	0.5008

Fig 3.11 shows the value of coefficients *a* and *b* as a function of d/Λ, where a second curve fitting (dotted line) is applied for the respective values of *a* and *b*, and coefficients of *a* and *b* can be further expressed in terms of d/Λ by the following equations

$$a = -0.549\left(\frac{d}{\Lambda}\right) + 0.8562$$
$$b = 0.01298\left(\frac{d}{\Lambda}\right)^{-3} + 0.07 \tag{3.17}$$

substituting Eq. (3.17) into Eq. (3.16), the mode field radius ω_{PCF} can be related to Λ and d/Λ by the following equation

$$\omega_{PCF}\left(\frac{d}{\Lambda}, \Lambda\right) = \left[-0.549\left(\frac{d}{\Lambda}\right) + 0.8562\right]\Lambda + \left[0.01298\left(\frac{d}{\Lambda}\right)^{-3} + 0.07\right] \tag{3.18}$$

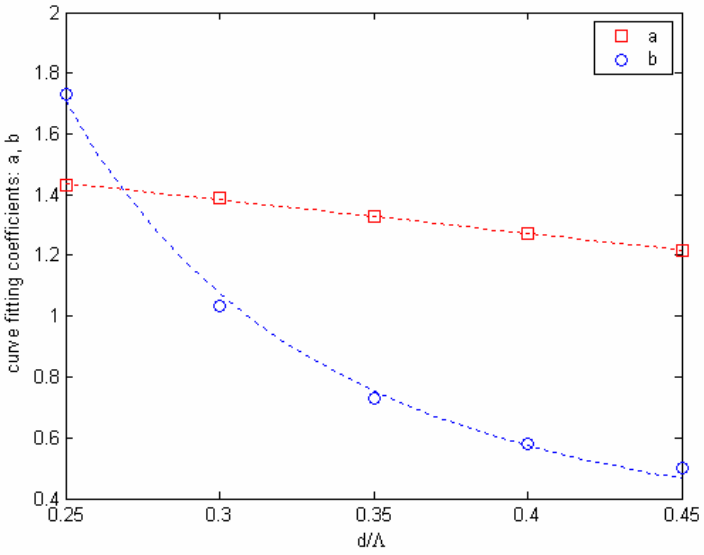

Figure 3.11 The value of coefficients (*a* and *b*) as a function of d/Λ.

The maximum deviation of ω_{PCF} between the above formula and the data shown in Fig. 3.10 is within 1% for 0.25≤d/Λ≤0.45. It should be mentioned that Eq. (3.18) can also be applied for other operating wavelengths by applying the scaling property of the Maxwell Equation [26]. In fact, Eq. (3.18) may be generalized to calculate the normalized mode field radius (ω_{PCF} / Λ) as function of d/Λ and normalized frequency λ/Λ by dividing both sides of Eq. (3.18) with Λ.

$$\frac{\omega_{PCF}}{\Lambda} = \left[-0.549\left(\frac{d}{\Lambda}\right) + 0.8562 \right] + \left[0.00837\left(\frac{d}{\Lambda}\right)^{-3} + 0.0452 \right]\left(\frac{\lambda}{\Lambda}\right) \qquad (3.19)$$

The deviation of above formula from the numerical results obtained by using FEM is less than 1% for $0.155 \le \lambda/\Lambda \le 0.31$ and $0.25 \le d/\Lambda \le 0.45$.

3.4.2 Splice loss evaluations

Once the MFD of PCF is obtained, the splice loss (α) between the PCF and the SMF can be estimated by [25]

$$\alpha = -20\log\left(\frac{2\omega_{PCF}\omega_{SM}}{\omega_{PCF}^2 + \omega_{SM}^2}\right) \cdot \exp\left(\frac{-2u^2}{\omega_{PCF}^2 + \omega_{SM}^2}\right) \qquad (3.20)$$

where *u* is a transverse offset, and $2\omega_{SM}$ is the MFD of the SMF that can be easily calculated if the *V*-number of the fiber is known. It should be mentioned that the MFD of PCF could also be evaluated in terms of *V*-number [27]. However, intensive computation is needed to calculate the *V*-number of the PCF because it involved the calculation of the effective index of the space-filling mode of the photonic crystal cladding.

Fig. 3.12 shows the estimated splice loss between the PCF and the Corning SMF-28 as functions of pitch Λ for d/Λ varying from 0.25 to 0.45 at a wavelength of

1.55μm. The calculation is based on Eq. (3.18) and Eq. (3.20) with offset set to zero. The upper value ($d/\Lambda = 0.45$) corresponds to the upper limit of the endlessly single mode operation of PCF. The results for smaller d/Λ are not included because the confinement loss would become significant for $d/\Lambda \leq 0.25$ even if the number of air-hole rings were reasonable large [28]. For comparison, the accurate splice loss computed by the overlap integral of the field distributions obtained from the vector FEM is also shown in Fig. 3.12. The maximum deviation is less than 0.2dB.

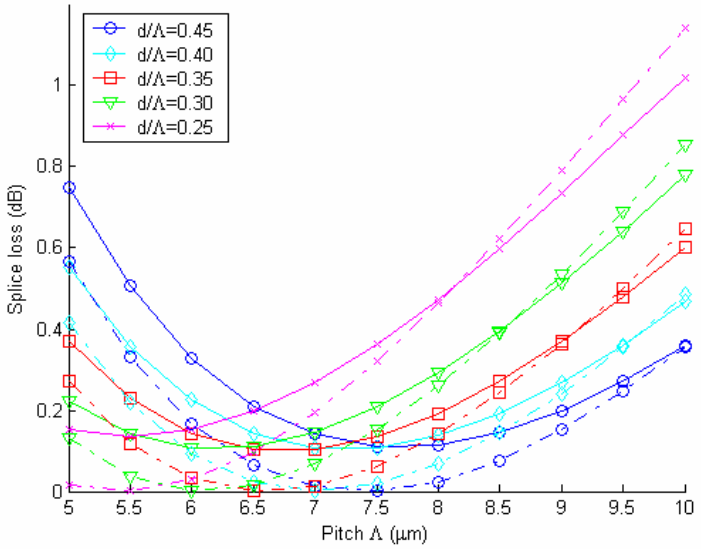

Figure 3.12 Splice loss as a function of pitch Λ for various d/Λ. Dash-dot line: results computed using Eq. 3.18 and Eq. 3.20; Solid line: Results obtained from overlap integral of vector field distributions

The results of overlap integral method indicate that zero coupling loss between PCF and single mode fiber is impossible and the minimum value is around 0.1dB. However, it is possible to achieve nearly zero coupling loss from the results of the Eq. 3.20, which can be attributed to the assumption of a Gaussian intensity profile for PCF. The corresponding value of MFD and pitch at the minimum coupling loss for different

d/Λ are summarized in Table 3.5. As the MFD is proportional to the core diameter (2Λ-d) of PCF, with the increase of d/Λ the pitch value should be increased to optimize the match of the MFD of the PCF and the SMF.

Table 3.5 MFD and pitch value at minimum coupling loss

d/Λ	Λ (μm)	MFD (μm)
0.25	5.6	9.85
0.30	6.3	9.81
0.35	6.8	9.78
0.40	7.3	9.84
0.45	7.7	9.80

Splice losses as function of offset were computed at both 1.31μm and 1.55μm for a particular LMA PCF (LMA10 from Crystal Fiber A/S Demark. d/Λ = 0.458, Λ = 6μm)/SMF-28 splice. The results are shown in Fig. 3.13. Comparison between the estimated splice loss and the more accurate overlap integral method based on FEM indicates that, at both operating wavelength, the splice loss deviations are less than 0.1dB and 0.25dB for zero and 3μm offsets respectively.

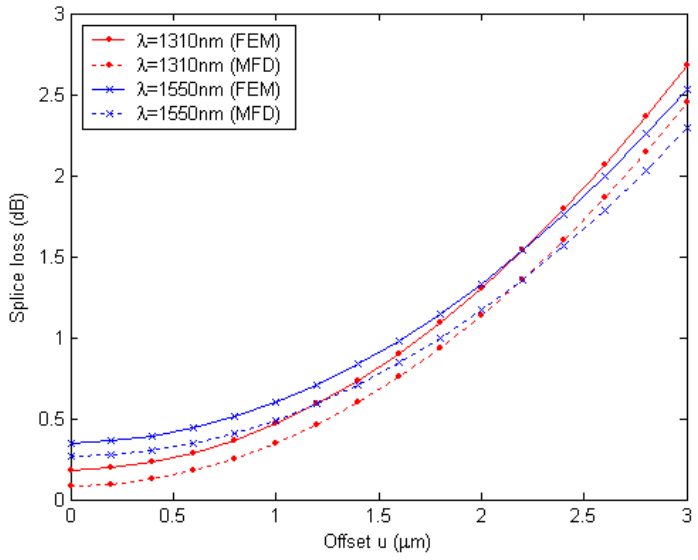

Figure 3.13 LMA10 PCF (d/Λ = 0.458, Λ = 6μm)/SMF-28 splice loss as

function of offset *u* for wavelength 1310nm and 1550nm.

The splice losses between SMF-28 fiber and two LMA PCFs (LMA10 and LMA5 with $d/\Lambda = 0.53$, $\Lambda = 3.125\mu m$) were experimentally measured at 1.55μm to be 0.47dB and 3.62dB, which agree well with the estimated values of 0.27dB and 3.2dB respectively.

3.5 Summary

In this chapter, we have reviewed a variety of numerical methods for modeling PCFs. The basic principles of FEM are introduced. The accuracy of a commercial software, FEMLAB, for analyzing PCFs was examined by comparing the simulation results with those obtained by supercell lattice method, multipole method and another FEM. At the end of this chapter, we calculate the vectorial field components and evaluate the MFD of ESM PCF. Based on the simulation results, an empirical formula is proposed for estimating the MFD. The results calculated by using the formula deviates less than 1% from those obtained from FEM for $0.25 \leq d/\Lambda \leq 0.45$. With the help of the MFD, the connection loss between a single mode fiber and a PCF can be evaluated by using the classical method based on the mode field radius.

References for Chapter 3

1. T. Birks, J. Knight, and P. Russell, “Endlessly single-mode photonic crystal fiber,” *Opt. Lett.*, vol. 22, pp. 961-963, 1997.

2. K.M. Ho, C.T. Chan, and C.M. Soukoulis, “Existence of a photonic gap in periodic dielectric structures,” *Phys. Rev. Lett.*, vol. 65, pp. 3152-3155, Dec 1990.
3. H.S. Sözüer, J.W. Haus, and R. Inguva, “Photonic bands: Convergence problems with the plane-wave method,” *Phys. Rev. B*, vol. 45, pp. 13962-13972, June 1992.
4. W. Zhi, R. Guobin, L. Shuqin, and J. Shuisheng, “Supercell lattice method for photonic crystal fibers,” *Opt. Express*, vol. 11, pp. 980-991, 2003.
5. R. Guobin, W. Zhi, L. Shuqin, L. Yan, and J. Shuisheng, “Full-vectorial analysis of complex refractive index photonic crystal fibers,” *Opt. Express*, vol. 12, pp. 1126-1135, 2004.
6. M. Qiu, “Analysis of guided modes in photonic crystal fibers using the finite-difference time-domain method,” *Microwave and Optical Technol. Lett.*, vol. 30, pp. 327-330, Sept 2001.
7. T. White, B. Kuhlmey, R. McPhedran, D. Maystre, G. Renversez, C. de Sterke, and L. Botten, “Multipole method for microstructured optical fibers. I. Formulation,” *J. Opt. Soc. Am. B*, vol. 19, pp. 2322-2330, 2002.
8. B. Kuhlmey, T. White, G. Renversez, D. Maystre, L. Botten, C. de Sterke, and R. McPhedran, “Multipole method for microstructured optical fibers. II. Implementation and results,” *J. Opt. Soc. Am. B*, vol. 19, pp. 2331-2340, 2002.
9. K.M. Lo, R.C. McPhedran, I.M. Bassett, G.W. Milton, “An electromagnetic theory of dielectric waveguides with multiple embedded cylinders,” *J. of Lightwave Technol.*, vol. 12, pp. 396-410, Mar 1994.
10. E. Centeno and D. Felbacq, “Rigorous vector diffraction of electromagnetic waves by bidimensional photonic crystals,” *J. Opt. Soc. Am. A*, vol. 17, pp. 320-327 2000.

11. B.M. Dillon, and J.P. Webb, “A comparison of formulations for the vector finite element analysis of waveguides,” *IEEE Trans. on Microwave Theory and Techniques*, vol. 42, pp. 308-316, Feb 1994.
12. S. Selleri and M. Zoboli, “Performance comparison of finite-element approaches for electromagnetic waveguides,” *J. Opt. Soc. Am. A*, vol. 14, pp. 1460-, 1997.
13. Jianming Jin, *The finite element method in electromagnetics* John Wiley & Sons, 2002.
14. M. Koshiba, *Optical waveguide theory by the finite element method*, KTK Scientific Publishers, 1992.
15. M. Koshiba, S. Maruyama, and K. Hirayama, “A vector finite element method with the high-order mixed-interpolation-type triangular elements for optical waveguiding problems,” *J. of Lightwave Technol.*, vol. 12, pp. 495-502, Mar 1994.
16. M.S. Stern, “Semivectorial polarized finite difference method for optical waveguides with arbitrary index profiles,” *IEE Proc.*, pt. J, vol. 135, pp. 56-63, Feb 1988.
17. R. Guobin, W. Zhi, L. Shuqin, and J. Shuisheng, “Mode classification and degeneracy in photonic crystal fibers,” *Opt. Express*, vol. 11, pp. 1310-1321, 2003.
18. M. Koshiba and K. Saitoh, “Finite-Element Analysis of Birefringence and Dispersion Properties in Actual and Idealized Holey-Fiber Structures ,” *Appl. Opt.*, vol. 42, pp. 6267-6275, 2003.
19. M. Koshiba, and K. Saitoh, “Numerical verification of degeneracy in hexagonal photonic crystal fibers,” *IEEE Photon. Technol. Lett.*, vol. 13, pp. 1313-1315, Dec 2001.

20. F. Brechet, J. Marcou, D. Pagnoux and P. Roy, “Complete Analysis of the Characteristics of Propagation into Photonic Crystal Fibers, by the Finite Element Method,” *Optical Fiber Technology*, vol. 6, pp. 181-191, April 2000.
21. A. Ferrando, E. Silvestre, J. Miret, P. Andrés, and M. Andrés, “Vector description of higher-order modes in photonic crystal fibers,” *J. Opt. Soc. Am. A*, vol. 17, pp. 1333-1340, 2000.
22. M. Koshiba, “Full-vector analysis of photonic crystal fibers using the finite element method,” *IEICE Trans. Electron.*, vol. E85-C, pp. 881-888, Apr 2002.
23. J.T. Lizier, and G.E. Town, “Splice losses in holey optical fibers,” *IEEE Photon Technol. Lett.*, vol. 13, pp. 794-796, 2001.
24. T. Conese, G. Barbarossa, and M.N. Armenise, “Accurate loss analysis of single-mode fiber/D-fiber splice by vectorial finite-element method,” *IEEE Photon. Technol Lett.*, vol. 7, pp. 523-525, 1995.
25. A. K. Ghatak and K. Thyagarajan, *Introduction to Fiber Optics*, Cambridge University Press, Cambridge, 1998.
26. W. Zhi, J. Jian, W. Jin, and K.S. Chiang, “Scaling property and multi-resonance of PCF-based long period gratings,” *Opt. Express*, vol. 12, pp. 6252-6257, Dec. 2004.
27. M. Nielsen, N. Mortensen, J. Folkenberg, and A. Bjarklev, “Mode-field radius of photonic crystal fibers expressed by the V parameter,” *Opt. Lett.*, vol. 28, pp. 2309-2311, 2003.
28. D. Ferrarini, L. Vincetti, M. Zoboli, A. Cucinotta, and S. Selleri, “Leakage properties of photonic crystal fibers,” *Opt. Express*, vol. 10, pp. 1314-1319, 2002.

CHAPTER 4

PROPERTIES OF A HIGHLY BIREFRINGENT PCF

In this chapter, we investigate various properties of a Hi-Bi PCF. The full-vector FEM is used to perform numerical simulations. The main properties of the fundamental mode, including modal birefringence, mode field diameter, divergence angle, and polarization mode dispersion as a function of wavelength and the structural parameters, were studied in detail.

4.1 Modal properties

This Hi-Bi PCF was originally demonstrated by Ortigosa-Blanch et al [1] and was the first reported Hi-Bi PCF ever. The scanning-electron micrograph (SEM) of the fiber is shown in Fig. 4.1a.

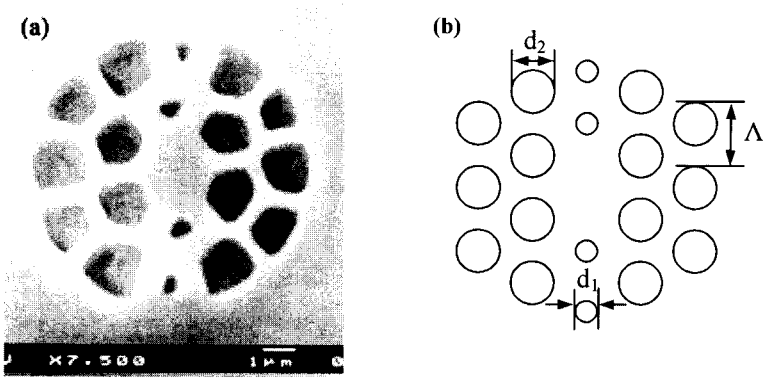

Figure 4.1 (a) SEM of the Hi-Bi PCF, (b) Idealized structure of the PCF.

It was fabricated by a stack-and-draw method [2]. Anisotropy was introduced by

positioning of capillaries with the same external diameter but different wall thickness, leading to different air-hole sizes in the cladding and two-fold rotational symmetry. The fiber has a pitch Λ = 1.96μm and a hole diameter of d_1 = 0.40μm and d_2 = 1.16μm for the small and large air-holes. The cross-section of the PCF is then modeled by an idealized structure with all the holes assumed to be circular and their sizes matched to that of the SEM of the fiber (Fig. 4.1b).

Our calculation confirms that two non-degenerate fundamental modes are well confined to the core region. By analogy to the conventional HB fibers, we call these two approximately linearly polarized modes as HE_{11}^{x} and HE_{11}^{y} mode, respectively. Fig. 4.2 shows the electric field vectors of the *x*- and *y*-polarized fundamental mode. The effective indexes corresponding to the two polarization modes are denoted as n_x and n_y, respectively. The modal birefringence $B = |n_x - n_y|$ of such a fiber as a function of wavelength is shown in Fig. 4.3 (the line with crosses). At wavelength 1540nm, the birefringence is 4×10^{-3}, corresponding to a beat length $L_B = \lambda/B$ = 0.385mm. This value is in good agreement with the measurement data (L_B = 0.42mm) reported in [1].

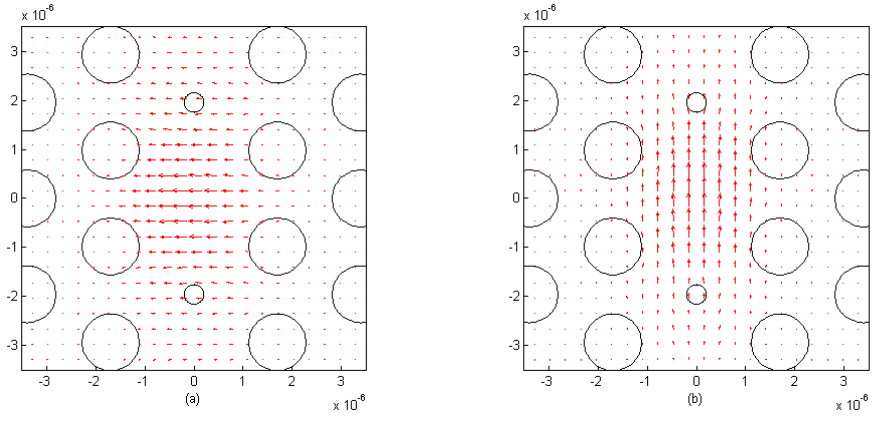

Figure 4.2 Electric field vectors of the (a) *x*- and (b) *y*-polarized fundamental mode.

It is possible to adjust the modal birefringence of the Hi-Bi PCF by the diameter of the air-holes. The influence of hole-size on the modal birefringence is thus important

from a practical design point of view. The computer simulation results of the modal birefringence for the PCFs with various hole-sizes are presented in Fig. 4.3. As expected, the birefringence increases with a decrease in the size of the small holes (d_1) (Fig. 4.3a) and an increase in the ratio of the size of the big holes over the pitch d_2/Λ (Fig. 4.3b). However, increasing birefringence through reducing the size of the small holes may not be practical because light confinement property of the fiber is affected when the hole-size becomes small, leading to high confinement loss. In our simulation we found a large portion of light field extends beyond the first small holes for d_1 = 0.2μm although a relative high birefringence can be obtained (the dotted line in Fig. 4.3a). It is therefore more practical to achieve a higher birefringence through the increase in d_2/Λ. However, an increase in the value of d_2/Λ would result in multi-mode operation at the working wavelength.

In order to understand the mode behavior of this Hi-Bi PCF, we have conducted extensive search on the possible modes that can be supported by the PCF. It should be noticed here that the fundamental space-filling mode can't be applied directly to predict the mode property because the cladding does not consist of an evenly distributed air-holes. In order to obtain birefringence as high as possible, d_1/Λ is chosen to be small enough, i.e. $d_1/\Lambda < 0.4$, which is smaller than the value required for ESM operation for a PCF with uniform hole size in the cladding. Therefore, we may intuitively regard that the higher order mode cutoff is mainly determined by the value of d_2/Λ. Fig. 4.4 shows the effective index of a Hi-Bi PCF with d_1 = 0.43μm, d_2 = 1.3μm, Λ = 1.8μm, and with 4 rings of air holes. It seems this Hi-Bi PCF is multi-mode for normalized frequency range from Λ/λ = 1.0 to 5.0. It is important to notice that the

mode confinement of higher order mode becomes so worse at normalized frequency lower than $\Lambda/\lambda = 1.0$ that it should be considered cutoff for a real PCF.

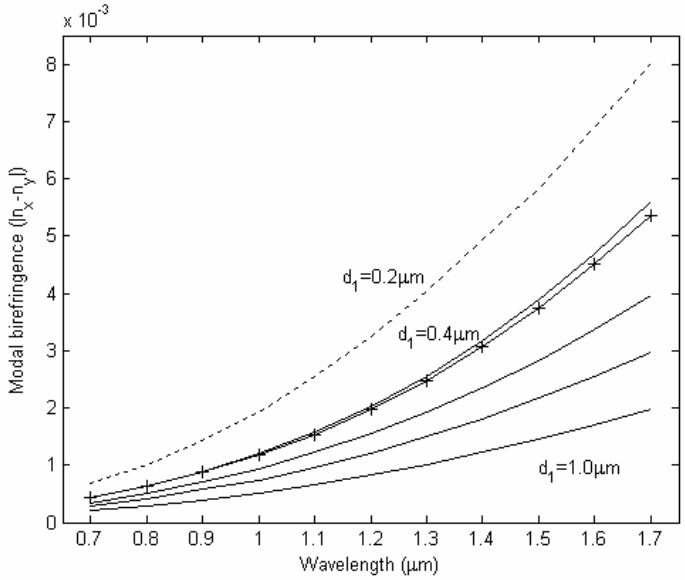

(a)

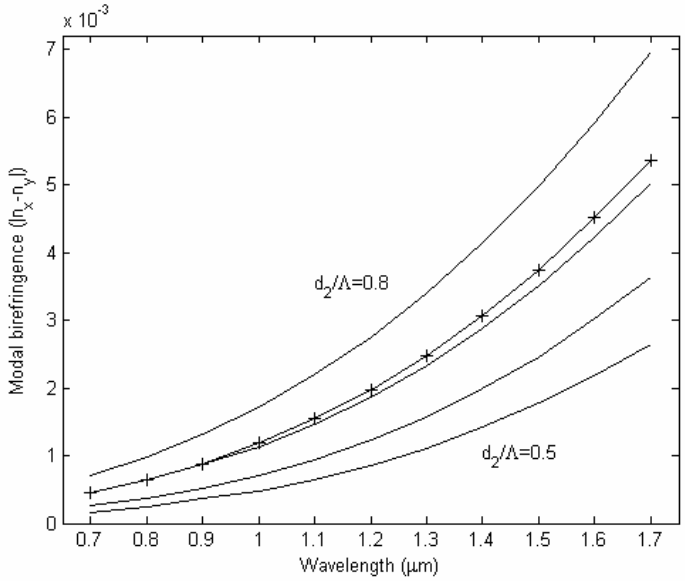

(b)

Figure 4.3 Dependence of modal birefringence on the size of the holes. (a) The size of the small holes are increased from d_1 = 0.2μm to 1.0μm in steps of 0.2μm with d_2/Λ = 0.6; (b) the size to pitch ratio for the big holes is increased from d_2/Λ = 0.5 to 0.8 in steps of 0.1 with d_1 = 0.4μm. (The lines with crosses in them

are the simulated results for the fiber presented in [1] with d_1 = 0.43μm, d_2 = 1.3μm and Λ = 1.8μm).

It has been shown that mode cutoff property of PCF can be studied from the corresponding effective mode area A_{eff} [3]. Further calculations of A_{eff} were conducted to investigate the second order mode cutoff of this Hi-Bi PCF, and the results are shown in Fig. 4.5. The cutoff wavelength for the second order mode is estimated to be 1.42μm.

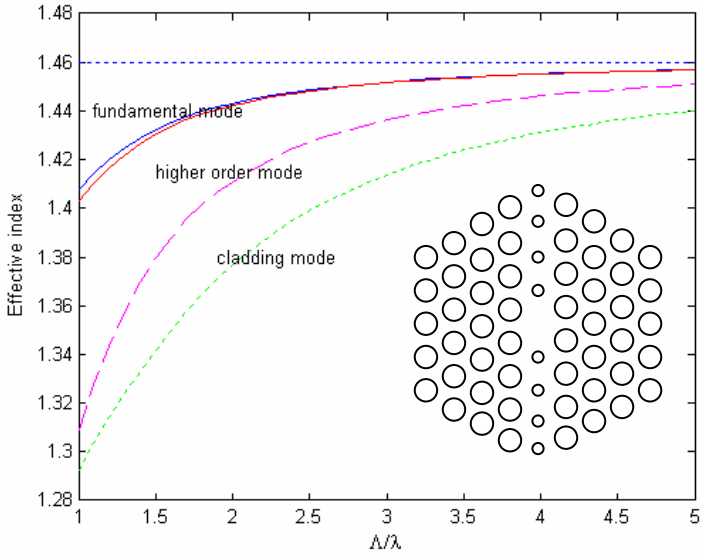

Figure 4.4 Modal dispersion properties of the Hi-Bi PCF with d_1 = 0.43μm, d_2 = 1.3μm, and Λ = 1.8μm.

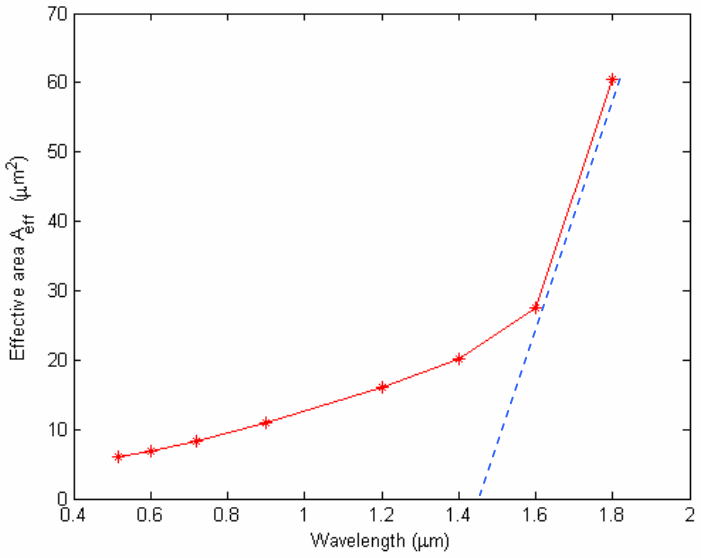

Figure 4.5 Effective area of the second order mode for the Hi-Bi PCF with $d_1 = 0.43\mu m$, $d_2 = 1.3\mu m$, and $\Lambda = 1.8\mu m$.

4.2 Mode field diameter

MFD w and half divergence angle θ are important parameters for the study fiber to fiber and fiber to waveguide joints, bending induced loss and non-linear fiber optics. For a Gaussian field, the MFD w is that at which power is reduced to $1/e^2$ of the maximum power and the corresponding half divergence angle θ can be expressed as $\theta \cong \tan^{-1} \lambda/\pi w$ [4]. Since the light intensity distribution of the highly birefringent PCF is not circularly symmetric, the MFD (w_x and w_y) and the half divergence angles (θ_x and θ_y) along the x and y directions are different. Numerical calculation shows that the intensity distributions along the two orthogonal directions can be approximated by proper Gaussian functions (Fig.4.6), and the root mean square error (RMSE) of the x- and y- direction intensity fitting is 0.012 and 0.065 for the y-polarized mode. Applying Gaussian fitting to the normalized intensity, the mode field widths and the half divergence angles can be calculated.

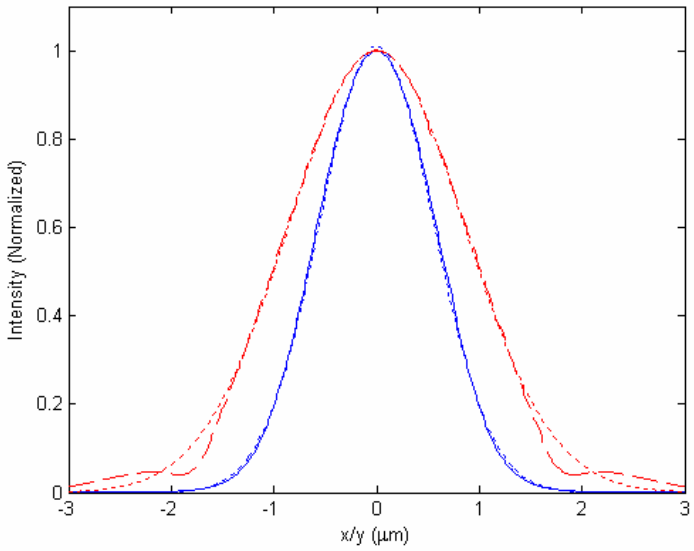

Figure 4.6 Normalized intensity of *y*-polarized fundamental mode (λ=1540nm, *x* direction: solid line, *y* direction: dashed line) and the corresponding Gaussian fit (dotted line).

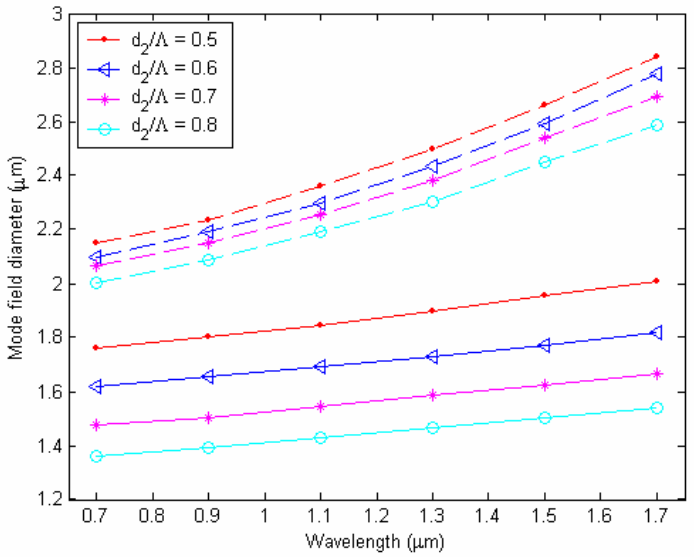

(a)

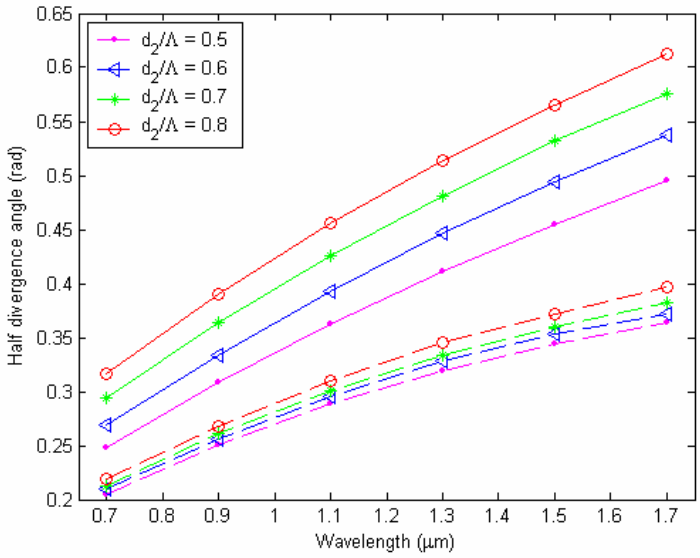

(b)

Figure 4.7 (a) The mode field diameter (w_x: the solid lines; w_y: the dashed lines) of the *y*-polarized mode. (b) The half divergence angles (θ_x: the solid lines; θ_y: the dashed lines) of the *y*-polarized mode.

Fig. 4.7 shows the MFD and the half divergence angles for the two directions of the *y*-polarized modes as functions of wavelength for various d_2/Λ ratios. As expected the mode becomes more confined for increased d_2/Λ ratio and hence displays a relatively smaller MFD. On the contrary, the half divergence angle increases as the d_2/Λ ratio is increased. The effects of varying d_2/Λ on the MFD along the *x*-direction are significantly bigger than that along the *y*-direction. This can be attributed to the associated changes in both the core size and effective index difference between the core and cladding along the *x*-direction.

The MFD and half divergence angle of the *x*-polarized mode are shown in Fig. 4.8.

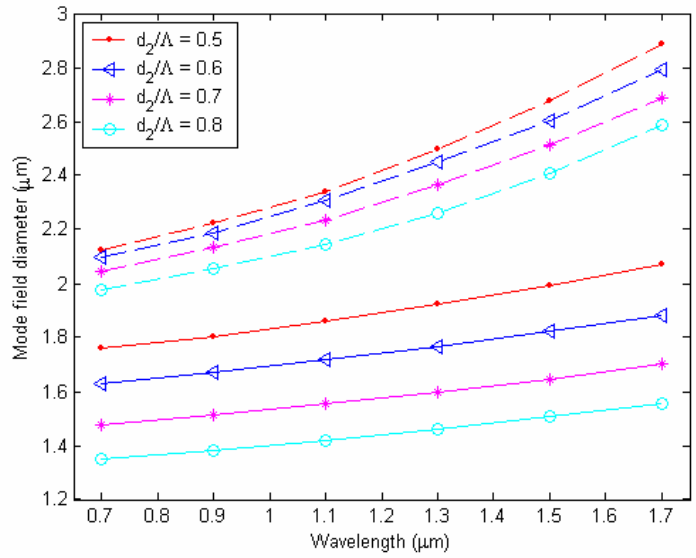

(a)

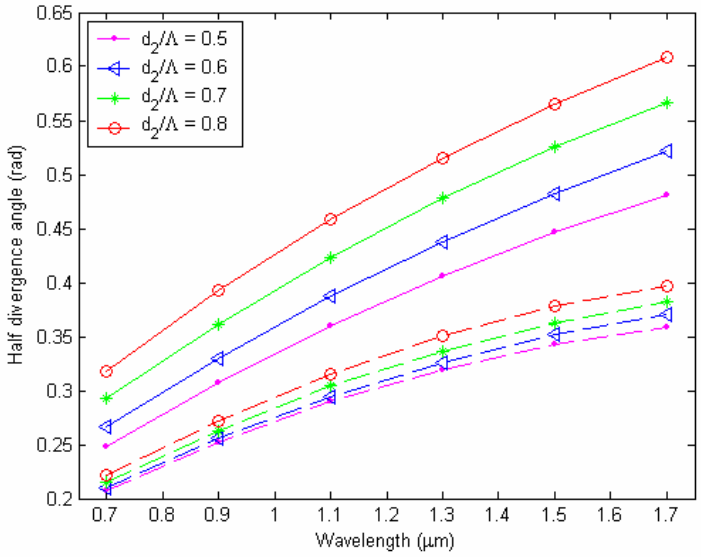

(b)

Figure 4.8 (a) The mode field diameter (w_x: the solid lines; w_y: the dashed lines) of the *x*-polarized mode. (b) The half divergence angles (θ_x: the solid lines; θ_y: the dashed lines) of the *x*-polarized mode.

4.3 Polarization mode dispersion

The non-degeneracy of the two polarizations verified by the computed values of effective indexes can lead to different group velocity. Different group velocities caused by the small departures from perfect hexagonal symmetry have been experimentally

observed [5]. The group velocity dispersion (GVD), which is an important parameter for high bit-rate transmission systems that uses polarization maintaining fibers [6], was theoretically calculated by the following equation

$$D = -\frac{\lambda}{c} \cdot \frac{\partial^2 n_{eff}}{\partial \lambda^2}$$

where n_{eff} is the effective index, λ is the optical wavelength, and c is the light speed in vacuum. The dependence of dispersion on d_2/Λ is shown in Fig. 4.9, where the increased separation between the two polarizations is an indication of stronger anisotropy introduced by a higher value of d_2/Λ.

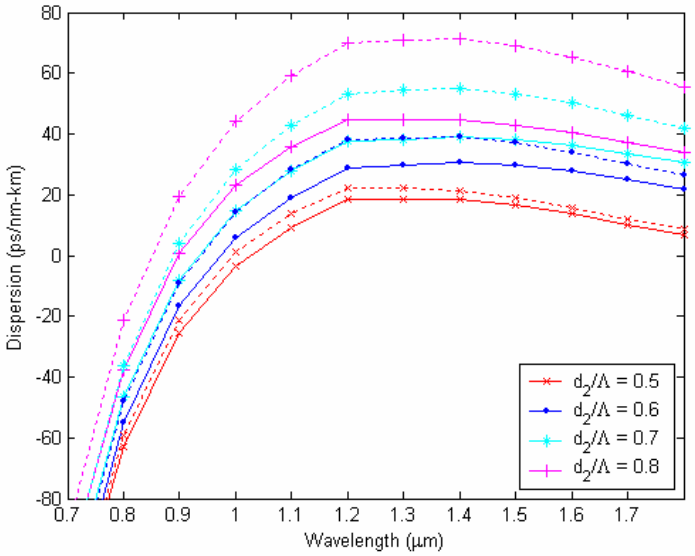

Figure 4.9 Calculated GVD for the two fundamental polarization modes of the fiber. (d_1 = 0.40μm, Λ= 1.80μm, x-polarized mode: solid line, y-polarized mode: dotted line).

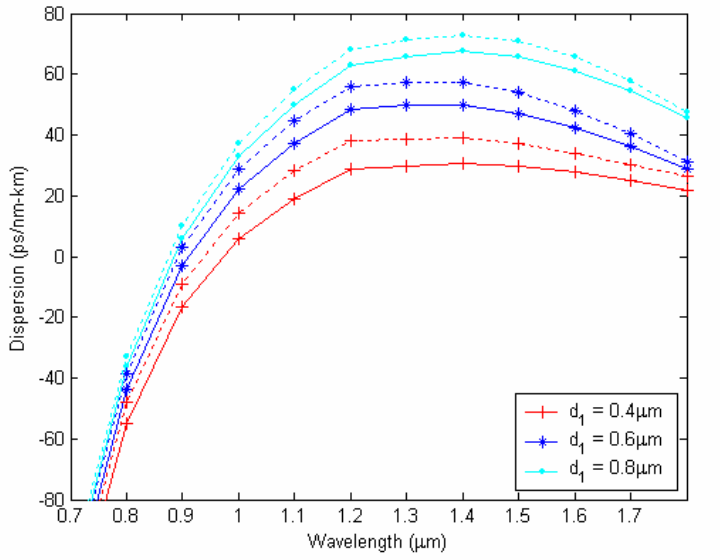

Figure 4.10 Calculated GVD for the two fundamental polarization modes of the fiber. (d_2/Λ= 0.6, Λ= 1.80μm, x-polarized mode: solid line, y-polarized mode: dotted line).

The dependence of dispersion on d_1 is shown in Fig. 4.10, where a slight separation between the two polarization modes is observed with the variation of d_1. A comparison between Fig. 4.9 and Fig. 4.10 indicates that dependence of the group velocity dispersion on d_2/Λ is stronger than on d_1.

4.4 Summary

A Hi-Bi PCF is successfully modeled and analyzed by using a full-vector FEM. The calculated birefringence is in good agreement with the measurements reported previously in the literature. The birefringence may be further enhanced by increasing the size to pitch ratio for the bigger holes. The mode field distribution has approximately an elliptical shape with the width of the major axis significant bigger than that of the minor axis. The dependence of MFD, divergence angle, and group velocity dispersion on the structural parameters of the PCF is also investigated.

References for Chapter 4

1. A. Ortigosa-Blanch, J.C. Knight, W.J. Wadsworth, J. Arriaga, B.J. Mangan, T.A. Birks, and P.St.J. Russell, “Highly biregringent photonic crystal fibers,” *Opt. Lett.*, vol. 25, pp. 1325-1327, Sept. 2000.
2. T.A. Birks, J.C. Knight, and P.St.J. Russell, “Endlessly single-mode photonic crystal fiber,” *Opt. Lett.*, vol. 22, pp. 961-963, July 1997.
3. N. Mortensen, "Effective area of photonic crystal fibers," Opt. Express, vol. 10, pp. 341-348, 2002.
4. N. A. Mortensen, J. R. Folken, Peter M. W. Skovgaard, and J. Broeng, “Numerical aperture of single-mode photonic crystal fibers,” *IEEE Photon. Technol. Lett.*, vol. 14, pp. 1094-1096, Aug. 2002.
5. J.C. Knight, J. Arriaga, T.A. Birks, A. Ortigosa-Blanch, W. J. wadsworth, and P. St. J. Russell, “Anomalous dispersion in photonic crystal fiber,” *IEEE Photon. Technol. Lett.*, vol. 12, pp. 807-809, July 2000.
6. K. Suzuki, H. Kubota, S. Kawanishi, M. Tanaka, and M. Fujita, “High-speed bi-directional polarization division multiplexed optical transmission in ultra low-loss (1.3dB/km) polarization-maintaining photonic crystal fiber,” *Electron. Lett.*, vol. 37, pp. 1399-1401, Nov. 2001.

CHAPTER 5

SINGLE POLARIZATION SINGLE MODE PCF

In this chapter, single-polarization single-mode (SPSM) operation of a Hi-Bi PCF is investigated in detail by using a full-vector finite element method with anisotropic perfectly matched layers (PMLs). We designed the cut-off wavelengths of the two linearly polarized principal eigen-modes of the SPSM PCF by varying the structure parameters of the fiber. The polarization dependent confinement loss and effective mode area are also evaluated to validate the design methodology. At the end of this chapter, splice losses to standard single-mode fiber (SMF) for particular SPSM PCFs are evaluated and appropriate structural parameters are recommended for operating at 1.30μm and 1.55μm.

5.1 Concept of SPSM PCF

Single-polarization single-mode fibers, in which only one linearly polarized mode is guided while the mode with orthogonal polarization is suppressed, are particularly desirable for use as in-line fiber polarizer and sensing elements. There has been considerable effort devoted to the design and fabrication of SPSM fibers based on various Hi-Bi fiber structures. Conventional schemes for accomplishing this include tunneling in W-profile fibers [1-2], utilizing differential bending loss of the orthogonal polarization modes [3], and attenuation induced by an absorptive cladding layer [4]. We have shown in previous chapters that the large index contrast and the stack-and-draw fabrication process permit high birefringence to be easily realized on

PCFs. Recently, it has been shown that Hi-Bi PCFs have the potential to realize better SPSM fibers [5-6]. In [5], a low-loss SPSM PCF with a confinement loss less than 0.1dB/km from 1.48 to 1.6μm was proposed and analyzed. A PCF-based single polarization fiber with a polarization dependent loss of 196dB/km and a transmission loss of 28dB/km at 1550nm was reported in [6].

Although some preliminary conclusions have been drawn in [6], the reported PCF is not optimized for particular applications such as fiber polarizing devices. For example, to make a fiber polarizer with an extinction ratio (ER) of 30dB at 1550nm, it requires ~150m of such a fiber. Also, no explicit design criteria have been reported for the design of SPSM PCF.

5.2 Design of SPSM PCF

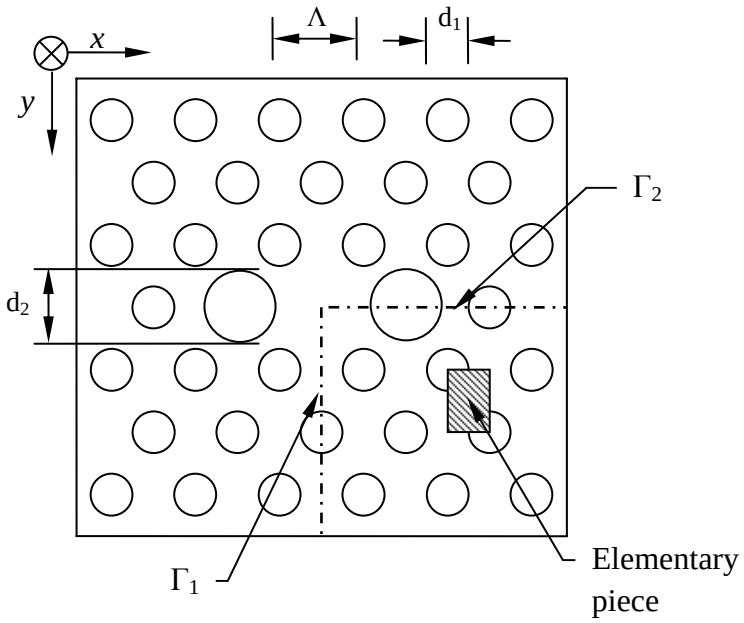

Figure 5.1 Schematic cross-section of a Hi-Bi PCF.

The structure of the Hi-Bi PCF to achieve single-polarization operation is shown in Fig. 5.1. This PCF is Hi-Bi because of different air hole diameters along the orthogonal axis

[7-8]. The objective of this section is to find the proper PCF parameters that support only a single linearly polarized mode. Although it has been suggested that the condition for single polarization is $d_2/d_1>2$ [6], we found that this is not always the condition to achieve single-polarization operation.

The full-vector FEM [9-10] is firstly applied to calculate the dispersion curve of the Hi-Bi PCF. Because of the symmetric nature of the PCF, only a quarter of the cross-section was used during the calculation and a perfect electric or perfect magnetic conductor (PEC or PMC) is applied along the symmetric plane Γ_1 and Γ_2. The definition of the boundary conditions and proper choice of them for calculating the corresponding guided modes have been described in detail in Chapter 3. The computational window is chosen beforehand so that the influence of artificial outer boundaries can be neglected. The background refractive index was obtained from the Sellmeier equation for silica [11].

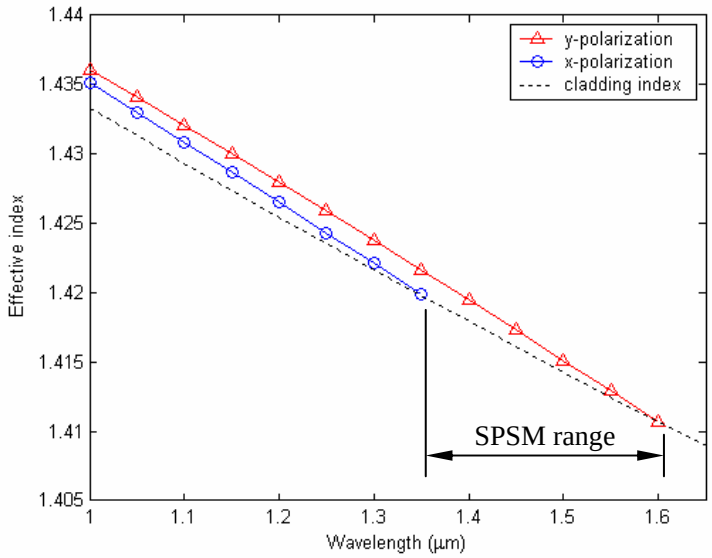

Figure 5.2 Dispersion curves as a function of wavelength for PCF with Λ=2.2μm, d_1/Λ=0.40, and d_2/Λ=0.95.

Fig. 5.2 shows the effective index of the *x*- and *y*-polarization mode as a function

of wavelength for a particular PCF with Λ=2.2μm, d_1/Λ=0.40, and d_2/Λ=0.95. Also shown in Fig. 5.2 is the effective cladding index of the fundamental space-filling mode (FSM) [12], which is evaluated by applying FEM to the elementary piece as shown in Fig. 5.1. Polarization cutoff occurs when the effective index of the polarization states falls below that of the FSM. The cutoff wavelengths of *x*- and *y*-polarized modes are estimated to be ~1.37μm and ~1.62μm, respectively, corresponding to the intersection points of their dispersion curves with that of the cladding as shown in Fig. 5.2. The single-polarization wavelength range where only *y*-polarized mode is guided and *x*-polarized mode is leaky is therefore estimated to be 250nm. Fig. 5.3 shows the intensity distribution of the *y*-polarized mode for the PCF at 1.55μm. The mode is well-confined and elongated in the *y*-direction.

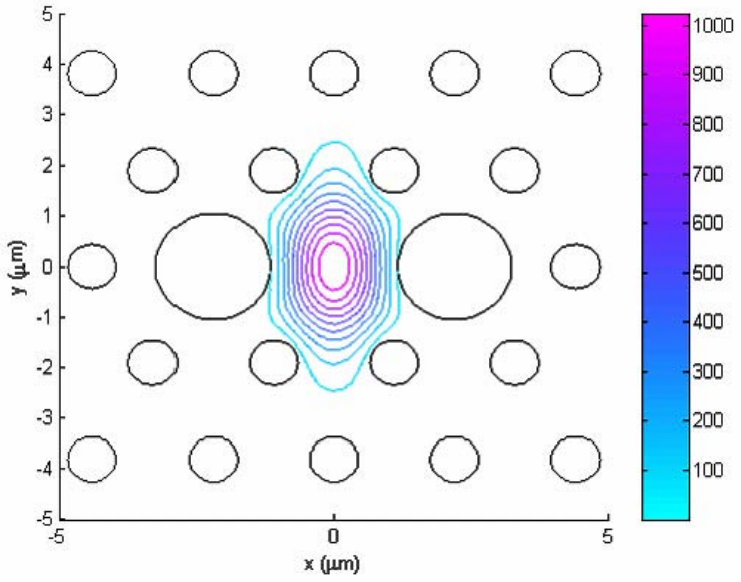

Figure 5.3 Contour plot of intensity distribution of the PCF with Λ=2.2μm, d_1/Λ=0.40, and d_2/Λ=0.95 at 1.55μm.

We found that it's possible to tune the wavelength range for single polarization operation by varying the fiber structural parameters: d_1/Λ, d_2/Λ, and Λ. Therefore, it's worthwhile to examine the dispersion properties under the influence of these

parameters. First, we fix d_1/Λ at 0.4 and Λ at 2μm and change d_2/Λ from 0.95 to 0.75 (Fig. 5.4). The cutoff wavelength for *x*- and *y*-polarization shifts from 1.26μm and 1.48μm to 1.78μm and 1.915μm, respectively. Tuning the cutoff wavelengths by changing the d_2/Λ ratio is possible but at the cost of the reduction of single-polarization wavelength range, from 220nm to 135nm for d_2/Λ=0.95 to 0.75. The single polarization wavelength range reduction can be attributed to the reduced birefringence induced by decreasing diameter of the two big air holes. When the dispersion curves of *x*- and *y*-polarization are intercepted by that of the cladding mode, a smaller single-polarization wavelength range appears for d_2/Λ=0.75. Therefore, the d_2/Λ should be set as high as possible to attain a wider single-polarization wavelength range. The d_2/Λ=0.95 is a reasonable parameter for practical PCFs [13], and is the value used for all the following simulations.

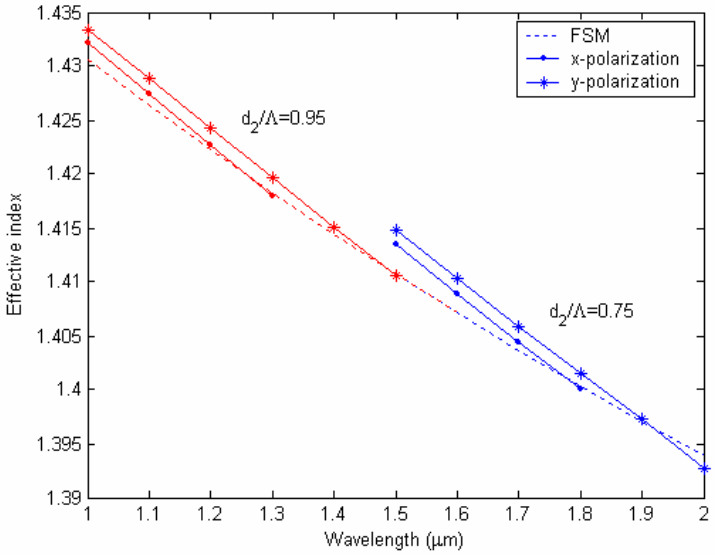

Figure 5.4 The dispersion curves for SPSM PCF with different pitches d_2/Λ. The ratio d_1/Λ and pitch Λ are fixed at 0.40 and 2μm.

The hole pitch Λ is then varied from 1.6μm to 2.4μm in steps of 0.4μm where d_1/Λ and d_2/Λ are fixed at 0.40 and 0.95, respectively. The dispersion curves are shown in

Fig. 5.5. The cutoff wavelength for *x*- and *y*-polarization shifts to longer wavelength with the increase of pitches, and the single-polarization wavelength range also increases slightly. It is also possible to tune the cutoff wavelength by varying the ratio d_1/Λ. However, the pitch Λ should be varied accordingly in order for the fiber to be a single polarization fiber over a useful wavelength range.

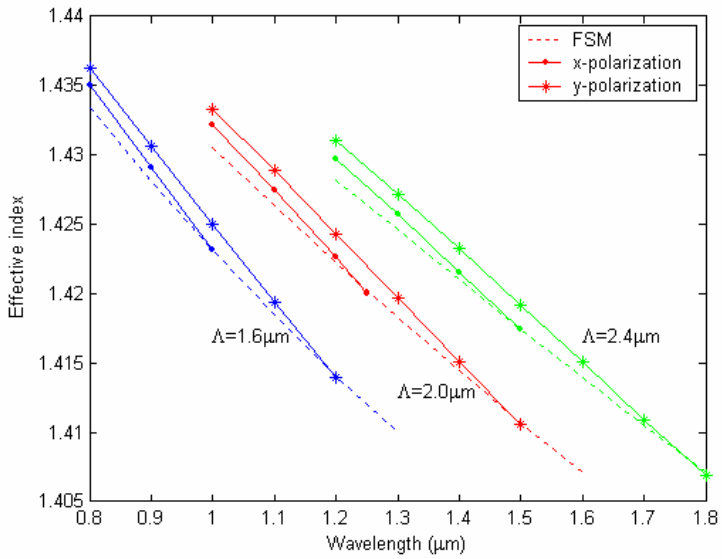

Figure 5.5 The dispersion curves for SPSM PCF with different pitches Λ. The ratio d_1/Λ and d_2/Λ are fixed at 0.40 and 0.95, respectively.

Fig. 5.6 shows dispersion curves for two set of parameters of d_1/Λ=0.5 and Λ=1.25μm, and d_1/Λ=0.4 and Λ=2μm. A smaller ratio of d_1/Λ requires a larger pitch Λ to support a single-polarization within a particular wavelength range. Further simulation shows that a PCF with a pitch as large as 8μm and d_1/Λ=0.30 has cutoff wavelengths of 1.12μm and 1.8μm for *x*- and *y*-polarization. If the pitch Λ were kept constant, further reduction of d_1/Λ to small values would lead to the dispersion curves of both polarizations become parallel to that of cladding, i.e., no crossing between the dispersion curves in the desired wavelength range. The fiber hence would not be a

single polarization fiber any more. In Fig. 5.6 the upper set of curves shows that the effective indices of the *x*- and *y*-polarization, and FSM are relatively close, as compared to that of the lower set of curves. Hence it is expected that the PCF corresponding to the upper set of curves is more leaky than the lower one because the light confinement is largely dependent on the relative refractive indices difference between the core and cladding modes. A bigger refractive index difference results in smaller percentage of power distributed in the cladding and hence the PCF experiences lesser attenuation.

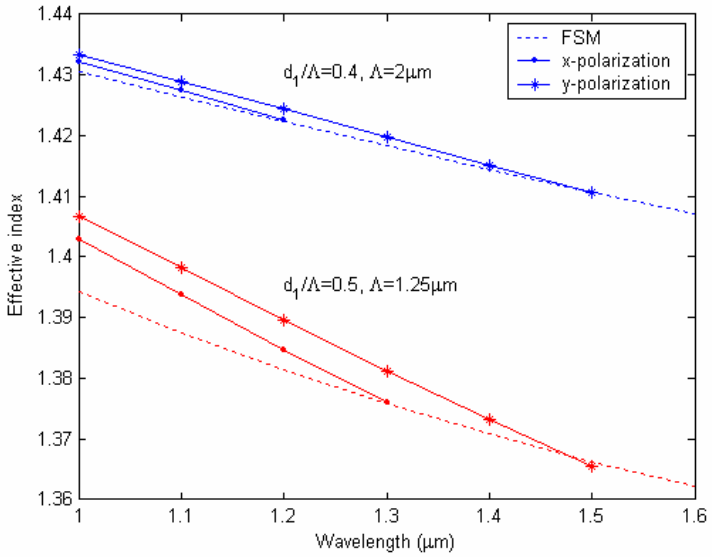

Figure 5.6 The dispersion curves for SPSM PCF with different ratio d_1/Λ and pitches Λ. The ratio d_2/Λ is fixed at 0.95.

In order to find suitable parameters of d_1/Λ and Λ for SPSM operation, a series of numerical simulations have been performed. The cutoff wavelength as a function of Λ for different d_1/Λ is shown in Fig. 5.7. For smaller values of d_1/Λ, larger values of Λ can be chosen to obtain a wider single-polarization range. The wider single-polarization wavelength range is easy to understand because the modal birefringence increases with a decrease of d_1/Λ resulting in a wider intersection section

between the dispersion curves of the guided modes and that of the cladding mode. As shown in Fig. 5.7d, a d_1/Λ of 0.5, corresponding to d_2/d_1 of less than 2, still supports a single-polarization operation although the single polarization range becomes narrower.

From Fig. 5.7, we note that the cutoff wavelength shows linear dependence on Λ, which is useful for SPSM PCF design. The fiber structural parameters for a desirable SPSM PCF operating at a special wavelength range can be easily obtained from Fig. 5.7.

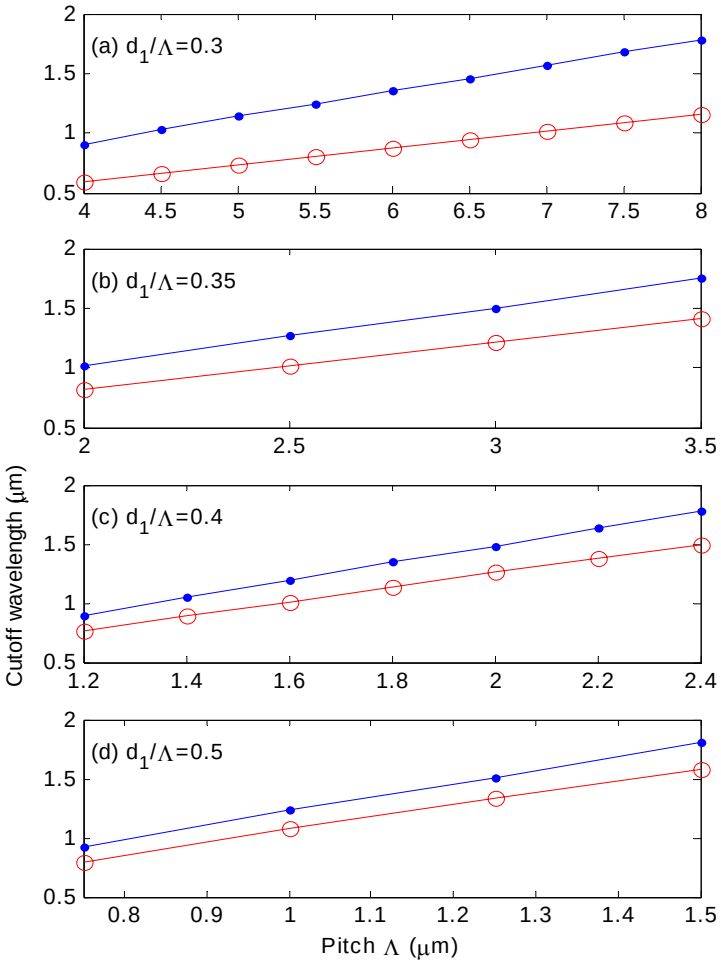

Figure 5.7 The cutoff wavelength as a function of pitch Λ for different ratios of d_1/Λ. Circle: *x*-polarization, dot: *y*-polarization.

5.3 Polarization dependent confinement loss and effective mode area

Because the cladding of PCF is usually made of finite numbers of rings of air holes, the guided modes in PCF are inherently leaky. Various numerical methods have been applied to investigate the leakage properties of PCF [14-15]. In this section, a full-vector FEM with anisotropic PMLs is used to calculate polarization dependent confinement loss. We will show that confinement loss simulation can provide valuable information for designing SPSM PCFs. It's worth mentioning here that the confinement loss exists even if other optical attenuations, i.e. Rayleigh scattering, imperfection loss, and absorption losses, are totally neglected. Thus, in order to realize a low-loss PCF, appropriate structural parameters should be chosen in order that the confinement loss is sufficiently small.

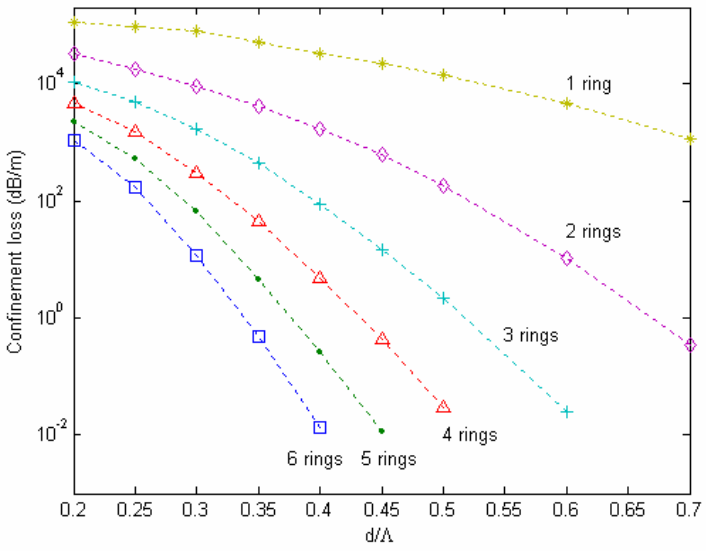

Figure 5.8 The confinement loss as a function of the number of hexagonally arranged air holes and d/Λ at 1.55μm. The air hole pitch is assumed to be 2.3μm.

First, our FEM program was tested rigorously by comparing with the multi-pole method [14] and other FEM data [5, 15] before it is used to perform confinement loss calculation. Fig. 5.8 shows the calculated confinement loss of a non-birefringent PCF (i.e., $d_1 = d_2 = d$) as a function of the number of rings of the hexagonally arranged air

holes and d/Λ ratio, where d is the diameter of air-hole and Λ is the hole spacing which is fixed at 2.3μm [14]. These results are calculated using our FEM program and agree well with the published results shown in Fig. 2.9 (Chapter 2). Therefore, we conclude that our program is reliable for confinement loss calculation.

We first study the PCFs aiming for single polarization operation around 1.30μm. The PCF parameters with cutoff wavelength of 1.30μm are listed in Table 5.1. These parameters were obtained by setting the cutoff wavelength of the *x*-polarization to 1.30μm and calculating the corresponding pitches using Fig. 5.7 for various d_1/Λ ratios.

Table 5.1

SPSM PCF Parameters and Confinement Loss @1300nm

	PCF I	PCF II	PCF III	PCF IV
d_1/Λ	0.30	0.35	0.40	0.50
Λ (μm)	9.03	3.22	2.07	1.21
Confinement Loss (dB/m)	*x*: 4.55 *y*: 0.11	*x*: 40.61 *y*: 0.33	*x*: 108.3 *y*: 0.56	*x*: 1692.1 *y*: 7.85
Bandwidth (nm)	14.6	84.7	65.3	41.7

Fig. 5.9 shows the calculated confinement losses for *x*- and *y*-polarization with 8 rings of air holes. The confinement losses for *x*- and *y*-polarized modes and SPSM bandwidth (BW) are also given in Table 5.1. The SPSM BW is defined as the wavelength range over which one polarization state is attenuated by at least 30dB/m while the orthogonal state suffers less than 1dB/m. PCF II shows the largest BW and PCF I is the smallest, which can be easily understood from Fig. 5.9. In Fig. 5.9 we see that low confinement losses can be obtained for both polarization modes at wavelengths far from the cutoff values (e.g. 1.0μm), whereas the confinement losses of

x-polarization shows an order of magnitude higher than that of *y*-polarization. PCF IV shows a sharp increase whereas PCF I reveals a gradual increase in confinement loss. The gradual increase can be attributed to the longer transition region between the cladding mode and the guided modes. Compared with other SPSM PCFs listed, PCF I allow the largest hole spacing Λ, resulting in a small splice loss with conventional optical fiber. However, the confinement loss difference between *x*- and *y*-polarization is the smallest for PCF I and the SPSM BW is only 14.6nm compared to 84.7nm of PCF II.

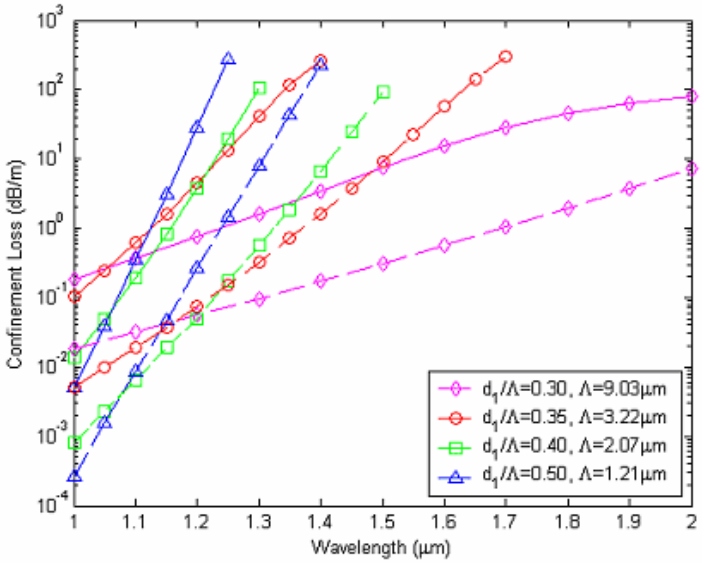

Figure 5.9 The confinement loss for the *x*- and *y*-polarization for SPSM PCF designed to work at 1.30μm. Solid lines: *x*-polarization; dashed lines: *y*-polarization.

Table 5.2

SPSM PCF Parameters and Confinement Loss @1550nm

	PCF V	PCF VI	PCF VII	PCF VIII
d_1/Λ	0.30	0.35	0.40	0.50
Λ (μm)	10.797	3.854	2.479	1.457
Confinement Loss (dB/m)	*x*: 1.5427 *y*: 0.0832	*x*: 32.286 *y*: 0.2665	*x*: 87.897 *y*: 0.4758	*x*: >1000 *y*: 5.1234
Bandwidth (nm)	12.4	103.5	72.9	45.6

Similar confinement loss profile can be found for SPSM PCFs designed to operate at 1.55μm (Table 5.2 and Fig. 5.10).

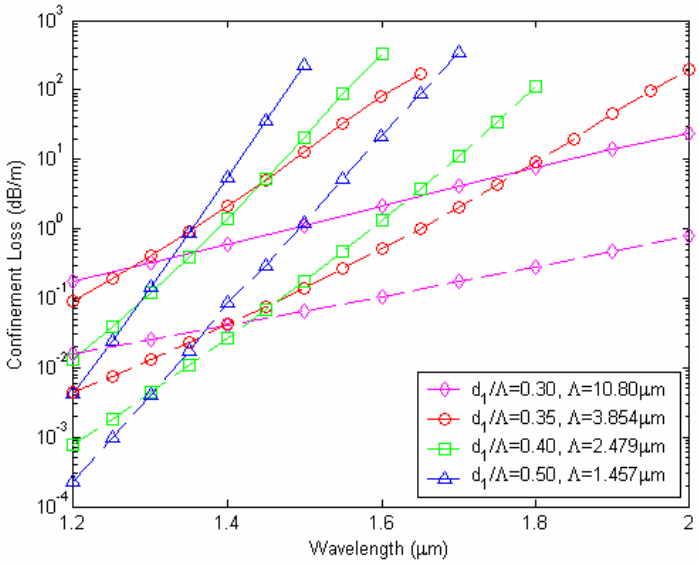

Figure 5.10 The confinement loss for the *x*- and *y*-polarization for SPSM PCF designed to work at 1.55μm. Solid lines: *x*-polarization; dashed lines: *y*-polarization.

It has been shown that the MFD of single-polarization optical fiber is a useful indicator of the fiber's performance [16] and mode cutoff of PCF can also be studied from the corresponding effective mode area A_{eff} [17]. The calculated A_{eff} of the SPSM PCF with d_1/Λ=0.40, Λ=2.07μm (PCF III) as a function of wavelength is plotted in

solid lines in Fig. 5.11. As has been shown in Fig. 5.7c, this fiber has a cutoff wavelength of ~1.3μm and ~1.50μm for the *x*- and *y*- polarization states. It can be seen from Fig. 5.11 that the A_{eff} remains nearly constant below the cutoff wavelength, but increases dramatically above the cut-off wavelength. The cut-off wavelength may be defined here by the crossing of the dotted lines as shown in Fig. 5.11 with the horizontal axis [17], which are ~1.35μm and ~1.55μm for the *x*- and *y*- polarized states. The discrepancy between the cut-off wavelengths obtained this way and that from Fig. 5.7 is less than 4%. From the practical point of view, the pitch Λ should be chosen to be a smaller value so that the cutoff wavelength shifts to shorter wavelength.

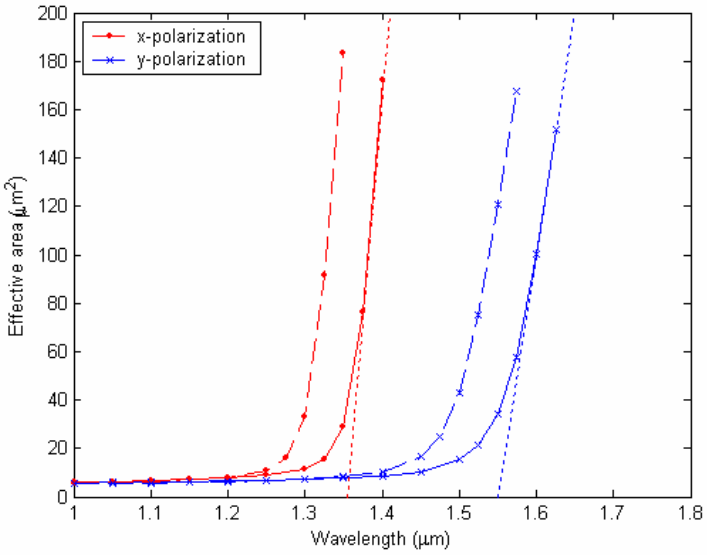

Figure 5.11 The calculated effective area of the two polarizations of a SPSM PCF with d_1/Λ=0.40, Λ=2.07μm (solid lines) and a modified PCF with d_1/Λ=0.40, Λ=1.98μm (dashed lines). The crossing of the dotted lines with the horizontal axis indicates the cutoff wavelength for the *x*- and *y*-polarizations.

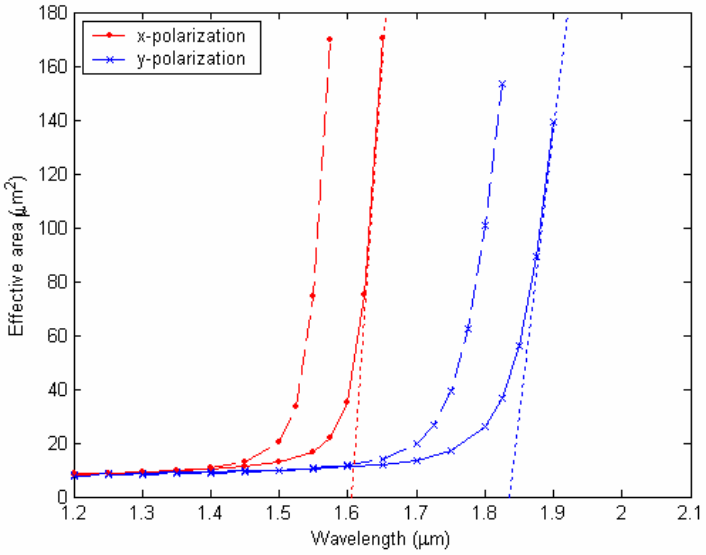

Figure 5.12 The calculated effective area of the two polarizations of a SPSM PCF with d_1/Λ=0.40, Λ=2.479μm (solid lines) and a modified PCF with d_1/Λ=0.40, Λ=2.35μm (dashed lines).

For comparison, we have also showed the A_{eff} of a modified SPSM PCF with d_1/Λ=0.40, Λ=1.98μm in dashed lines in Fig. 5.11. The A_{eff} of the SPSM PCFs operating at 1.55μm are shown in Fig. 5.12, where the solid lines and the dashed lines depict respectively the PCF with d_1/Λ=0.40, Λ=2.479μm (PCF VII) and a modified PCF with d_1/Λ=0.40, Λ=2.35μm.

5.4 Coupling between SMF and PCF

For practical applications of SPSM PCFs, splice loss between single-polarization fibers and conventional fibers or other optical waveguides should be considered. Using a full-vector FEM, we can accurately calculate the electrical field distribution of various waveguides, which can then be used for coupling loss evaluation by the overlap integral method. We have considered only the coupling loss between SPSM fibers and SMFs under ideal conditions where the two fiber axes are perfectly aligned, i.e.,

without longitudinal, lateral or angular misalignment.

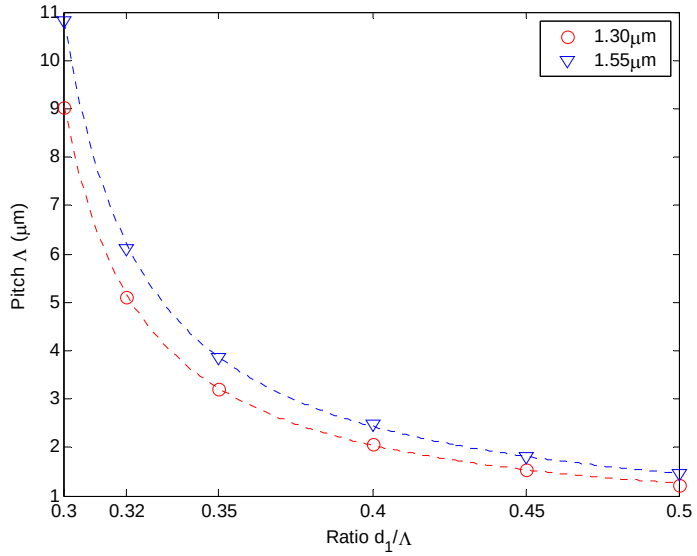

Figure 5.13 Pitch Λ as a function of the ratio d_1/Λ for SPSM PCF with *x*-polarization cutoff wavelength of 1.3μm and 1.55μm. The dotted lines are curve fitting results.

Before the splice loss calculation, the relationships between pitch Λ and the ratio d_1/Λ to achieve SPSM operation with *x*-polarization cutoff wavelength at 1.30μm and 1.55μm are plotted respectively in Fig. 5.13. The pitch associated with a specific ratio of d_1/Λ can be obtained from the curve fitting results (shown in dotted lines in Fig. 5.13).

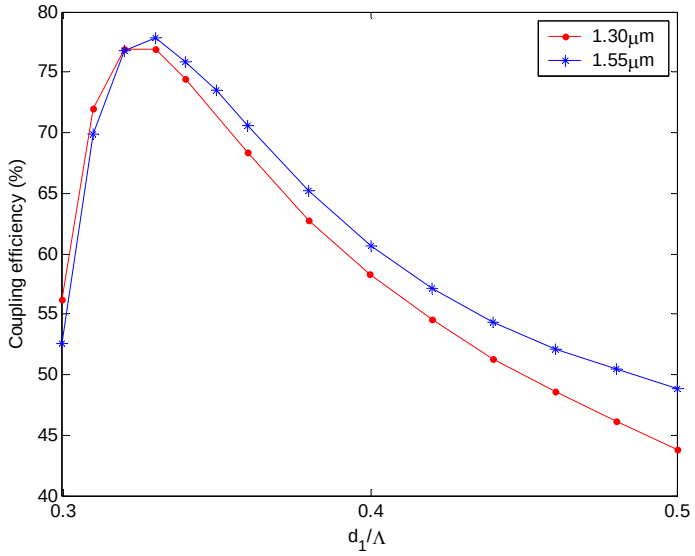

Figure 5.14 The coupling efficiency as a function of d_1/Λ for 1.30μm and 1.55μm.

The coupling efficiency between SPSM PCFs and SMF is calculated and shown in Fig. 5.14. In the simulations the MFD of SMF is approximated by normalized Gaussian modes and they are assumed to be 9.2μm at 1.30μm and 10.4μm at 1.55μm [18]. The mode field distribution of PCF is obtained by FEM and normalized before calculation. Overlap integration is then performed numerically to evaluate the coupling efficiency.

Fig. 5.14 shows the coupling efficiency as a function of d_1/Λ. The maximal coupling efficiency is estimated to be ~78% and ~77% for 1.55μm and 1.30μm, respectively, and the corresponding PCF structures are d_1/Λ=0.32, Λ=5.1754μm for 1.30μm and d_1/Λ=0.33, Λ=5.1646μm for 1.55μm. The polarization dependent confinement loss is 6.51dB/m for *x*-polarization and 0.179dB/m for *y*-polarization at 1.30μm and 6.78dB/m (*x*-polarization) and 0.144dB/m (*y*-polarization) at 1.55μm. Apparently, these loss data are not within the single polarization range as defined in Section 5.3, indicating that optimal coupling and optimal polarization extinction ratio may not be achieved simultaneously. We recommend the use of d_1/Λ=0.35 (PCF II and

VI as shown in Tabel 5.1 and 5.2) for SPSM PCF as being the optimum. The coupling efficiency would be over 70% for both 1.30μm and 1.55μm.

5.5 Summary

In conclusion, we have described the design methodology of PCF for SPSM operation at a particular operating wavelength. Specifically we optimized the PCF structure for operating at 1.30μm and 1.55μm. The bandwidths of the SPSM PCFs operation are respectively 84.7nm and 103.5nm for 1.30μm and 1.55μm. The cutoff wavelength is further validated by calculating the effective area of each polarization for two specific SPSM PCFs, which deviates less than 4% from that found by the confinement loss calculation using FEM. The coupling losses between the proposed SPSM fibers and single mode fibers were also calculated by using the overlap integral method and found to be better than 70% for 1.30μm and 1.55μm.

References for Chapter 5

1. J.R. Simpson et al., “A single-polarization fiber,” *J. Lightwave Technol.*, vol. LT-1, pp. 370-373, 1983.
2. R.H. Stolen, W. Pleibel, J.R. Simpson, et al., “Short *W*-tunneling fibre polarisers,” *Electron. Lett.*, vol. 24, pp. 524-525, 1988.
3. K. Okamoto, “Single-polarization operation in highly birefringent optical fibers,” *Appl. Opt.*, vol. 23, pp. 2638-2642, 1984.

4. K.S. Chiang, “Stress-induced birefringence fibers designed for single-polarization single-mode operation,” *J. Lightwave Technol.*, vol. 7, pp. 436-441, 1989.

5. K. Saitoh, and M. Koshiba, “Single-polarization single-mode photonic crystal fibers,” *IEEE Photon. Technol. Lett.*, vol. 15, pp. 1384-1386, Oct. 2003.

6. H. Kubota, S. Kawanishi, S. Koyanagi, M. Tanaka, and S. Yamaguchi, “Absolutely single polarization photonic crystal fiber,” *IEEE Photon. Technol. Lett.*, vol.16, pp. 182-184, Jan. 2004.

7. K. Suzuki, H. Kubota, S. Kawanishi, M. Tanaka, and M. Fujita, “High-speed bi-directional polarization division multiplexed optical transmission in ultra low-loss (1.3dB/km) polarization-maintaining photonic crystal fiber,” *Electron. Lett.*, vol. 37, pp. 1399-1401, Nov. 2001.

8. K. Suzuki, H. Kubota, S. Kawanishi, M. Tanaka, and M. Fujita, “Optical properties of a low-loss polarization-maintaining photonic crystal fiber,” *Opt. Express*, vol. 9, pp. 676-680, Dec. 2001.

9. J. Ju, W. Jin, and M.S. Demokan, “Properties of a highly birefringent photonic crystal fiber,” *IEEE Photon. Technol. Lett.*, vol. 15, pp. 1375-1377, Oct. 2001.

10. M. Koshiba, and K. Saitoh, “Finite-element analysis of birefringence and dispersion properties in actual and idealized holey-fiber structures,” *Appl. Opt.*, vol. 42, pp. 6267-6275, Nov. 2003.

11. A. Ortigosa-Blance, A. Diez, M. Delgado-Pinar, J. L. Cruz, and M. V. Andres, “Ultrahigh birefringent nonlinear microstructured fiber,” *IEEE Photon. Technol. Lett.*, vol. 7, pp. 1667-1669, July 2004.

12. T.A. Birks, J.C. Knight, and P.St.J. Russell, “Endlessly single-mode photonic

crystal fiber," *Opt. Lett.*, vol. 22, pp. 961-963, July 1997.

13. G. Kakarantzas, A. Ortigosa-Blanch, T. A. Birks, P. St. J. Russell, L. Farr, F. Couny, and B. J. Mangan, "Structural rocking filters in highly birefringent photonic crystal fiber," *Opt. Lett.*, vol. 28, pp. 158-160, Feb. 2003.
14. T. P. White, R. C. McPhedran, C. M. de Sterke, L. C. Botten, M. J. Steel, "Confinement losses in microstructured optical fibers," *Opt. Lett.*, vol. 26, pp. 1660-1662, Nov. 2001.
15. D. Ferranrini, L. Vincetti, M. Zoboli, A. Cucinotta, S. Selleri, "Leakage properties of photonic crystal fibers," *Opt. Express*, vol. 10, pp. 1314- 1319, Nov. 2002.
16. M. J. Messerly, J. R. Onstott, and R. C. Mikkelson, "A broad-band single polarization optical fiber," *J. Lightwave Technol.*, vol. 9, pp. 817-820, July 1991.
17. N. A. Mortensen, "Effective area of photonic crystal fibers," *Opt. Express*, vol. 10, pp. 341-348, Apr. 2002.
18. *SMF-28e Fiber Production Information Sheet*, Corning Incorporated, Corning, NY, 2003.

CHAPTER 6

TWO-MODE PHOTONIC CRYSTAL FIBER THEORY

In this chapter, we discuss the two-mode operation of the index-guiding PCF and explore the possible structures to support only the fundamental mode and the second order mode over an extended wavelength range. This ultra-broadband operation wavelength range will greatly enhance the performance of the two-mode fiber devices. Then we discuss the mode properties of a two-mode Hi-Bi PCF with different diameters of air-hole along the orthogonal axis. At the end of this chapter, we theoretically investigate a commercially available Hi-Bi PCF with similar structure, which will be used for sensing experiments in the next chapter.

6.1 Modal properties of two-mode PCF

We have shown in previous chapters that one of the earliest known and most exciting properties of PCF is the remarkable endlessly single mode property, where it supports only the two degenerate fundamental modes within the transparent window of silica. There exists a clear boundary between single- and dual-mode regions that have been determined by different methods [1-3]. However, the operation of PCF in two-mode regime was not particularly addressed. Conventional circular and elliptical core step-index two-mode optical fiber have been investigated for a number of device applications such as intermodal couplers [4], selective modal filters [5], acousto-optic frequency shifters [6], dispersion compensators [7], optical switches [8], and strain and

temperature sensors [9-10]. However, the wavelength range of the two-mode operation for conventional fibers is typically less than 150nm [11], which limits the potential applications of the two-mode devices. We will investigate the possibility of achieving broader two-mode wavelength range by using PCFs in this section.

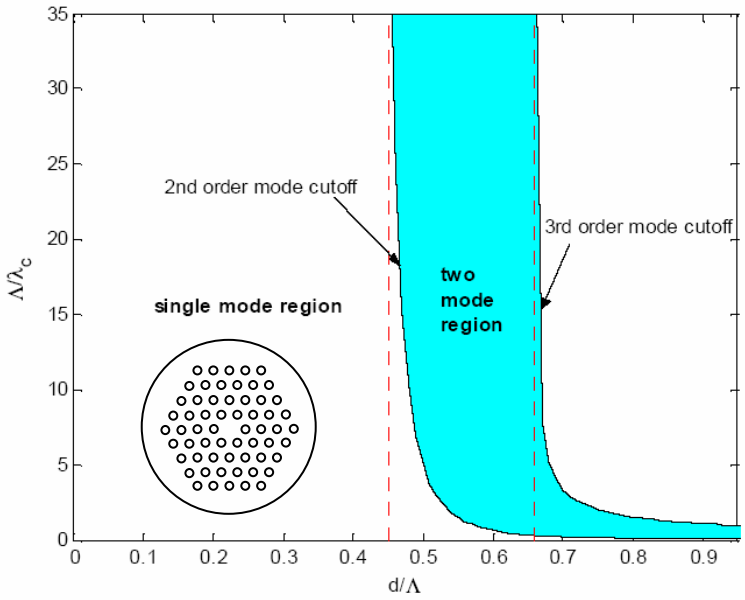

Figure 6.1 Normalized cutoff wavelength of the fundamental mode and that of the second order mode as a function of d/Λ.

We consider the PCF structure as previously shown in Fig. 3.3, which is reproduced in the inset of Fig. 6.1. We calculated the cut-off frequencies of the guided modes by finding the cross-points between their dispersion curves and that of the fundamental space filling mode of the cladding. Fig. 6.1 shows the normalized cut off frequency of the second order mode and third order modes as functions of the d/Λ. Again it confirms that d/Λ ≈ 0.45 bounds the endlessly single-mode region. The two-mode region shown in Fig. 6.1 corresponds approximately to a d/Λ value from 0.45 to 0.65 [12]. Within this region there exist a total number of 6 guided modes, include two degenerate fundamental mode and four nearly degenerate second order mode. The electric fields of these modes resemble those we showed in Fig. 3.8

(Chapter 3). Take $d/\Lambda = 0.55$ as an example, the cut-off wavelength of the second order mode is 1.9μm and 3.3μm for Λ = 3μm and 5μm, which is beyond the transparent window of silica material and hence the PCFs may be regarded as “endlessly two-mode”.

6.2 Highly birefringent two-mode PCF

Similar to the dual-mode circular-core fiber [4-5, 13-14], the two-mode PCF introduced in previous section suffers the instability in the lobe orientation of the second-order mode. However, it is possible to stabilize the lobe orientation by intentionally introducing a birefringence, as elliptical optical fiber does. Since the modes in an elliptical-core fiber are no longer degenerate, instability of the second-order mode lobe orientation can be eliminated by choosing a proper operating wavelength [11, 15]. Normally the two-mode operating wavelength range is limited around 150nm for the elliptical-core fiber [11].

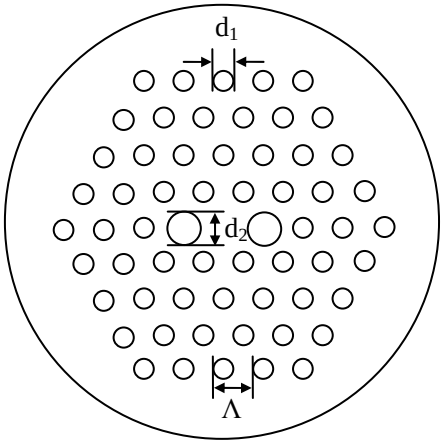

Figure 6.2 Schematic cross section of a highly birefringent PCF.

We have shown in Chapter 3 that the PCF can be desirably made highly birefringent by breaking its two-fold symmetry. One of the promising Hi-Bi PCF

structures [16-17] is shown in Fig. 6.2, which has been shown a very low transmission loss. This Hi-Bi PCF is characterized by three parameters: the pitch of the air-holes Λ, the diameters of the small diameters d_1, and the diameters of the large hole diameter d_2. It's possible to introduce a high birefringence to this PCF while retaining a wide two-mode operation range. For example, a Hi-Bi PCF with $d_1/\Lambda = 0.54$, $d_2/\Lambda = 0.98$, and $\Lambda = 6.0\mu m$ shows a two-mode range covering all the low-loss window of silica from 0.4μm to 1.8μm (Fig 6.3).

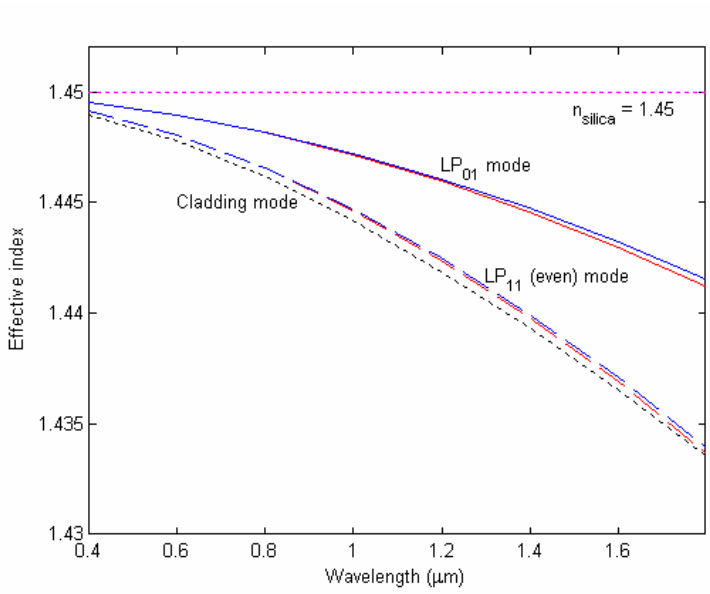

Figure 6.3 Modal dispersion curve of a Hi-Bi PCF with $d_1/\Lambda = 0.54$, $d_2/\Lambda = 0.98$. Solid lines represent the non-degenerate LP_{01} modes and dash lines represent the LP_{11} (even) modes.

There're totally 4 non-degenerate linearly-polarized modes supported by this Hi-Bi PCF with their effective indices lies above that of the cladding. The corresponding vector transverse mode field patterns are shown in Fig 6.4. By analogy to the elliptical core fiber, these four modes are labeled as LP_{01}^{x}, LP_{01}^{y}, LP_{11}^{x} (even) and LP_{11}^{y} (even) mode. The superscripts *x* and *y* correspond to the *x*- and *y*-polarization modes. It's interesting to notice that this Hi-Bi PCF is capable to suppress the LP_{11}(odd)

modes, which mainly limit the two-mode wavelength range of the elliptical core fiber [11].

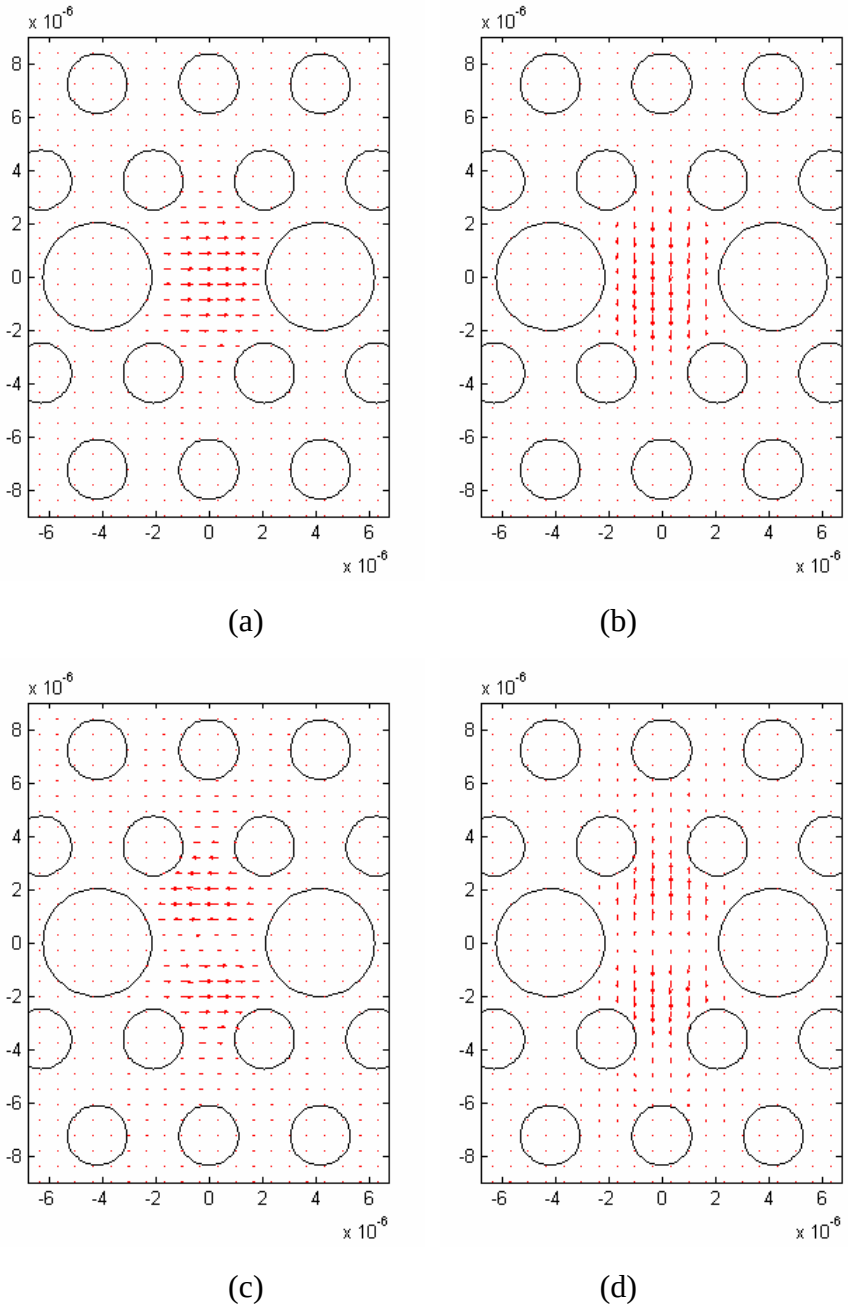

Figure 6.4 Transverse electric field distribution of (a) LP_{01}^{x}, (b) LP_{01}^{y}, (c) LP_{11}^{x} (even), and (d) LP_{11}^{y} (even) modes at 1.3μm.

The confinement loss of the LP_{11}(even) and LP_{11}(odd) mode of this two-mode Hi-Bi PCF with 10 rings of air holes is shown in Fig. 6.5. As shown in Fig. 6.5, the confinement loss of LP_{11}(even) mode is less than 0.025dB/m at 1.8μm, but it is larger

than 17dB/m for LP_{11}(odd) mode at 0.8μm even with 10 rings of air-holes. For wavelength longer than 0.8μm the confinement loss is much larger than the value at 0.8μm and is not shown in Fig. 6.5. Therefore, we're confident the confinement loss of LP_{11}(odd) is so large that it should not be considered guided by this two-mode PCF.

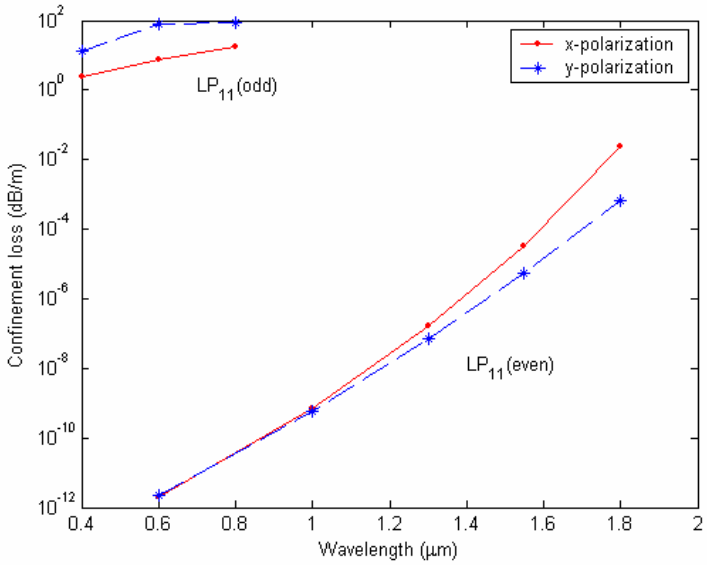

Figure 6.5 Confinement loss of LP_{11}(even) and LP_{11}(odd) mode of the two-mode Hi-Bi PCF with 10 rings of air-holes. (d_1/Λ = 0.54, d_2/Λ = 0.98, and Λ = 6.0μm).

6.3 A commercially available two-mode Hi-Bi PCF

For a commercially available Hi-Bi PCF with d_1/Λ = 0.536, d_2/Λ = 0.974, and Λ = 4.179μm (Fig. 6.6), which is designed for highly birefringent single-mode operation at 1550nm, its two-mode operation wavelength range extends to over 650nm [18]. Fig. 6.7 shows the dispersion curve of the first four guided modes and that of the fundamental space-filling mode. As shown in Fig. 6.7, the Hi-Bi PCF supports only four non-degenerate eigenmodes with transverse mode field pattern similar to those

shown in Fig. 6.4. It is worthy noting that there does not exist the LP_{11} (odd) mode at shorter wavelengths, which is remarkable different from that of the conventional elliptical core fiber. The cutoff wavelengths of LP_{11}^{x} (even) and LP_{11}^{y} (even) modes are estimated to be ~1.32μm and ~1.48μm, respectively, corresponding to the intersecting points of their dispersion curves with that of the cladding dispersion as shown in Fig. 6.7.

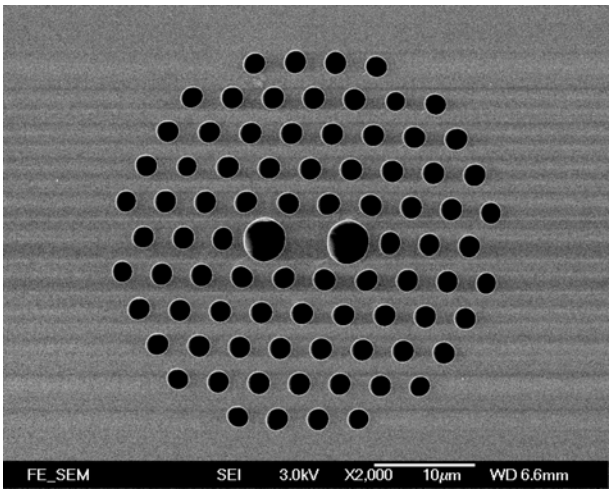

Figure 6.6 SEM photo of a Hi-Bi PCF with d_1/Λ = 0.536, d_2/Λ = 0.974, and Λ = 4.179μm.

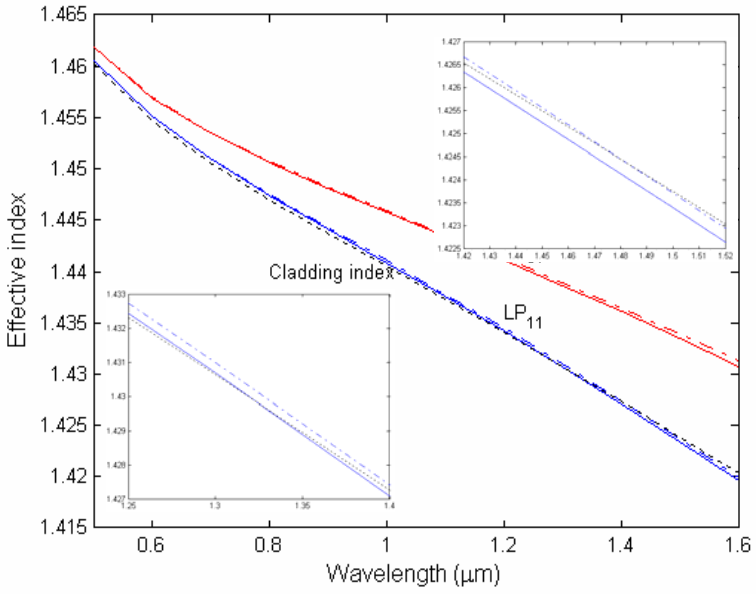

Figure 6.7 Dispersion curve of the first two guided modes (dash-dot line:

x-polarization, solid line: *y*-polarization) and cladding space-filling mode (dotted line). The background refractive index of silica is obtained from Sellmeier equation [19].

The confinement loss of LP_{11}(even) and LP_{11}(odd) mode of this commercially available Hi-Bi PCF with 6 rings of air-holes is shown in Fig. 6.8. LP_{11}(odd) mode shows an extraordinarily higher confinement loss than that of the LP_{11}(even) mode at a shorter wavelength, and can not be guided by this PCF. The measured loss at 1.3μm for the LP_{11}(even) mode are 0.55dB/m and 0.11dB/m for the *x*- and *y*-polarization, respectively. The discrepancy between the calculated confinement loss and measured loss is attributed to the idealized modeling of the Hi-Bi PCF.

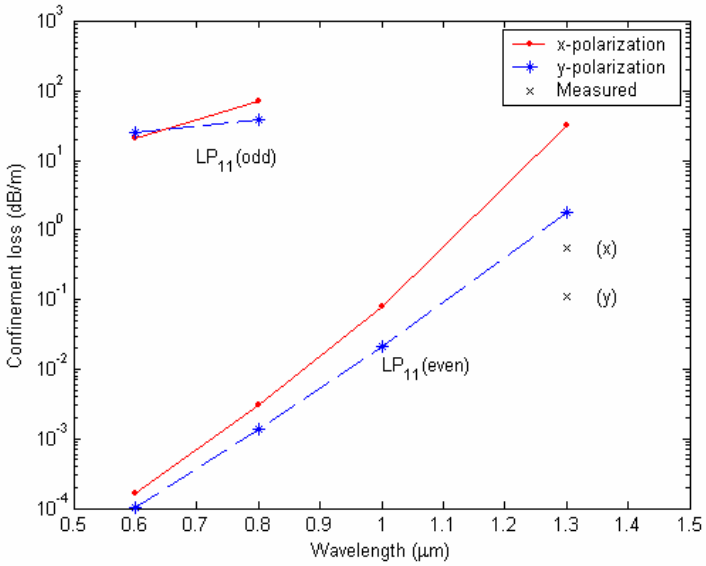

Figure 6.8 Confinement loss of LP_{11}(even) and LP_{11}(odd) mode of the two-mode Hi-Bi PCF with 10 rings of air-holes. (d_1/Λ = 0.54, d_2/Λ = 0.97, and Λ = 4.18μm)

The beat length between the LP_{01} and LP_{11}(even) mode is of particular importance for a lot of two-mode fiber-optic components and devices. The calculated beat length between the LP_{01} and LP_{11}(even) mode is shown in Fig. 6.9, indicating a shorter beat

length at long wavelength. For a perfectly two-fold symmetrical structure of this Hi-Bi PCF, the beat length in theory is the same for the *x*- and *y*-polarization except at wavelength ~1.4μm, where the LP_{11}(even) mode approaches the cutoff wavelength.

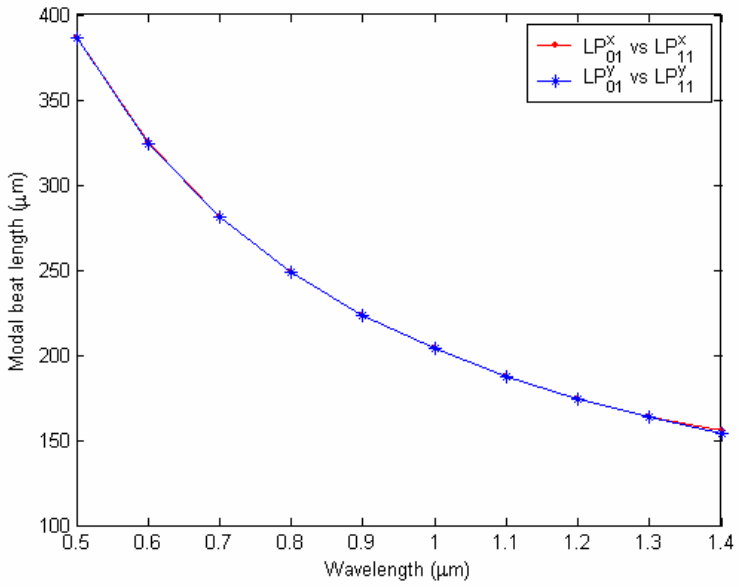

Figure 6.9 LP_{01} and LP_{11}(even) mode beat length as a function of wavelength.

6.4 Summary

In summary, we have explored possible structures of the index-guiding PCF for two-mode operation. Simulations showed that a PCF with d/Λ value from 0.45 to 0.65 supports only the fundamental mode and the first higher order modes with a broad wavelength range covering the transparent window of silica. However, the instable lobe orientation of the second-order mode makes it impractical for sensing applications. We proposed a Hi-Bi PCF for two-mode applications, and found that it's capable to support the LP_{11}(even) mode while suppress the LP_{11}(odd) mode. This has greatly expanded the two-mode operation to an unthinkable wavelength range from 400nm-2000nm, which was further confirmed by the confinement loss calculation for

this Hi-Bi PCF. For a similar PCF structure designed as a highly birefringent PCF with $d_1/\Lambda = 0.536$, $d_2/\Lambda = 0.974$, and $\Lambda = 4.179\mu m$, we have theoretically calculated its dispersion curve and found that it has a two-mode wavelength range over 1000nm (400nm-1400nm). We'll experimentally confirm this valuable modal property and demonstrate a two-mode interferometer in Chapter 7.

References for Chapter 6

1. B. Kuhlmey, R. McPhedran, and C. Martijn de Sterke, "Modal cutoff in microstructured optical fibers," *Opt. Lett.*, vol. 27, pp. 1684-1686, 2002.
2. N. Mortensen, J. Folkenberg, M. Nielsen, and K. Hansen, "Modal cutoff and the V parameter in photonic crystal fibers," *Opt. Lett.*, vol. 28, pp. 1879-1881, 2003.
3. J. Folkenberg, N. Mortensen, K. Hansen, T. Hansen, H. Simonsen, and C. Jakobsen, "Experimental investigation of cutoff phenomena in nonlinear photonic crystal fibers," *Opt. Lett.*, vol. 28, pp. 1882-1884, 2003.
4. J.N. Blake, B.Y. Kim, and H.J. Shaw, "Fiber-optic modal coupler using periodic microbending," *Opt. Lett.*, vol. 11, pp. 177-179, Mar. 1986.
5. W.V. Sorin, B.Y. Kim, and H.J. Shaw, "Highly selective evanescent modal filter for two-mode optical fibers," *Opt. Lett.*, vol. 11, pp. 581-583, Sept. 1986.
6. B.Y. Kim, J.N. Blake, H.E. Engan, and H.J. Shaw, "All-fiber acousto-optic frequency shifter," *Opt. Lett.*, vol. 11, pp. 389-391, 1986.
7. C. Poole, J. Wiesenfeld, A. McCormick, and K. Nelson, "Broadband dispersion

compensation by using the higher-order spatial mode in a two-mode fiber," *Opt. Lett.*, vol. 17, pp. 985-, 1992.

8. Park HS, Song KY, Yun SH, et al. “All-fiber wavelength-tunable acoustooptic switches based on intermodal coupling in fibers,” *J. of Lightwave Technol.*, vol. 20, pp. 1864-1868, Oct. 2002.
9. K.A. Murphy, M.S. Miller, A.M. Vengsarkar, and R.O. Claus, “Elliptical-core two-mode optical-fiber sensor implementation methods,” *J. of Lightwave Technol.*, vol. 8, pp. 1688-1696, Nov. 1990.
10. A.M. Vengsarkar, W.C. Michie, L. Jankovic, B. Culshaw, and R.O. Claus, “Fiber-optic dual-technique sensor for simultaneous measurement of strain and temperature,” *J. of Lightwave Technol.*, vol. 12, pp. 170-177, Jan. 1994.
11. B.Y. Kim, J.N. Blake, S.Y. Huang, and H.J. Shaw, “Use of highly elliptical core fibers for two-mode fiber devices,” *Opt. Lett.*, vol. 12, pp. 729-731, Sept. 1987.
12. W. Jin, Z. Wang, and J. Ju, “Two-mode photonic crystal fibers,” *Opt. Express*, vol. 13, pp. 2082-2088, 2005.
13. M. Layton and J. Bucaro, “Optical fiber acoustic sensor utilizing mode-mode interference,” *Appl. Opt.*, vol. 18, pp. 666-, 1979.
14. D. Kreit, R. Youngquist, and D. Davies, “Two-mode fiber interferometer /amplitude modulator,” *Appl. Opt.*, vol. 25, pp. 4433-, 1986.
15. J. Blake, S. Huang, B. Kim, and H. Shaw, “Strain effects on highly elliptical core two-mode fibers,” *Opt. Lett.*, vol. 12, pp. 732-, 1987.
16. K. Suzuki, H. Kubota, S. Kawanishi, M. Tanaka, and M. Fujita, “Optical properties of a low-loss polarization-maintaining photonic crystal fiber,” *Opt. Express*, vol. 9,

pp. 676-680, 2001.

17. H. Kubota, S. Kawanishi, S. Koyanagi, M. Tanaka, and S. Yamaguchi, “Absolutely single polarization photonic crystal fiber,” *IEEE Photon. Technol. Lett.*, vol.16, pp. 182-184, Jan. 2004.
18. J. Ju, W. Jin, and M.S. Demokan, “Two-mode operation in highly birefringent photonic crystal fiber,” *IEEE Photonics Technol. Lett.*, vol. 16, pp. 2472-2474, Nov. 2004.
19. G.P. Agrawal, *Nonlinear Fiber Optics*, Academic Press, 2001.

CHAPTER 7

SENSING APPLICATIONS OF TWO-MODE HI-BI PCF

For the two-mode Hi-Bi PCF discussed in Chapter 6, the second order mode LP_{11}(even) has a stable lobe orientation and two polarization principle axes. These special properties are extremely useful for two-mode fiber device and sensing application. In this chapter, we present the results of our theoretical and experimental investigation on the performance of a strain sensor and a temperature sensor based on the modal interference of LP_{01} and LP_{11}(even) modes in the Hi-Bi PCF, and discuss the possibility of simultaneous strain and temperature measurement using such PCF modal interference sensor.

7.1 Two mode interferometer based on Hi-Bi PCF

A two-mode fiber sensor uses a differential interferometric scheme where the interference between the LP_{01} and the LP_{11}(even) modes of the fiber leads to a two-lobe pattern in the far-field of the output [1-2]. In the scheme that uses circular core two-mode fibers, the four-fold degeneracy of the LP_{11} modes results in instability of the cross-sectional intensity distribution, which imposes obstacles in practical implementation of sensing applications. As a consequence, the degeneracy of LP_{11}

modes needs to be lift and a highly elliptical core fiber can remedy this situation [2-4]. As has been shown in Chapter 6, we found a properly designed Hi-Bi PCF shows similar properties with that of the elliptical core fiber but with a much wider two-mode wavelength range, over which only the LP_{01} and LP_{11}(even) modes propagate with a stable intensity distribution along the length of the fiber [5].

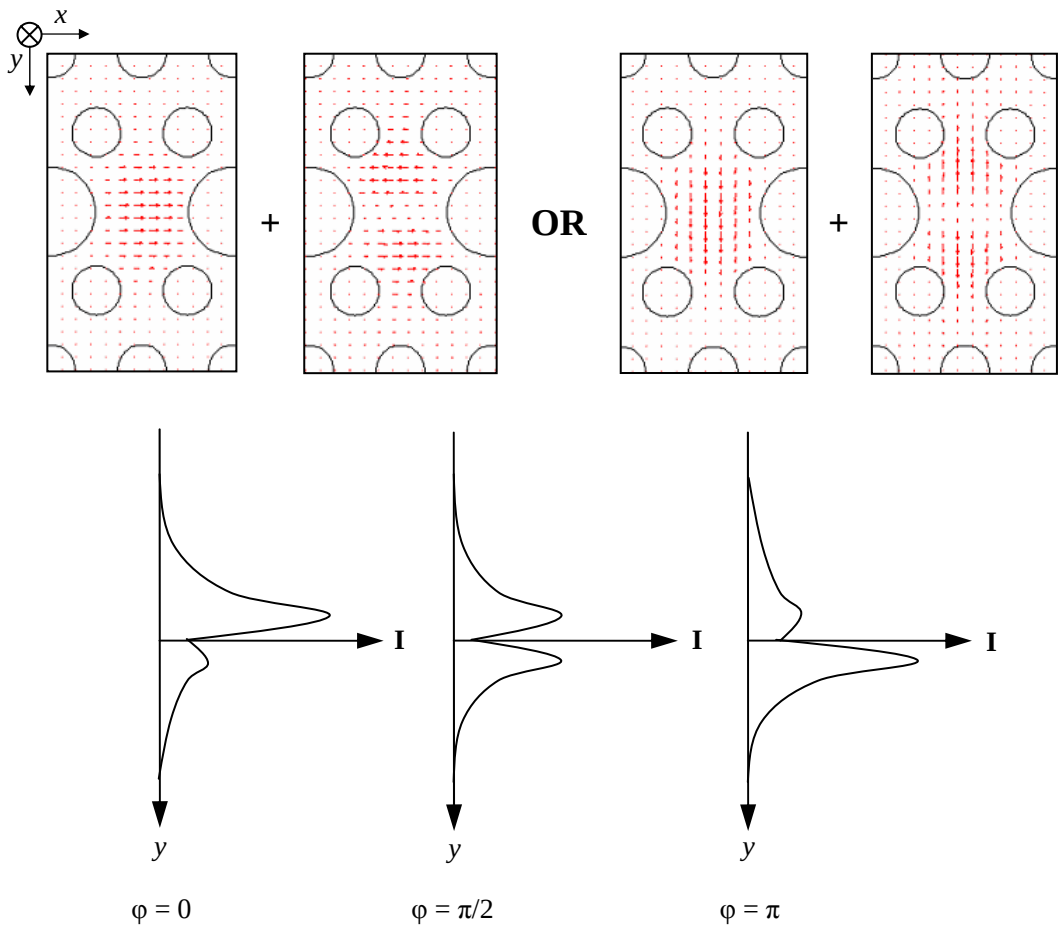

Figure 7.1 Evolution of the far-field patterns as a function of phase difference between LP_{01} and LP_{11}(even) modes.

Fig. 7.1 shows the schematic plots of the far field patterns as a result of phase difference change between the LP_{01} and LP_{11}(even) modes. When the LP_{01} and LP_{11}(even) modes are excited equally in the Hi-Bi PCF, the far-field output radiation pattern will be a superposition of the contribution from the two modes and will be a

function of the relative phase difference between them. The evolution of the far-field radiation for different phase difference φ results in variation in the two-lobed intensity patterns, as shown in Fig. 7.1. For a change in φ of 2π there will be one complete oscillation of the intensity pattern.

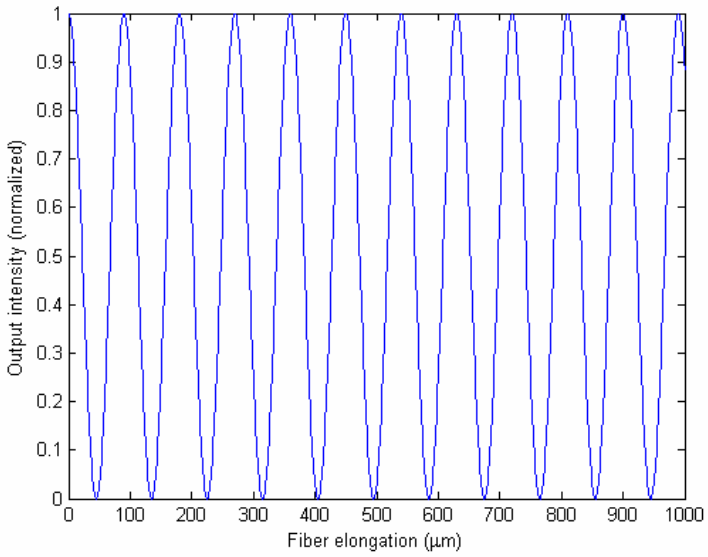

(a)

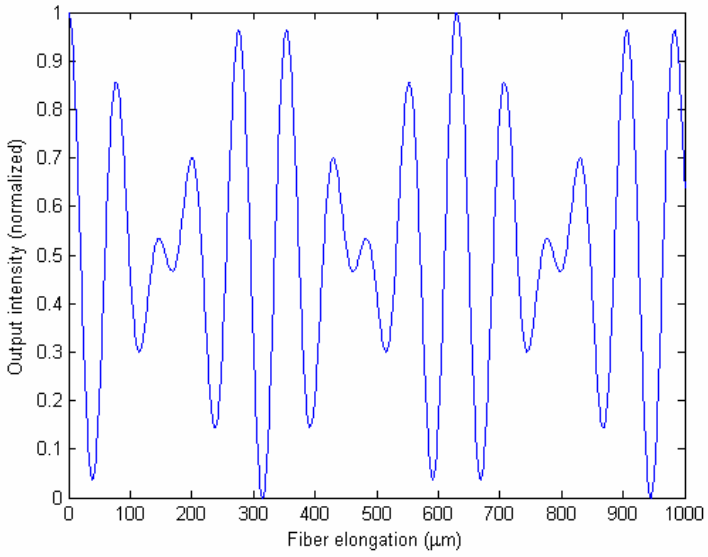

(b)

Figure 7.2 Theoretical output intensity pattern for linearly polarized light launched into the two-mode PCF. Polarizer angle: (a) π/2, (b) π/4.

An external disturbance, e.g. strain or temperature, applied on the PCF leads to a differential phase shift between these two modes, resulting in an oscillation of the two-lobe pattern. A spatial demodulator monitoring one of the two-lobe patterns at the far-field converts this oscillation into an intensity variation. When only the *x*- or *y*-polarization of LP_{01} and LP_{11} modes were excited at the entrance, a quasi-sinusoidal intensity waveform is obtained after the spatial demodulator (Fig. 7.2a). However, if both the *x*- and *y*-polarization are excited, two set of interference signals corresponding to the orthogonal polarization states are superimposed, resulting in an amplitude-modulated waveform (Fig. 7.2b).

The two-mode Hi-Bi PCF (pitch Λ = 4.179μm, diameters of small holes d_1 = 2.239μm, and diameters of larger holes d_2 = 4.069μm.) used in the present work is manufactured by Blaze Photonic [5] and the modal properties were analyzed in detail in Chapter 6. In the following sections, I present the results of our experimental investigation on the strain and temperature sensitivity of the two-mode sensor and discuss the possibility of using it for simultaneous measurement of strain and temperature.

7.2 Strain sensing

A schematic of the experimental setup is shown in Fig. 7.3. Light from a laser was coupled into a piece of Hi-Bi PCF with an alignment system consisting of a pair of lenses, a polarizer, a fiber holder and a 5-dimensional translation stage. The PCF has a total length of ~1 meter and is epoxy-bounded to a fixed stage and a translation stage. The 50cm PCF in between the two stages can be axially strained through a computer

controlled translation stage. An infrared TV camera with lens removed is placed near the output of the fiber to monitor one of two-lobe patterns at the far-field intensity, as indicated in the rectangular region in the right panel of Fig. 7.3. Alternatively, it is possible to use a lead-out fiber which is offset from the two-mode PCF to pick up the maximum contrast ratio in the intensity of the two-lobe output.

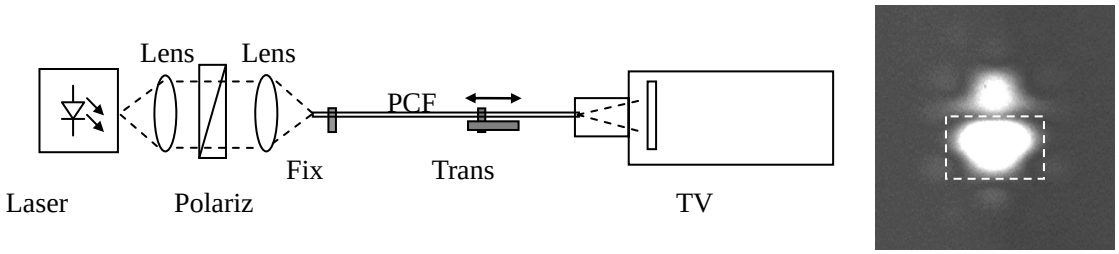

Figure 7.3 Experimental setup for strain measurement and far-field intensity.

Experiments were conducted at wavelength of 650nm, 780nm, 850nm, 980nm, 1300nm and 1550nm by using semiconductor lasers. At each wavelength, before applying axial strain to the PCF, the far field pattern at the fiber output was observed with the launching conditions varied. It confirmed that at wavelengths from 650nm to 1300nm, the fiber support only fundamental LP_{01} mode and LP_{11}(even) mode, and no higher mode was observed. The intensity-lobe orientation of the LP_{11}(even) mode was found stable even when the launching condition is changed. At 1550nm, only the LP_{01} mode can be observed, and no second order mode was observed. These observations agree with the theoretical prediction in the Chapter 6.

The strain sensitivity of the two-mode sensor for the five wavelengths from 650nm to 1300nm was then measured. Before each test, the launching condition was adjusted so that the two modes are launched with approximately equal intensity. This can be achieved by adjusting the offset of the focused incident beam with respective to the axis of the PCF. Taking the operation at 1.3μm as an example, the focused beam has a

diameter of ~3.7μm, giving a calculated maximum launching efficiency of 70% for the fundamental LP_{01} mode at zero offset and 23% for the LP_{11}(even) mode at 3.9μm offset. The intensities of the two modes are equalized at 3.4μm offset with launching efficiency of ~22%. The two modes interfere at the fiber output, resulting in a far field intensity distribution that varied with the phase difference between the two modes. In Fig. 7.4 the evolution of far-field intensity distribution at λ=1.3μm for phase differences of 0, π/2 and π are shown. For a change of 2π phase difference there will be one complete evolution.

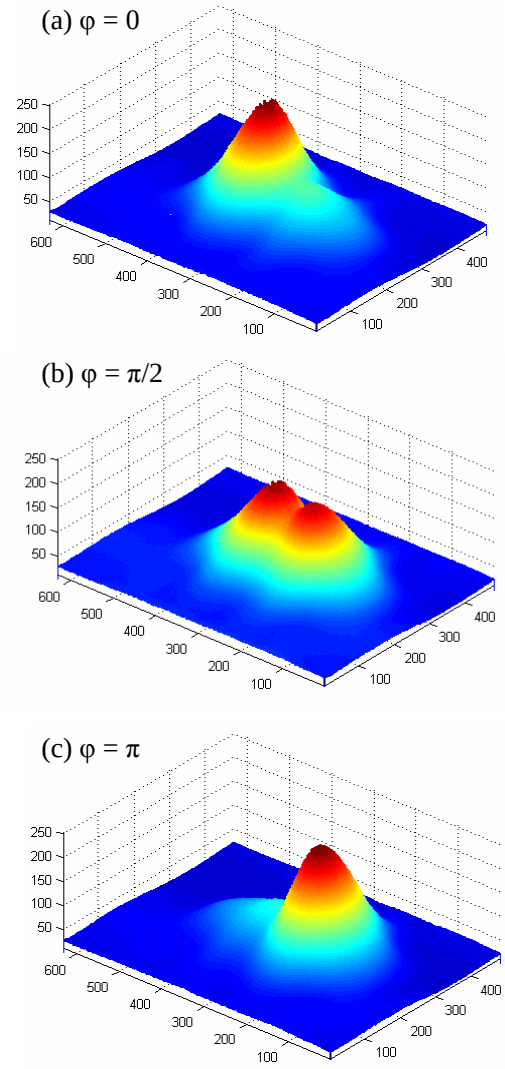

Figure 7.4 Measured far-field two-lobe pattern in two-mode Hi-Bi PCF for different phase shift (λ = 1300nm).

Fig.7.5 shows the measured intensity variation at one of the lobes when the PCF was elongated from 0 to 2mm. The curves from top to bottom correspond to respectively polarizer set to 0^o, 90^o, and 45^o, in respect to the *x*-axis as shown in Fig. 7.1. At 0^o and 90^o, the intensity variation is due to the interference of LP_{01} and LP_{11}(even) modes for the *x*- and *y*-polarization, respectively. They are approximately sinusoidal and the elongation $\delta L_{2\pi}$, which is defined as the elongation required for the intensity oscillation to undergo a complete 2π phase shift, is 124.4μm and 144.9μm, respectively. At a launch angle of 45^o respective to the principle axis of PCF, the two sets of interference patterns, corresponding to two orthogonal polarizations, are superimposed, resulting in an amplitude-modulated wave as shown in the lower graph of Fig. 7.5.

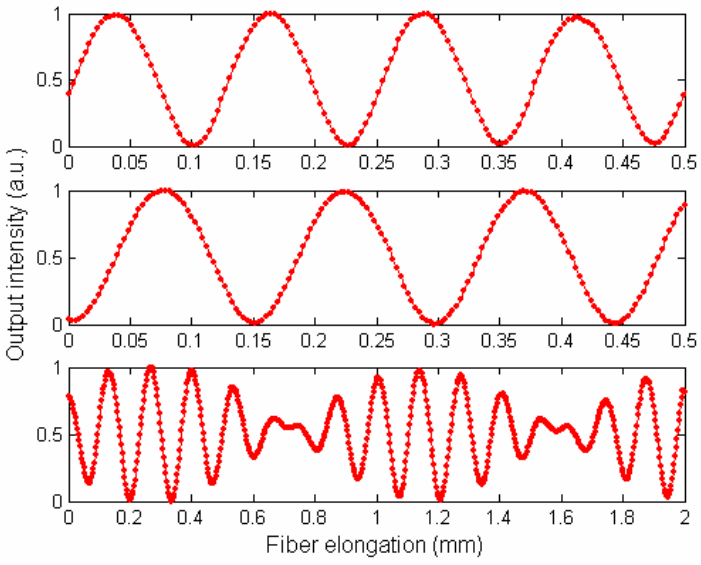

Figure 7.5 Experimental results for different launch angles of 0^o, 90^o, and 45^o (from top to bottom).

The values of $\delta L_{2\pi}$ for various wavelengths for both polarizations are shown in Fig. 7.6. Also included in the figure are the calculated beat lengths between the LP_{01} and the LP_{11}(even) modes when the PCF is unstrained (solid line). Contrary to elliptical

core two-mode fibers [3, 6], both the modal beat lengths and the elongation needed to produce 2π phase change decrease with the optical wavelength, indicating higher strain sensitivity at longer wavelengths. The values of strain sensitivity, which is defined as the rate of change of the phase difference between the two modes with respect to strain, are listed in Table 7.1 and shown in Fig. 7.7. The strain sensitivity shows a linear relationship with respect to the optical wavelength.

Table 7.1 Strain sensitivity (rad/με)

	λ = 650nm	λ = 780nm	λ = 850nm	λ = 980nm	λ = 1310nm
x-polarization:	0.029	0.033	0.035	0.040	0.05
y-polarization:	0.024	0.028	0.029	0.034	0.043

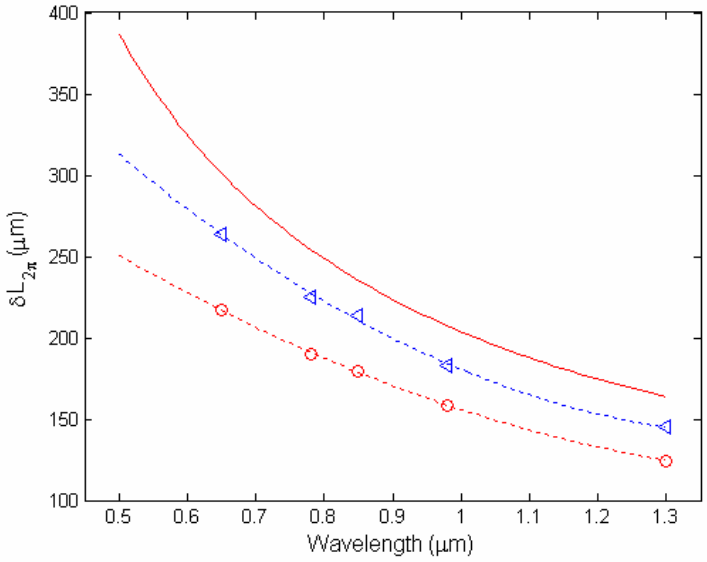

Figure 7.6 Measured $\delta L_{2\pi}$ as a function of operating wavelength for two polarization states (circle: *x*-polarization, triangle: *y*-polarization).

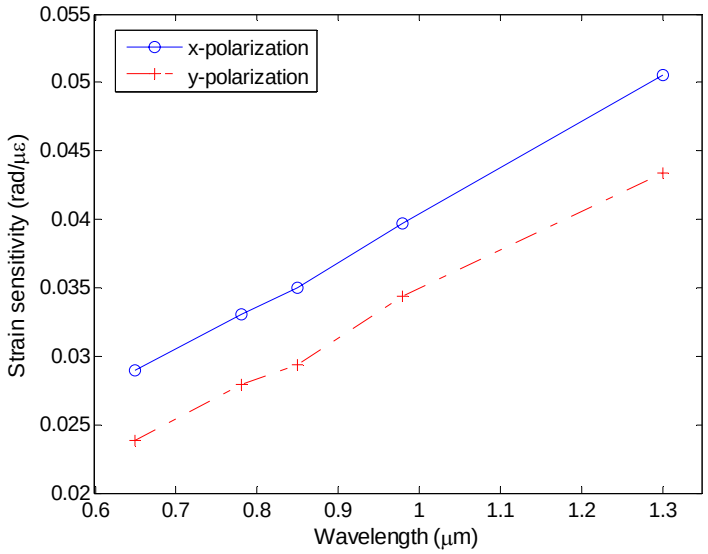

Figure 7.7 Strain sensitivity as a function of wavelength.

7.3 Temperature sensing

The experimental setup used for measuring the temperature sensitivity is shown in Fig. 7.8. A polarizer is placed at the input, which allows the launching of a linear polarization to one of the principal axes of the PCF. An infrared camera with lens removed is placed at the output to monitor the far-field intensity distribution. The two modes were excited approximately equally by an offset introduced at the input. A section of PCF (~1.8 meters) was heated by putting it inside an oven.

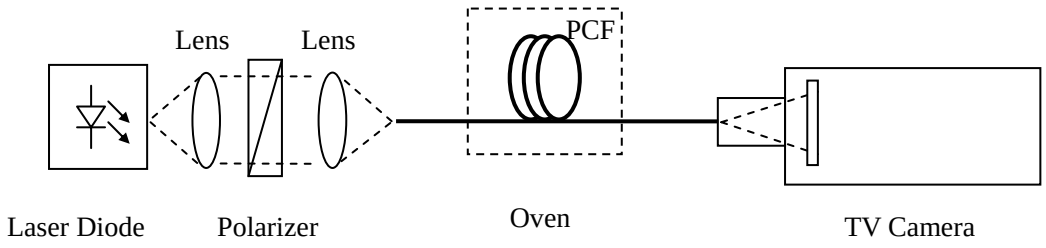

Figure 7.8 Experimental setup for temperature measurement.

Measurements were performed for both the *x*- and *y*-polarization. Fig. 7.9 shows an example of the output intensity of the two-mode interferometer at 1300nm as a function of oven temperature when the input polarization is aligned to the *x*-axis. One

complete cycle in the intensity variation corresponds to a 2π change in the phase difference between the LP_{01} and LP_{11}(even) modes. We noticed that the period of the intensity oscillation is not constant during the temperature range from 20°C to 120°C, and the period is obviously larger at lower temperatures, indicating that the interferometer shows a non-linear response to the temperature changes. The temperature sensitivity η, defined as the rate of change of phase difference $\Delta\phi$ between the two modes with respect to temperature T per unit length of sensing fiber, is given by

$$\eta = \frac{1}{L} \cdot \frac{\Delta \phi}{\Delta T} \tag{7.1}$$

where L is the fiber length placed inside the oven. The measured average temperature sensitivities within the temperature range from 20°C to 120°C are listed in Table 7.2 and shown in Fig. 7.10. As can be seen from Table 7.2, the temperature sensitivity of TM PCF is slightly different for the *x*- and *y*-polarization. And the values are in general smaller than that of the conventional elliptical core two-mode fibers [6].

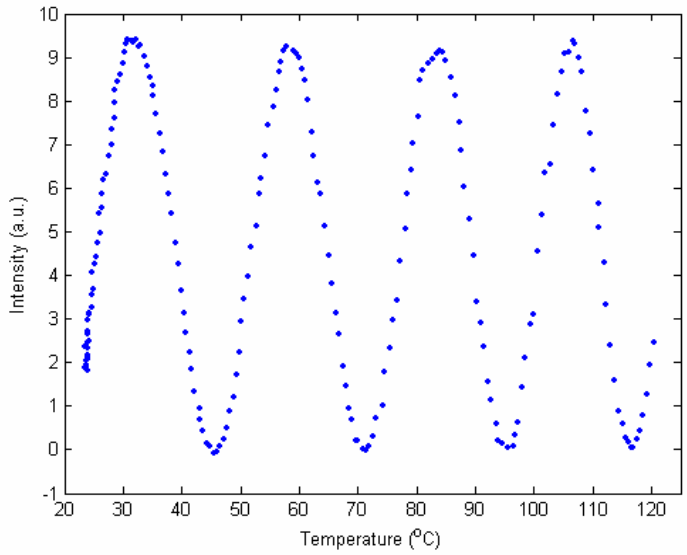

Figure 7.9 Experimental results showing the periodic intensity variation with temperature. (λ=1310nm, *x*-polarization).

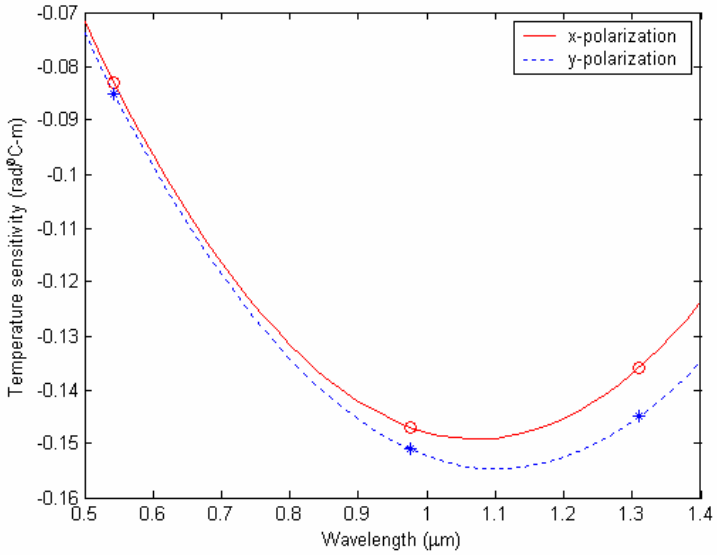

Figure 7.10 Measured temperature sensitivity for x-polarization (circle) and y-polarization (star) as a function of optical wavelength. Solid and dashed lines are curve fitting results of the measured data.

Table 7.2 Temperature sensitivity (rad/°C-m)

	λ = 543nm	λ = 975nm	λ = 1310nm
x-polarization:	0.083	0.147	0.136
y-polarization:	0.085	0.151	0.145

It can be seen from Fig. 7.10 that the temperature sensitivity has a non-monotonic dependence on wavelength. To understand the origin of this non-monotonic dependence, we conducted theoretical analysis on the temperature sensitivity. The temperature sensitivity, η, may be re-written as

$$\eta = \frac{1}{L}\frac{\Delta\phi}{\Delta T} = \frac{1}{L}\cdot\frac{\partial(\Delta\beta\cdot L)}{\partial T} = \frac{\partial(\Delta\beta)}{\partial T} + \Delta\beta\cdot\frac{1}{L}\frac{\partial L}{\partial T} \tag{7.2}$$

where $\Delta\beta$ is the propagation constant difference between the LP_{01} and LP_{11}(even) modes. As the PCF is a single material fiber, the thermal expansion coefficient α and thermo-optic coefficient κ should be the same for both the core and cladding, which are respectively defined as

$$\alpha = \frac{1}{L}\cdot\frac{\partial L}{\partial T} \quad \text{and} \quad \kappa = \frac{1}{n}\cdot\frac{\partial n}{\partial T} \tag{7.3}$$

where n is the refractive index of PCF material, which is pure silica. For fused silica, the thermal expansion coefficient and thermo-optic coefficient are $\alpha = 5\cdot10^{-7}/^{o}\text{C}$ and $\kappa = 1\cdot10^{-5}/^{o}\text{C}$, respectively [6].

By applying a super-cell method [7], we can calculate the propagation constants of the two modes at different temperatures. Although the temperature induced cross-sectional change was intuitively regarded as small, simulation results shown in Fig. 7.11 illustrate that its influence over the propagation constant difference $\Delta\beta$ should be taken into consideration. However, in both cases, the differential propagation constant $\Delta\beta$ was found to vary linearly with the temperature, which can be conveniently used to evaluate the first part of Eq. (2) by calculating the slope of the curve.

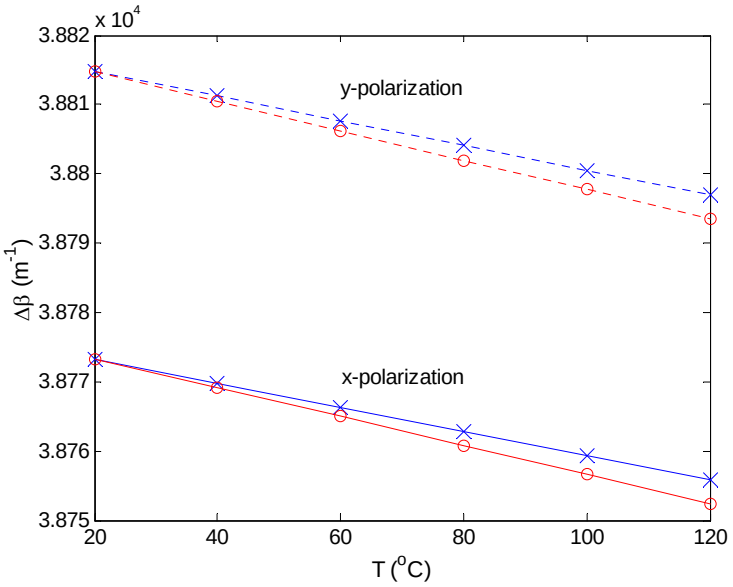

Figure 7.11 Propagation constant difference $\Delta\beta$ at 1310nm as functions of temperature. Circle and Cross lines represent the results with and without considering transverse thermal expansion.

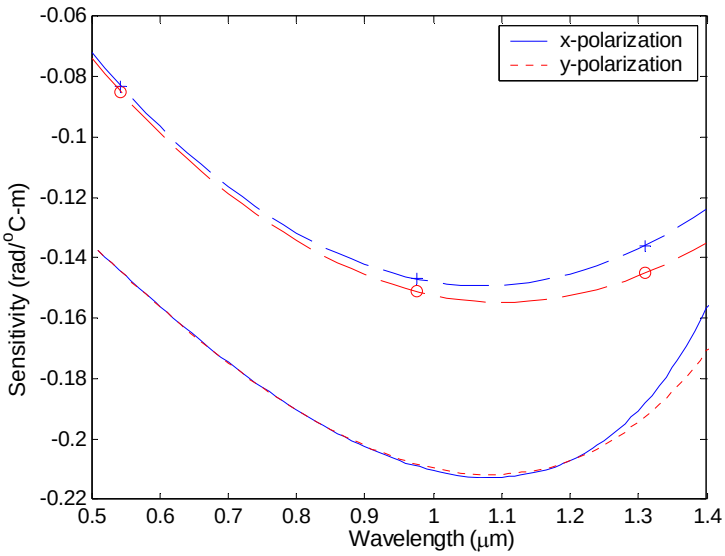

Figure 7.12 Calculated temperature sensitivities as functions of wavelength. Solid and dotted lines correspond to theoretical results for the *x*- and *y*-polarization. Cross and circle points correspond to experimental data of *x*- and *y*-polarization, and dashed lines correspond to curve-fitting results.

The theoretically calculated temperature sensitivity as a function of wavelength is shown in Fig. 7.12. The theoretical sensitivity of TM PCF has negative values and a parabolic-like shape with respect to the optical wavelength. The theoretical sensitivities agree in trends with the experimentally measured results. We believe the difference between the measured and the calculated values is caused by discrepancy between the parameters of an idealized fiber modeling and that of the real fiber which has non-circular holes and non-uniform hole distribution (Fig. 6.6).

To understand the non-monotonic dependence of temperature sensitivity on the optical wavelength, further theoretical investigation was conducted. First, simulation indicated the contribution of the thermo-optic effect to the overall temperature sensitivity is an order of magnitude higher than that of the fiber elongation ($\sim 3\times10^{-3}$) and transverse cross-section expansion ($\sim 4\times10^{-2}$). We thus neglect the latter two factors

and concentrate on the thermo-optical effect to the propagation constants. The sensitivity can now be re-written as

$$\eta' = \frac{1}{L}\frac{\Delta\phi}{\Delta T} = \frac{1}{L}\cdot\frac{\partial(\Delta\beta\cdot L)}{\partial T} = \frac{\partial(\Delta\beta)}{\partial T} = \frac{\partial(\Delta\beta)}{\partial n}\cdot\frac{\partial n}{\partial T} = n\kappa\cdot\frac{\partial(\Delta\beta)}{\partial n} \tag{7.4}$$

substituting $\Delta\beta = \frac{2\pi}{\lambda}\left(n_{eff}^{01} - n_{eff}^{11}\right)$ to Eq. (7.4), where n_{eff}^{01} and n_{eff}^{11} are the effective index of the LP_{01} and LP_{11}(even) mode, respectively, the temperature sensitivity can be written as

$$\eta' = n\kappa\cdot\frac{\partial(\Delta\beta)}{\partial n} = n\kappa\cdot\frac{2\pi}{\lambda}\cdot\left(\frac{\partial n_{eff}^{01}}{\partial n} - \frac{\partial n_{eff}^{11}}{\partial n}\right) \tag{7.5}$$

where $\frac{\partial n_{eff}^{01}}{\partial n}$ and $\frac{\partial n_{eff}^{11}}{\partial n}$ is the rate of change of the effective index of the LP_{01} and LP_{11}(even) mode with respect to the background refractive index of silica, which has been shown in Fig. 7.13. For the LP_{01} mode $\frac{\partial n_{eff}^{01}}{\partial n}$ shows a linear relationship with respect to the optical wavelength. However, $\frac{\partial n_{eff}^{11}}{\partial n}$ of the LP_{11}(even) mode shows a parabolic-like shape with respect to the optical wavelength when the optical wavelength is approaching its cutoff wavelength (~1.32μm). The difference between $\frac{\partial n_{eff}^{01}}{\partial n}$ and $\frac{\partial n_{eff}^{11}}{\partial n}$ shows a non-monotonic dependence on wavelength as shown in Fig. 7.12.

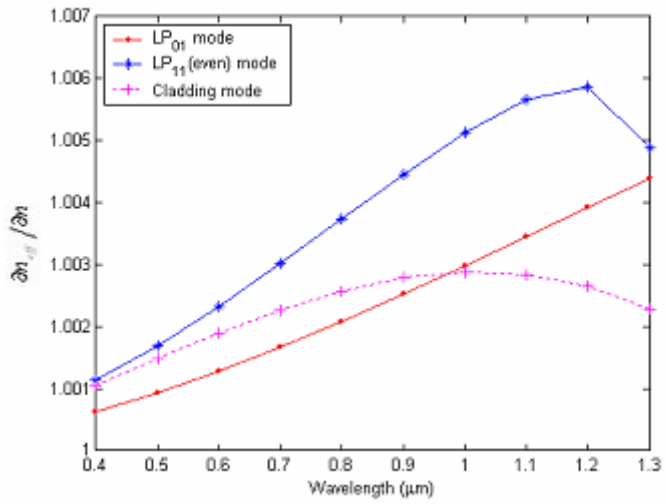

Figure 7.13 $\partial n_{eff} / \partial n$ as a function of wavelength for LP_{01}, LP_{11}(even) and cladding mode.

7.4 Simultaneous measurement of strain and temperature

The extremely broad two-mode wavelength range [8] and the unusual wavelength-dependent temperature sensitivity of the two-mode PCF sensor provide a useful means for strain and temperature discrimination. As has already shown in Fig. 7.7, the strain sensitivities increase linearly with wavelength and are significantly different (~15%) for the two orthogonal polarizations. The temperature sensitivities have non-monotonic dependence on wavelength (Fig. 7.10) and are similar for both polarizations.

Now consider a two-mode interferometer interrogated simultaneously at two wavelengths (λ_1 and λ_2). For a particular polarization (e.g., *x*-polarization), the measurement equations may be expressed as

$$\begin{bmatrix} \Delta\phi_1 \\ \Delta\phi_2 \end{bmatrix} = \begin{bmatrix} K_1^T & K_1^\varepsilon \\ K_2^T & K_2^\varepsilon \end{bmatrix} \begin{bmatrix} T \\ \varepsilon \end{bmatrix} \tag{7.6}$$

where $\Delta\phi_1$ and $\Delta\phi_2$ are the measured phase difference between the two modes at λ_1 and λ_2, respectively. The units of $\Delta\phi_i$ (i=1,2) is radians. K_i^T and K_i^ε are the

temperature and strain sensitivities at λ_i (i=1,2), and can be obtained from Fig. 7.7 and Fig. 7.10, respectively. The strain (ε) and temperature (T) have units of microstrain ($\mu\varepsilon$) and ^{o}C respectively and can be recovered in principle from Eq.(7.6) as long as the determinant of the transfer matrix, i.e., $|\Delta_0| = \left|K_1^T K_2^\varepsilon - K_2^T K_1^\varepsilon\right|$ is not equal to zero.

It is obvious that a temperature-independent strain measurement can be realized by operating the interferometer at two wavelengths where the temperature sensitivities are the same, i.e., $K_1^T = K_2^T$, as shown in Fig. 7.10. Taken the case of λ_1 = 840nm and λ_2 = 1310nm as an example, for x-polarization, the transfer matrix elements are $K_1^T = K_2^T = -0.136$, $K_1^\varepsilon = 0.035$ and $K_2^\varepsilon = 0.05$, and strain measurement can be performed by equation

$$\Delta\phi_2 - \Delta\phi_1 = (K_2^\varepsilon - K_1^\varepsilon)\varepsilon = 0.015\ \varepsilon \tag{7.7}$$

In the following, we will study the errors in the recovery of strain (ε) and temperature (T) for the aforementioned measurement scheme (i.e., λ_1 = 840nm, λ_2 = 1310nm) and two other schemes with the following pairs of operating wavelengths: λ_1 = 745nm and λ_2 = 1400nm; and λ_1 = 940nm, λ_2 = 1205nm. The three schemes have a common characteristics, i.e., the temperature sensitivities at the two wavelengths in each of the schemes are the same and hence temperature-insensitive strain measurement may be performed by a similar process as in Eq.(7.7).

The errors in T and ε can be due to the errors in the phase measurements or errors in the determination of the matrix elements. A general analysis of errors transformation can be found in previous papers [9-10]. For the case where phase measurement error (i.e. $\Delta\phi_i$) is dominant, the errors in strain and temperature recovery may be estimated by using: [9-10]

$$\begin{aligned} |\delta T| &\le \frac{\left|K_2^{\varepsilon}\right| + \left|K_1^{\varepsilon}\right|}{\Delta_0} |\delta\phi| \\ |\delta\varepsilon| &\le \frac{\left|K_2^{T}\right| + \left|K_1^{T}\right|}{\Delta_0} |\delta\phi| \end{aligned} \tag{7.8}$$

where $\delta\phi$ is the maximum error in the determination of $\Delta\phi_i$ (i=1, 2), δT and $\delta\varepsilon$ are the errors in T and ε. Assuming a maximum phase measurement error of $\delta\phi = \pi/100$ radians for 1 meter length of fiber, the errors in the recovery of T and ε are given for the three aforementioned schemes are calculated and given in Table 7.3.

Table 7.3 Strain and Temperature Errors

Error	λ_1 = 745nm, λ_2 = 1400nm	λ_1 = 840nm, λ_2 = 1310nm	λ_1 = 940nm, λ_2 = 1205nm
T (^{o}C)	0.97	1.29	2.1
ε (με)	2.86	4.18	7.13

If the matrix elements have errors and are dominant over the phase measurement error, the relative errors in recovering T and ε may be estimated by [9]:

$$\begin{aligned} \left|\frac{\delta T}{T}\right|_{\max} &\approx \frac{\left|K_1^T K_2^{\varepsilon}\right| + \left|K_1^{\varepsilon} K_2^T\right| + 2\left|\varepsilon/T\right|\left|K_1^{\varepsilon} K_2^{\varepsilon}\right|}{\left|\Delta_0\right|} |\gamma| \\ \left|\frac{\delta\varepsilon}{\varepsilon}\right|_{\max} &\approx \frac{\left|K_1^{\varepsilon} K_2^T\right| + \left|K_1^T K_2^{\varepsilon}\right| + 2\left|T/\varepsilon\right|\left|K_1^T K_2^T\right|}{\left|\Delta_0\right|} |\gamma| \end{aligned} \tag{7.9}$$

where $|\gamma|$ is the maximum relative (or fractional) errors for all the elements of the matrix and assumed to be the same. It should be mentioned that a detailed evaluation of errors due to matrix elements' inaccuracy is complicated and Eq.(7.9) only gives the worst case results. The actual errors could be smaller than that estimated by Eq.(7.9). Nevertheless, Eq.(7.9) gives the limit of the maximum possible error.

It can be seen from Eq.(7.9) that the relative temperature recovery error ($|\delta T/T|$) increases with ε and reaches a maximum when the sensor operates at the strain limit

(ε_{max}). $|\delta T/T|$ also increases with a decrease in T and hence the measurement error δT increase for smaller temperature variation T. The minimum measurable temperature variation may be determined by setting $|\delta T/T|_{max}=1$, i.e. the temperature measurement has a signal-to-noise ratio of 1. The minimum measurable strain may also be evaluated by setting $|\delta\varepsilon/\varepsilon|_{max} = 1$ and with $T = T_{max}$. . As a working illustration, we assume 1% error in the determination of the matrix elements ($|\gamma|$=1%), a strain range of 3000με (ε_{max}=3000με) and a temperature excursion of 30°C (T_{max}=30°C), The recovery errors caused by the inaccuracies in the matrix elements are calculated using (7.9) and results are shown in Table 7.4.

Table 7.4 Minimum Detectable Strain and Temperature

	λ_1 = 745nm, λ_2 = 1400nm	λ_1 = 840nm, λ_2 = 1310nm	λ_1 = 940nm, λ_2 = 1205nm
ε (με):	3.5	5.1	11
T (°C):	40	49	94

As shown in Table 7.3 and Table 7.4, the three measurement schemes are relatively insensitive to phase measurement error; however, they are more significantly affected by the errors in the matrix elements. The minimum detectable strains as shown in Table 7.3 are comparable to, in some cases better than, the conventional sensing schemes [9], indicating the PCF-based two-mode sensors are good at performing temperature insensitive strain measurement. However, the performance is very sensitive to error of transfer matrix elements and hence is not a good candidate for temperature measurement. The best strain measurement performance is obtained with the scheme of λ_1 = 745nm and λ_2 = 1400nm, where the wavelength spacing (λ_2 - λ_1) is the largest.

For comparison, we summarized the various schemes for simultaneous measurement of strain and temperature in Table 7.5. The highest resolution was obtained by a joint evaluation of fiber optical path length and fiber dispersion [16], but it was a very complex experimental setup. Polarimetric and two-mode differential interferometric schemes incorporated in a conventional elliptical-core fiber showed a good resolution and they're easy to construct. We expected a higher resolution can be obtained by the proposed two-mode PCF sensor by operating it at two different optical wavelengths (last row in Table 7.5). We have shown that temperature T and strain ε can be obtained by the inverse of the transfer matrix of Eq. (7.6).

$$\begin{bmatrix} T \\ \varepsilon \end{bmatrix} = \begin{bmatrix} K_1^T & K_1^\varepsilon \\ K_2^T & K_2^\varepsilon \end{bmatrix}^{-1} \begin{bmatrix} \Delta\phi_1 \\ \Delta\phi_2 \end{bmatrix} = \begin{bmatrix} L_{11} & L_{12} \\ L_{21} & L_{22} \end{bmatrix} \begin{bmatrix} \Delta\phi_1 \\ \Delta\phi_2 \end{bmatrix} \tag{7.10}$$

The resolution of temperature and strain can be estimated by the following equation

$$\begin{aligned} \Delta T &\le |L_{11}||\Delta\phi_1| + |L_{12}||\Delta\phi_2| \\ \Delta\varepsilon &\le |L_{21}||\Delta\phi_1| + |L_{22}||\Delta\phi_2| \end{aligned} \tag{7.11}$$

Assuming the measurement resolution of phase is 1°, i.e. $|\Delta\phi_1| = |\Delta\phi_2| = \pi/180$, the resolution is estimated to be 1.8°C and 3.3με for temperature and strain when the operating wavelengths are chosen to be λ_1=0.4μm and λ_2 =1.4μm.

Principles	Resolution	Complexity
Two-mode (*x*- & *y*-)[6]	n/a	Easy
Polarimetric + two-mode[11]	n/a	Medium
Polarimetric + two-mode[12]	10με/2°C	Medium
F-P + two-mode[13]	±10μ m/±5°C	Easy
FBG (λ_1 λ_2)[14]	±17μm/±1°C	Complex
Optical path + Dispersion[15]	0.1με/1°C	Complex
Brillouin-scattering[16]	100με/4°C	Complex
LPG (λ_1 λ_2)[17]	30με/0.6°C	Complex
two-mode PCF	3.3με/1.8°C	Easy

Table 7.5 Simultaneous measurement of strain and temperature: a comparison

7.5 Summary

In summary, a two-mode interferometer based on LP_{01} and LP_{11}(even) mode interference is demonstrated for the first time for axial strain and temperature measurement. It was found that there exists a broad band two-mode operation wavelength range over 760nm, where only the LP_{01} and LP_{11}(even) mode can be guided. For the strain sensor, the fiber elongations needed to produce 2π phase change decrease with the wavelength, indicating higher strain sensitivity at longer wavelengths. The strain sensitivity is highly polarization-dependent. The temperature sensitivity of the two-mode PCF sensor was measured and it showed a non-monotonic dependence on the operating wavelength. We present a theoretical analysis of the non-monotonic wavelength response. The theoretical sensitivities agree in trends with the experimentally measured results. The unique strain and temperature sensitivities of the

two-mode Hi-Bi PCF described in this chapter can be used to perform temperature insensitive strain measurement. At the end of this chapter, we present a theoretical error analysis on the performance of the two mode interferometric sensor for simultaneous strain and temperature measurement. The results indicated that the PCF-based two-mode sensors are good at performing temperature insensitive strain measurement. However, the performance is more sensitive to error of transfer matrix elements and is not a good candidate for temperature measurement. The best strain measurement performance is recommended with the scheme of λ_1=745nm and λ_2=1400nm, where the wavelength spacing (λ_2-λ_1) is the largest.

References for Chapter 7

1. M. Layton and J. Bucaro, “Optical fiber acoustic sensor utilizing mode-mode interference,” *Appl. Opt.*, vol. 18, pp. 666-, 1979.
2. B.Y. Kim, J.N. Blake, S.Y. Huang, and H.J. Shaw, “Use of highly elliptical core fibers for two-mode fiber devices,” *Opt. Lett.*, vol. 12, pp. 729-731, Sept. 1987.
3. J. Blake, S. Huang, B. Kim, and H. Shaw, “Strain effects on highly elliptical core two-mode fibers,” *Opt. Lett.*, vol. 12, pp. 732-734, 1987.
4. B.Y. Kim, J.N. Blake, H.E. Engan, and H.J. Shaw, “All-fiber acousto-optic frequency shifter,” *Opt. Lett.*, vol. 11, pp. 389-391, 1986.
5. J. Ju, W. Jin, and M.S. Demokan, “Two-mode operation in highly birefringent photonic crystal fiber,” *IEEE Photonics Technol. Lett.*, vol. 16, pp. 2472-2474, Nov. 2004.

6. S.Y. Huang, J.N. Blake, and B.Y. Kim, “Perturbation effects on mode propagation in highly elliptical core two-mode fibers,” *J. Lightwave Technol.*, vol. 8, pp. 23-33, Jan. 1990.
7. Z. Wang, G. Ren, S. Lou, and W. Liang, “Investigation of the supercell based orthonormal basis function method for different kinds of fibers,” *Opt. Fiber Technol.*, vol. 10, pp. 296-311, 2004.
8. W. Jin, Z. Wang, and J. Ju, “Two-mode photonic crystal fibers,” *Opt. Express*, vol. 13, pp. 2082-2088, MAR 21 2005.
9. W. Jin, W.C. Michie, G. Thursby, M. Konstantaki, B. Culshaw, “Simultaneous measurement of strain and temperature: Error analysis,” *Optical Engineering*, vol. 36, pp. 598-609, 1997.
10. W. Jin, W.C. Michie, G. Thursby, M. Konstantaki, B. Culshaw, “Geometric representation of errors in measurements of strain and temperature,” *Optical Engineering*, vol. 36, pp. 2272-2278, 1997.
11. F. Farahi, D.J. Webb, J.D.C. Jones, D.A. Jackson, “Simultaneous measurement of temperature and strain – cross-sensitivity considerations,” *J. Lightwave Technol.*, vol. 8, pp. 138-142, Feb. 1990.
12. A.M. Vengsarkar, W.C. Michie, L. Jankovic, B. Culshaw, and R.O. Claus, “Fiber-optic dual-technique sensor for simultaneous measurement of strain and temperature,” *J. Lightwave Technol.*, vol. 12, pp. 170-177, Jan. 1994.
13. G.Z. Wang, A.B. Wang, K.A. Murphy, A.M. Vengsarkar, “Two-mode Fabry-Perot optical fibre sensors for strain and temperature measurement,” *Electron. Lett.*, vol. 27, pp. 1843 – 1845, Sept. 1991.

14. S.W. James, M.L. Dockney, R.P. Tatam, “Simultaneous independent temperature and strain measurement using in-fibre Bragg grating sensors,” *Electron. Lett.*, vol. 32, pp. 1133 – 1134, June 1996.

15. V. Gusmeroli and M. Martinelli, "Nonincremental interferometric fiber-optic measurement method for simultaneous detection of temperature and strain," *Opt. Lett.* vol. 19, pp. 2164-2166, 1994.

16. T.R. Parker, M. Farhadiroushan, V.A. Handerek, A.J. Roger, “A fully distributed simultaneous strain and temperature sensor using spontaneous Brillouin backscatter,” *IEEE Photonics Technol. Lett.*, vol. 9, pp. 979 – 981, July 1997.

17. V. Bhatia, D. Campbell, R. O. Claus, and A. M. Vengsarkar, “Simultaneous strain and temperature m easurement with long-period gratings,” Opt. Lett. Vol. 22, pp. 648-650, 1997.

CHAPTER 8

RESEARCH SUMMARY AND FUTURE WORK

8.1 Research summary

In summary, detailed investigations for a class of PCFs have been carried out. These include the theoretical investigation of the modal and polarization properties of Hi-Bi PCFs, estimation of MFD of ESM PCF and their connection loss with standard single mode fiber, design and analysis of SPSM and two-mode PCFs, and the applications of two-mode PCF for strain and temperature measurement.

The basic properties of an asymmetrical core PCF are theoretically investigated by using the full-vector FEM. The influence of fiber structural parameters on modal birefringence, MFD, and half divergence angle are investigated in detail. The group velocity dispersions for the two fundamental modes are also calculated and are found to be significantly different for the two orthogonal polarizations.

The full-vector FEM is also used to calculate the electrical field and to evaluate the equivalent MFD of ESM PCF. It was found that the MFD increases approximately linearly with pitch Λ and decreases with an increase in air-hole diameter to pitch ratio d/Λ. An empirical formula is proposed for estimating the MFD. The results calculated by using the formula deviates less than 1% for $0.25 \leq d/\Lambda \leq 0.45$ from those obtained from FEM. With the help of the MFD, the connection loss between a single mode fiber and a PCF can be evaluated by using the classical method based on the MFD.

Through the analysis of a Hi-Bi PCF by FEM with anisotropic PMLs, we have

presented the general design methodology of an asymmetrical core PCF for SPSM operation at an arbitrary operating wavelength. Specifically we optimized the PCF structure for operating at 1.30μm and 1.55μm. The bandwidths of the SPSM PCFs operation are respectively 84.7nm and 103.5nm for 1.30μm and 1.55μm, within which one polarization state is attenuated by at least 30dB/m while the orthogonal state suffers a confinement loss of less than 1dB/m. The cutoff wavelength is further validated by calculating the effective mode area of each polarization, which deviates less than 4% from that found by the confinement loss calculation using FEM. The coupling losses between the proposed SPSM fibers and single mode fibers were also calculated by using the overlap integral method and found to be over 70% for 1.55μm and 1.30μm, respectively.

A similar Hi-Bi PCF but with different parameters is found to support only the LP_{01} and LP_{11} modes from 543nm to 1310nm. The LP_{11}(odd) mode is unsupported within this broad range, and the supported LP_{11}(even) mode has a stable intensity lobe position. With the special modal properties of the Hi-Bi PCF, we experimentally demonstrated a two-mode PCF interferometer based on the modal interference between the LP_{01} and LP_{11}(even) modes propagating in the same length of PCF. The interferometer responses to axial strain and temperature were experimentally investigated over a wavelength range of from 543nm to 1310nm. For the strain sensor, the fiber elongations needed to produce 2π phase change decrease with the wavelength, indicating higher strain sensitivity at longer wavelengths. The strain sensitivity is also polarization dependent. The temperature sensitivity of the two-mode PCF sensor shows a non-monotonic dependence on the operating wavelength, which can be used to

perform temperature insensitive strain measurement. We present a theoretical analysis of the non-monotonic response. The theoretical sensitivities agree in trends with the experimentally measured results. These findings will play an important role in developing novel two-mode PCF sensors and devices.

8.2 Future work

During the progress of research on this interesting topic, some promising research directions have been identified. They are listed as follows:

The manufacturing of two-mode PCF with a broader optical wavelength range covering the whole low loss window of the silica will be very useful for the development of extremely broad band devices. However, it demands collaborations with other institutions with fiber manufacturing facilities. The contents of the thesis provide plenty of information on the design of two-mode PCFs with or without birefringence.

With the future development of two-mode PCFs with better performance and broader operating wavelength, novel optical fiber devices and optical fiber sensor can be readily implemented. Long period fiber gratings can be inscribed on the PCF by high-frequency CO_2 laser pulse to convert the fundamental mode to the first higher order modes. The higher order modes can be further removed by mode stripper and a notch filter can be realized on two-mode PCF.

Another potential device application is acousto-optic tunable filter, which relies on the interaction between the optical wave and acoustic wave co-propagating along the two-mode PCF. The ultra-broad two-mode wavelength range of the novel PCFs would

allow all fiber broad band tunable optical filters to be developed.

We have demonstrated the strain and temperature sensor based on the modal interference between the fundamental LP_{01} mode and LP_{11}(even) mode. A scheme for simultaneous strain and temperature measurement has also been proposed and theoretically analyzed in this aspect. Experimental investigations are expected to verify the theoretical analysis.

APPENDIX

PUBLICATIONS

Journals

1. **Ju J.**, Wang Z., Jin W., and Demokan M.S., "Temperature sensitivity of a two-mode photonic crystal fiber interferometric sensor," *IEEE Photonics Technology Letters*, accepted for publication.
2. **Ju J.**, Jin W., and Demokan M.S., "Design of single-polarization single-mode photonic crystal fiber at 1.30μm and 1.55μm," *IEEE Journal of Lightwave Technology*, vol. 24, no. 2, pp. 825-830, Feb 2006.
3. **Ju J.**, Jin W. and Demokan M.S., "Two-mode operation in highly birefringent photonic crystal fiber," *IEEE Photonics Technology Letters*, vol. 16, no. 11, pp. 2472-2474, Nov. 2004.
4. **Ju J.**, Jin W., Demokan M.S., "Properties of a highly birefringent photonic crystal fiber," *IEEE Photonics Technology Letters*, vol. 15, no. 10, pp. 1375-1377, Oct 2003.
5. **Ju J**., Jin W., Hoo Y.L., et al. "A simple method for estimating the splice loss of photonic-crystal fiber/single-mode fiber," *Microwave and Optical Technology Letters*, vol. 42, no. 2, pp. 171-173, July 2004.
6. Wang Z., **Ju J.**, Jin W., "Optimizing PCFs for two-mode interference," *Optical Fiber Technology*, vol. 12, no. 1, pp. 29-37, Jan 2006.

7. Zhi W., **Jian J.**, Jin W., Chiang K.S., "Scaling property and multi-resonance of PCF-based long period gratings," *Optics Express*, vol. 12, no. 25, pp. 6252-6257, Dec. 2004.
8. Wang Z., **Ju J.**, Jin W., "Properties of elliptical-core two-mode fiber," *Optics Express*, vol. 13, no. 11, pp. 4350-4357, May 2004.
9. Jin W., Wang Z., and **Ju J.**, "Two-mode photonic crystal fibers," *Optics Express*, vol. 13, no. 6, pp. 2082-2088, Mar. 2005.
10. Hoo Y.L., Jin W., **Ju J.**, Ho H.L, Wang D.N., "Design of photonic crystal fibers with ultra-low, ultra-flattened chromatic dispersion," *Optics Communications*, vol. 242, no. 4-6, pp. 327-332, Dec. 2004.
11. Hoo Y.L, Jin W., Ho H.L., **Ju J.**, and Wang D.N, "Gas diffusion measurement using hollow-core photonic bandgap fiber," *Sensors and Actuators B*, vol. 105, pp. 2, pp. 183-186, Mar. 2005.
12. Hoo Y.L., Jin W., **Ju J.**, et al. "Loss analysis of single-mode fiber/photonic-crystal fiber splice," *Microwave and Optical Technology Letters*, vol. 40, pp. 5, pp. 378-380, Mar. 2004.
13. Shi C.Z., Chan C.C., Zhang M., **Ju J.**, et al, "Simultaneous interrogation of multiple fiber Bragg grating sensors for dynamic strain measurements," *Journal of Optoelectronics and Advanced Materials*, vol. 4, no. 4, pp. 937-941, Dec. 2002.

Proceedings

1. **Ju J.**, Wang Z., Jin W., et al., "Temperature sensitivity of a two-mode photonic crystal fiber interferometer," 2005 IEEE LEOS Annual Meeting Conference

Proceedings (LEOS), pp. 856-857, Sydney, Australia, Oct. 22-28, 2005.

2. **Ju J**., Jin W., Hoo Y.L., et al., "Design of single-polarization PCF at 1300 and 1550nm bands," Second European Workshop on Optical Fiber Sensors, pp. 358-361, Santander, Spain, Jun 09-11, 2004.
3. **Ju J.**, Jin W., and Demokan M.S., "Properties of highly birefringent photonic crystal fiber", 16th International Conference on Optical Fiber Sensors, Nara, Japan, Oct., 2003.
4. Wang Z., **Ju J.**, Jin W., et al., "Properties of PCF-based long period gratings," 17th International Conference on Optical Fiber Sensors, Pts. 1-2, pp. 298-301, Brugge, Belgium May 23-27, 2005.
5. Jin W., Wang Z., **Ju J.**, "Two-mode photonic crystal fibers," 17th International Conference on Optical Fiber Sensors, Pts. 1-2, pp. 290-293, Brugge, Belgium, May 23-27, 2005.
6. Jin W., Hoo Y.L., **Ju J.**, and Ho H.L., "Loss analysis of single mode fiber/photonic crystal fiber splice", 16th International Conference on Optical Fiber Sensors, Nara, Japan, Oct., 2003.
7. Zhang M., Wang D., Jin W., **Ju J.**, Liao Y., and Lan S., "Wavelength modulation spectroscopy applied to intra-cavity absorption gas sensor", 16th International Conference on Optical Fiber Sensors, Nara, Japan, Oct., 2003.
8. Shi C.Z., Chan C.C., Zhang M., **Ju J.**, Jin W., et al, "Simultaneous interrogation of multiple FBG sensors for dynamic measurands," Advanced Sensor Systems and Applications, pp. 578-583, Shanghai, China, Oct. 15-18, 2002.